Silicon Plasmonic Sensor for Biological Detection

by

Fabbiha Bushra (200021105)
Muslima Siddiqui (200021117)
Sanzida Tasnim Nisa (200021122)

A Thesis Submitted to the Academic Faculty in Partial Fulfillment for the Requirements of the Degree of

BACHELOR OF SCIENCE IN ELECTRICAL AND ELECTRONIC ENGINEERING

Department of Electrical and Electronic Engineering
Islamic University of Technology (IUT)
Gazipur, Bangladesh

October 2025

Declaration of Authorship

We do hereby certify that the thesis titled "Silicon Plasmonic Sensor for Biological Detection" represents the outcome of research conducted under the supervision of Dr. Rakibul Hasan Sagor, Professor at the Islamic University of Technology. This work fulfills partial requirements for the degree of Bachelor of Science in Electrical and Electronic Engineering at IUT.

We affirm that this thesis or any part of it, has not been previously submitted for any other degree or diploma. Proper attribution has been given to all consulted sources and published works of others.

Signatures of the Candidates

…………………………………………….

Fabbiha Bushra

Student ID: 200021105

…………………………………………….

Muslima Siddiqui

Student ID: 200021117

…………………………………………….

Sanzida Tasnim Nisa

Student ID: 200021122

Certificate of Approval

Silicon Plasmonic Sensor for Biological Detection

Submitted by

Fabbiha Bushra (200021105)
Muslima Siddiqui (200021117)
Sanzida Tasnim Nisa (200021122)

has been approved by:

Dr. Rakibul Hasan Sagor

Supervisor and Professor,
Department of Electrical and Electronic Engineering,
Islamic University of Technology (IUT),
Boardbazar, Gazipur-1704.

Date: ………………….

Acknowledgement

We would like to begin by gratefully acknowledging the Almighty Allah for endowing us the perseverance, determination and strength to complete this thesis. We extend our sincere appreciation to Prof. Dr. Rakibul Hasan Sagor for his invaluable supervision, insightful guidance and constructive feedback throughout the course of this work. His continuous support and encouragement have been instrumental in the successful completion of this research.

We also wish to acknowledge Mr. A. K. M. Rakib, Mr. Sheikh Montasir Mahbub and Mr. Abdullah Taharat for their early guidance and instruction, which provided a strong academic foundation for our research endeavors. Our gratitude is further extended to all faculty members of the Department of Electrical and Electronic Engineering, IUT, for their consistent support, encouragement and inspiration during our academic journey.

We convey our sincere appreciation to our families for their constant encouragement, patience and faith in us. Their unwavering support has played a vital role in motivating us throughout the course of this work.

Fabbiha Bushra
Muslima Siddiqui
Sanzida Tasnim Nisa

October, 2025

Abstract

The thesis presents a groundbreaking advancement in photonic biosensing through the development of a CMOS-compatible plasmonic sensor that utilizes n-doped silicon as a high-performance alternative to conventional noble metals. By fundamentally reimagining both the material platform and structural design, this research overcomes the critical limitations of traditional surface plasmon resonance systems, including high optical losses, poor stability and fabrication incompatibility. Through systematic design evolution and rigorous finite element method optimization, we have created an innovative waveguide-coupled resonator architecture featuring embedded multi-ring nanostructures and strategically positioned dielectric pillars. This sophisticated design achieves exceptional performance metrics, demonstrating a sensitivity of 1270 nm/RIU and a figure of merit of 22.3 that competes favorably with noble metal-based sensors while offering superior integration capabilities. The sensor demonstrates precise identification of blood components, clear differentiation of intracellular biomolecules and reliable distinction between various tissue types. This research establishes a transformative foundation for next-generation point-of-care diagnostics, offering a commercially viable pathway toward scalable, cost-effective biosensing solutions. By bridging the critical gap between laboratory performance and real-world clinical implementation, this work paves the way for integrated lab-on-chip systems that combine high sensitivity with manufacturability, potentially revolutionizing personalized medicine, environmental monitoring and biomedical research.

Keywords:
Silicon plasmonics, Refractive index sensor, CMOS-compatible, High sensitivity, Biomedical diagnostics.

Table of Contents

List of Tables

List of Figures

List of Acronyms

Acronym	Full form
SPR	Surface plasmon resonance
SPP	Surface plasmon polaritons
RI	Refractive index
FOM	Figure of merit
FWHM	Full width at half maximum
CMOS	Complementary metal-oxide-semiconductor
MIM	Metal–insulator–metal
TiN	Titanium nitride
ZrN	Zirconium nitride
NIL	Nano-imprint lithography
OBE	Outcome-based education
CO	Course outcome
PO	Program outcome
K3–K8	Knowledge profile attributes
P1–P7	Attributes of complex engineering problem solving
A1–A5	Attributes of complex engineering activities
FEM	Finite element method
FEA	Finite element analysis
Si	Silicon

Au	Gold
Ag	Silver
DNA	Deoxyribonucleic acid
COMSOL	COMSOL multiphysics
NIR	Near-infrared
nm/RIU	Nanometers per refractive index unit

CHAPTER 1
INTRODUCTION

The work focuses on designing a silicon based plasmonic refractive index sensor for biological detection. It investigates doped silicon as an alternative to noble metals to overcome challenges like high optical loss, poor chemical stability and CMOS incompatibility [1], [2].

The objective is to develop a CMOS-compatible, highly sensitive, label-free sensor capable of detecting small refractive index variations for real-time biomedical and environmental applications [3], [4]. The sensor operates on surface plasmon resonance (SPR), where incident light excites surface-bound electromagnetic waves at the interface, and minor refractive index changes produce measurable resonance wavelength shifts [5]. This enables applications such as glucose monitoring, anemia detection and cancer cell differentiation [6], [7].

Traditional noble metals like gold and silver provide strong plasmonic responses but suffer from high cost, instability and limited CMOS compatibility [8]. In contrast, doped silicon and alternative materials like TiN and ZrN offer tunable optical properties, improved durability and better integration potential [9]. Among them, doped silicon shows lower optical loss and superior stability, making it an excellent choice for next-generation plasmonic biosensors [2].

1.1 Background

Plasmonic refractive index (RI) sensors operate on the principle of surface plasmon polaritons (SPPs), which are collective oscillations of free electrons at a metal-dielectric interface excited by incident light [10]. The key operational feature of these SPPs is their exceptional sensitivity to alterations in the adjacent medium's refractive index. This property makes plasmonic sensors powerful tools for identifying minor changes in biological or chemical samples, thus finding extensive use in chemical analysis, environmental sensing and biosensing applications [30].

Measurements are performed by tracking changes in resonance conditions, observed as shifts in either wavelength or intensity. This allows for highly accurate, real-time and label-free detection, a combination of features that is especially beneficial for analyzing biomolecules like DNA, proteins and pathogens. Consequently, these sensors are effectively used in applications such as the identification of viral antigens and cancer biomarkers, facilitating highly sensitive and rapid diagnostic procedures [10].

Silicon (Si), due to its compatibility with existing semiconductor fabrication technologies and its high refractive index contrast, has emerged as a promising material for plasmonic sensor designs [11–14]. Unlike traditional noble metals such as gold or silver, Si offers better integration possibilities with CMOS technology, enabling compact and cost-effective sensor platforms. The incorporation of Si in plasmonic structures allows precise control over waveguiding, resonance characteristics and field confinement, which significantly improves sensor performance [13], [14]. This makes Si-based sensors particularly attractive for lab-on-a-chip devices, where compactness and integration with electronic readout systems are critical.

Recent advancements in Si-based plasmonic sensors have demonstrated substantial improvements in sensitivity and figure of merit (FOM). For example, a Si-coated plasmonic sensor achieved a sensitivity of 2079.45 nm/RIU, representing a 28.31% enhancement over its uncoated counterpart [11]. Another sensor design demonstrated a sensitivity of 1145.71 nm/RIU and a maximum FOM of 393.25 RIU^{-1}, highlighting the effectiveness of Si-based plasmonic structures in detecting subtle refractive index changes [12]. Moreover, the integration of hybrid plasmonic structures, which combine Si with other dielectric or metallic layers, has been shown to further improve performance metrics, with one design achieving a sensitivity of 1276 nm/RIU and an FOM of 107 RIU^{-1} [13], [14].

The developments demonstrate that Si-based plasmonic sensors can provide both high sensitivity and selectivity, making them promising candidates for applications in biosensing, environmental monitoring and medical diagnostics [11–14]. Specifically, they have been explored for detecting glucose levels in blood, monitoring water contaminants and identifying low concentrations of disease-related biomarkers.

The development of Si-based plasmonic sensors requires careful optimization of several parameters, including the geometry of plasmonic structures, material selection, waveguide dimensions and integration techniques, to achieve the desired resonance characteristics and sensitivity [10], [11]. Fine-tuning these parameters allows researchers to maximize field confinement, reduce losses and enhance overall sensor performance. Ongoing progress in material science and nanofabrication techniques is positioning silicon-based plasmonic sensors to become key platforms for highly sensitive, compact and affordable analytical devices. Their potential applications are broad, spanning from point-of-care medical diagnostics to environmental sensing and portable chemical analysis [11–14].

1.2 Motivation

The growing demand for rapid, sensitive and cost-effective biosensing, particularly in healthcare and environmental monitoring, has highlighted the limitations of traditional plasmonic materials. While noble metals provide high sensitivity through SPR, they suffer from high optical loss, chemical instability and incompatibility with CMOS fabrication processes, making them unsuitable for mass production and on-chip integration [15]. These shortcomings restrict their use in next-generation portable diagnostic devices, where scalability, stability and reliability are essential.

In contrast, silicon, being abundant, biocompatible and CMOS-compatible, offers a scalable and eco-friendly alternative for plasmonic sensor design. Its availability and compatibility with mature semiconductor fabrication technologies ensure low-cost, large-scale production. Furthermore, silicon's chemical stability makes it more reliable under biological and environmental conditions compared to noble metals. Recent advancements have shown that doped silicon and emerging plasmonic materials such as titanium nitride (TiN) and zirconium nitride (ZrN) can overcome the inherent drawbacks of conventional metallic plasmonics [16], [17]. These materials not only maintain high sensitivity but also provide tunability in optical properties, further extending their potential in real-world biosensing. This makes them ideal candidates for applications requiring real-time, non-invasive and label-free detection of biomolecules.

Additionally, there is a pressing need for sensors that can detect subtle biomolecular interactions with high precision. This is particularly crucial for early-stage disease detection, where small variations in biomarker concentration can serve as critical diagnostic indicators. Beyond healthcare, such sensitivity is vital for environmental surveillance, where trace-level contaminants must be monitored to ensure safety and for portable diagnostics, where accuracy must be balanced with compact design and low power consumption [7]. The integration of these advanced sensors into lab-on-chip platforms could revolutionize point-of-care testing by providing fast, reliable and user-friendly biosensing capabilities at the patient's side.

This research is therefore motivated by the goals illustrated in Fig. 1.1, which aims to design a CMOS-compatible, ultra-sensitive silicon-based plasmonic sensor that is capable of real-time detection, while addressing both material and geometric optimization challenges [18]. By leveraging the unique properties of doped silicon and optimizing structural parameters for enhanced plasmonic performance, the proposed sensor aims to overcome the constraints of existing technologies. Ultimately, it aspires to contribute to next-generation biosensing systems that are not only scalable and low-cost, but also adaptable to diverse applications in medical diagnostics and environmental monitoring.

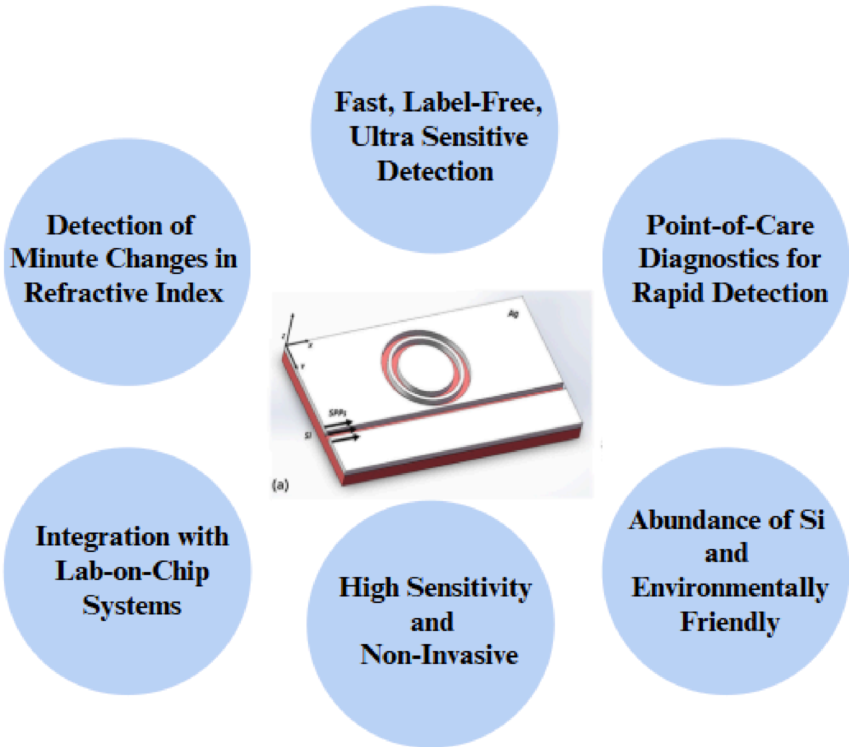

Fig. 1.1 Motivation of our research [19]

1.3 Objectives

The principal objective of this work is to engineer and systematically assess a silicon-based plasmonic sensor that can be used for biological detection. The study focuses on creating a sensor that is highly sensitive, reliable and compatible with modern fabrication technologies. By doing so, it aims to provide an alternative to traditional metal-based plasmonic sensors, which are often costly and difficult to integrate with standard CMOS processes [20], [9].

To achieve this goal, the research sets out several specific objectives. First, it seeks to improve the sensitivity and accuracy of plasmonic sensors by carefully optimizing their geometry, materials and structural parameters [2]. This involves exploring doped silicon, titanium nitride (TiN) and zirconium nitride (ZrN) as potential substitutes for noble metals [9], [18], since these materials can be more cost-effective and environmentally friendly while still offering strong plasmonic performance.

Another objective is to design a sensor structure that can be fabricated using existing silicon processing methods. This ensures that the proposed design is not only theoretically effective but also scalable and practical for real-world applications [20]. At the same time, the study aims to link the sensor's performance with realistic biological and environmental conditions, such as the refractive index ranges associated with diseases like cancer, anemia and bacterial infections [6], [7], [8], [21].

Finally, the work is intended to establish a foundation for future integration with microfluidics and lab-on-chip systems. Such integration would allow the sensor to be used in compact, portable devices for use in clinical diagnostics, on-site environmental analysis, and other decentralized sensing applications [2], [8]. In this way, the research not only advances the theoretical understanding of silicon-based plasmonics but also moves closer to practical applications that can benefit society.

CHAPTER 2
LITERATURE REVIEW & METHODOLOGY

Plasmonic sensors have become an important tool in biosensing because they detect refractive index changes from biomolecular interactions with high sensitivity. Silicon based plasmonic structures are especially promising due to their CMOS compatibility, cost effectiveness and ability to confine light efficiently [5].

Recent studies show that Si plasmonic sensors can detect early biomarkers of cancer, viral infections and neurological disorders. Their nanoscale sensitivity makes them suitable for real time and point-of-care detection [22]. This chapter reviews existing work and describes the methodology used for designing and evaluating a silicon plasmonic sensor for biological detection [22].

2.1 Basic functionality of the plasmonic RI sensor

The proposed sensor of Fig. 2.1 operates by detecting refractive index changes through the measurement of resonance wavelength shifts, which occur due to interactions at the sensor surface. It utilizes the principles of surface plasmon resonance (SPR), a phenomenon where incident light excites surface bound electromagnetic waves, making it highly sensitive to local refractive index variations [5]. This sensitivity enables the sensor to support a range of biological applications, such as monitoring glucose concentration, classifying hemoglobin levels for anemia detection and distinguishing between cancerous and normal cells [6].

In practical operation, the biological analyte (such as blood serum or tissue sample) is introduced into the sensor cavity, where it directly interacts with the sensing surface. Any variation in the analyte's composition leads to refractive index change, which in turn shifts the resonance wavelength of the SPR response. These spectral shifts are then correlated with specific biomarkers or concentration levels, enabling disease detection. For example, abnormal hemoglobin levels can indicate anemia, while characteristic refractive index signatures help differentiate cancerous from healthy cells [7].

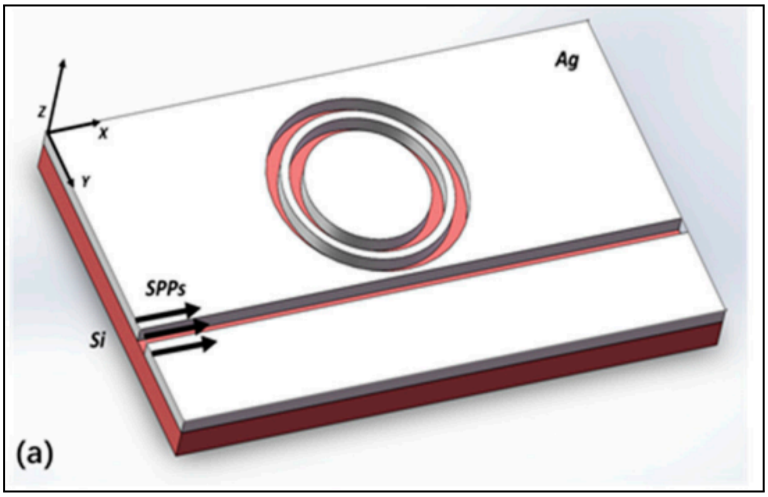

Fig. 2.1 A plasmonic RI sensor [23]

Additionally, the sensor offers fast, non-invasive operation and its compact, miniaturized design makes it a well-suited addition, paving the way for real-time, point-of-care diagnostics. Its compatibility with CMOS technology further enhances the feasibility of large-scale production and on-chip integration, making it suitable for portable diagnostic systems. The use of doped silicon not only reduces cost but also improves chemical stability compared to traditional noble metals, addressing major limitations in conventional SPR sensors. This positions the proposed sensor as a promising solution for next-generation biosensing in both clinical and environmental contexts [20].

2.1.1 Traditional noble metals vs Alternative plasmonic materials

Noble metals, like gold and silver, provide a strong plasmonic response, but face drawbacks in the form of incompatibility with CMOS, chemical stability and cost [15], [24]. Alternative materials such as TiN, ZrN, graphene and doped semiconductors address these challenges, offering better integration potential and tunable optical properties for next-generation plasmonic devices [9] .

Table 2.1 Traditional noble metals vs Alternative plasmonic materials

Traditional noble metals	Alternative plasmonic materials
Gold (Au)	Titanium nitride (TiN)
Silver (Ag)	Zirconium nitride (ZrN)

Aluminium (Al)	Graphene
Copper (Cu)	Doped semiconductors

The Table 2.1 highlights the commonly used noble metals and emerging alternatives in plasmonic sensing.

2.1.2 Metal vs doped silicon

Doped silicon presents a promising alternative to traditional metal-based plasmonic structures due to its superior material and fabrication properties. While metal–insulator–metal (MIM) structures suffer from high optical loss, poor chemical stability and complex nanofabrication requirements, doped silicon demonstrates reduced optical loss, enhanced chemical stability and ease of fabrication. Moreover, its compatibility with standard silicon fabrication processes ensures better integration with existing CMOS technology [2].

This compatibility allows doped silicon to bridge the gap between plasmonics and semiconductor technology, facilitating large-scale and cost-effective production. Consequently, it enhances the potential for practical applications in integrated photonic and biosensing devices [2].

2.1.3 Theoretical models for plasmonic sensor design

The design and simulation of plasmonic sensors rely heavily on accurate theoretical models that describe how materials interact with electromagnetic fields at the nanoscale. Several models are commonly used to capture the optical properties of plasmonic materials and guide sensor optimization.

2.1.3.1 *drude model*

The Drude model assumes that conduction electrons respond to electromagnetic waves like a classical gas of particles, leading to a dielectric function of the form,

$$\epsilon(\omega) = \epsilon_{\infty} - \frac{\omega_P^{2}}{\omega^{2} + i\gamma\omega} \tag{2.1}$$

Drude model is useful for metals like Au, Ag and doped semiconductors at low frequencies (IR/NIR region). It offers a simple yet effective way to describe how they optically behave by linking their free-electron behavior to measurable quantities such as plasma frequency and damping factor.

The main advantages lie in its analytical simplicity and ability to accurately predict material responses in the infrared and near-infrared regions, making it particularly useful for plasmonic and optoelectronic device modeling. However, the model's limitations arise from its classical assumptions, it neglects quantum effects, interband transitions and electron-electron interactions, leading to inaccuracies at higher frequencies (visible or UV range) and for materials with complex band structures.

2.1.3.2 *lorentz model*

This model accounts for bound electrons oscillating at specific resonance frequencies and is often combined with the Drude model for materials with both free and bound electrons. It gives dielectric function of the form,

$$\epsilon(\omega) = \epsilon_{\infty} - \sum_{j} \frac{f_j \omega_{P,j}^2}{\omega_{0,j}^2 - \omega^2 - i\gamma_j \omega} \tag{2.2}$$

It is suitable for dielectric and semiconductor with significant interband transitions. The Lorentz model describes the behavior of bound electrons that oscillate at specific resonance frequencies, making it suitable for materials where interband transitions play a major role. Its main advantage is its ability to accurately model dielectric and semiconductor materials by capturing resonant absorption and dispersion effects that the Drude model cannot represent.

Lorentz model is often combined with the Drude model to describe materials containing both free and bound electrons, providing a more comprehensive understanding of their optical response. However, the Lorentz model can be computationally complex and may require multiple fitting parameters to match experimental data, which can make it less efficient for simplified analytical modeling.

2.1.3.3 *lorentz-drude model*

A hybrid model that merges both the free electron Drude and bound electron Lorentz contributions. This model provides a more complete representation of the dielectric response of materials like doped silicon, TiN and ZrN. This model captures both intraband (free carrier) and interband (bound carrier) effects, which is essential for accurate simulation in biosensing regimes.

The Lorentz–Drude model can be attributed to be a mixed approach that combines the free-electron behavior of the Drude model with the bound-electron resonance effects of the Lorentz model, offering a comprehensive representation of a material's dielectric response. This model enables accurate optical simulations across a broad frequency range, improving prediction of resonance peaks, absorption behavior and refractive index variations. However, it can be mathematically intensive and requires precise parameter fitting, which may complicate analysis for materials with complex electronic structures.

2.1.3.4 *effective medium theory*

EMT is used when materials are nanostructured or consist of composite layers (metal-dielectric stacks). EMT allows estimating the effective permittivity based on the volume fractions of constituents and predicts optical response in layered or porous structures, though less commonly used for bulk plasmonic sensor simulations.

EMT provides a mathematical framework to estimate the overall dielectric response of nanostructured or composite materials by averaging the properties of their individual constituents according to their volume fractions. It is particularly useful for modeling layered, porous or metal-dielectric composite structures, where the electromagnetic fields interact with multiple materials simultaneously.

The main advantage of EMT lies in its ability to simplify complex nanostructures into an equivalent homogeneous medium, enabling easier analysis of optical behavior. However, its accuracy decreases when the structural dimensions become comparable to the wavelength of light and it may fail to capture localized plasmonic effects, making it less reliable for detailed plasmonic sensor simulations.

2.1.3.5 *maxwell's equations & boundary conditions*

Maxwell's equations govern all the simulations. The equations see use for solve of electromagnetic fields in the structure using -

a) Frequency-domain analysis (in COMSOL or Lumerical)
b) Boundary conditions like perfectly matched layers (PMLs) and port excitations

Using Maxwell's equations with frequency-domain analysis allows precise modeling of electromagnetic fields in complex structures, making it highly accurate for predicting optical responses in plasmonic sensors. The incorporation of boundary conditions like PMLs and port excitations ensures minimal artificial reflections and realistic excitation of the structure. However, this approach can be computationally intensive, especially for fine meshes or large-scale 3D simulations and results can be sensitive to the choice of boundary settings and meshing, requiring careful setup to avoid numerical errors or convergence issues.

2.2 Literature review

2.2.1 Surface plasmon resonance (SPR) and its principles

When light incident at the interface of a metal and a dielectric couples with SPPs, then the phenomenon of surface plasmon resonance (SPR) occurs [6]. Due to this sensitivity, even small RI variations can be detected, which makes SPR highly suitable for sensing applications.

SPR can detect biomolecular interactions. It has been applied largely for the purpose of current and label-free detection [5]. It enables monitoring of proteins, nucleic acids and whole cells without chemical labeling, offering high sensitivity and specificity. Coupling SPR with nanostructures further enhances electromagnetic confinement and sensor performance [4]. Recent developments also explore integration with silicon photonic biosensors, providing CMOS-compatible and cost-effective solutions for biomedical diagnostics, environmental monitoring and food safety [25].

In addition to sensitivity, the versatility of SPR lies in its ability to be integrated into different optical configurations such as prism-based, fiber-optic and waveguide systems. These configurations allow adaptability for various application environments, from laboratory-scale diagnostics to portable point-of-care devices. With ongoing progress in nanofabrication and material engineering, SPR platforms are increasingly being optimized to achieve higher detection accuracy, lower noise levels and broader applicability in interdisciplinary fields [5], [25].

2.2.2 Traditional and emerging plasmonic materials

Conventional SPR sensors are typically based on noble metals such as gold (Au) and silver (Ag), which provide strong plasmonic responses in the visible and near-infrared spectrum [26]. While effective in field confinement and sensitivity, these metals suffer from high optical losses, limited thermal and chemical stability and incompatibility with CMOS fabrication processes. Such drawbacks restrict their scalability and long-term use in integrated sensing platforms.

To address these issues, alternative plasmonic materials such as doped silicon, titanium nitride (TiN) and zirconium nitride (ZrN) have been explored. Doped silicon offers CMOS compatibility and tunable plasmonic properties suitable for integration into photonic circuits [20]. TiN and ZrN, on the other hand, exhibit mechanical durability, chemical stability and cost-effectiveness while maintaining plasmonic performance in the visible spectrum [16]. These materials provide robust, scalable platforms for next-generation biosensors, shifting the focus of research from noble metals to CMOS-compatible alternatives with practical biomedical potential [20], [26], [16].

2.2.3 Doped silicon as a plasmonic material

To address the inherent drawbacks of noble metals, this work proposes a high-sensitivity plasmonic refractive index sensor utilizing n-doped silicon, a tunable and CMOS-compatible material [2]. Unlike conventional MIM structures, their design in Fig. 2.2 uses plasmonic properties of doped Si to reduce optical losses and enable integration with existing semiconductor technology. The sensor demonstrated a resolution of 2.04×10^{-4} RIU. It also showed sensitivity of 4900 nm/RIU which was maximum, showing competitive performance compared to traditional noble metal counterparts [2].

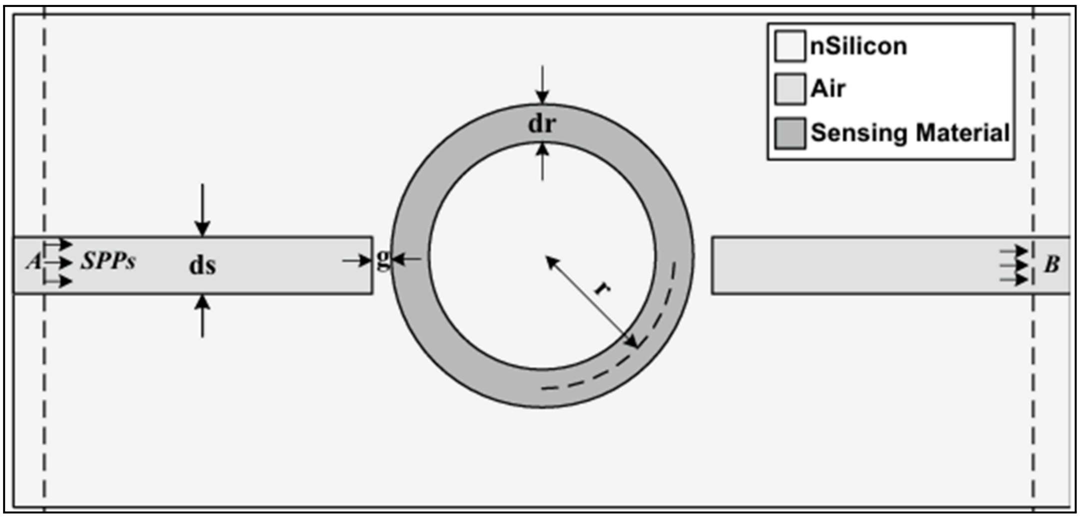

Fig. 2.2 Design of sensor

The study also emphasized the ability of doped silicon to detect extremely small refractive index variations, particularly in low-index regimes such as gas-phase sensing, as shown in Fig. 2.3 [2]. This makes it a strong candidate for biosensing applications where the target analytes often produce subtle RI changes. Moreover, the work highlights that doped Si can provide a balance between sensitivity, fabrication feasibility and device stability, offering a pathway toward next-generation plasmonic sensors optimized for biomedical and environmental applications [2].

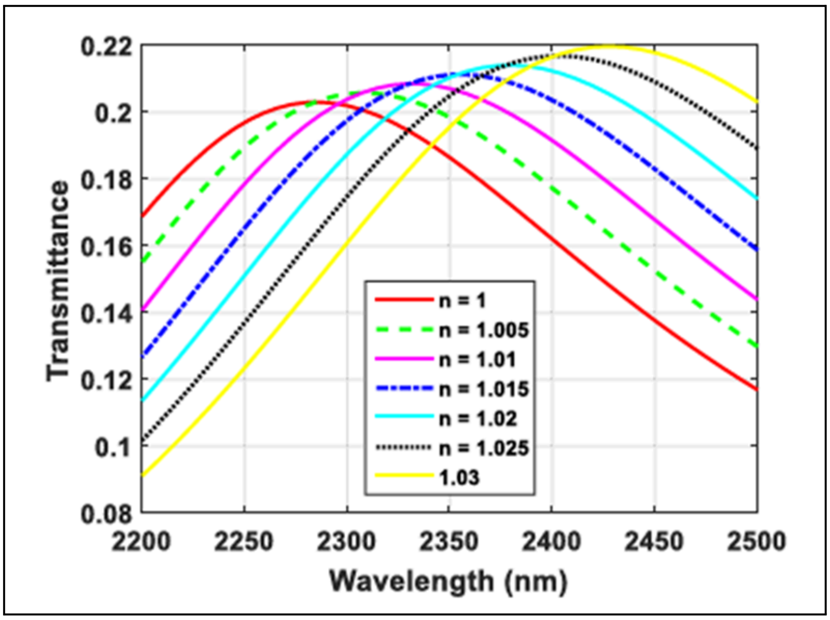

Fig. 2.3 Transmittance graph of the sensor

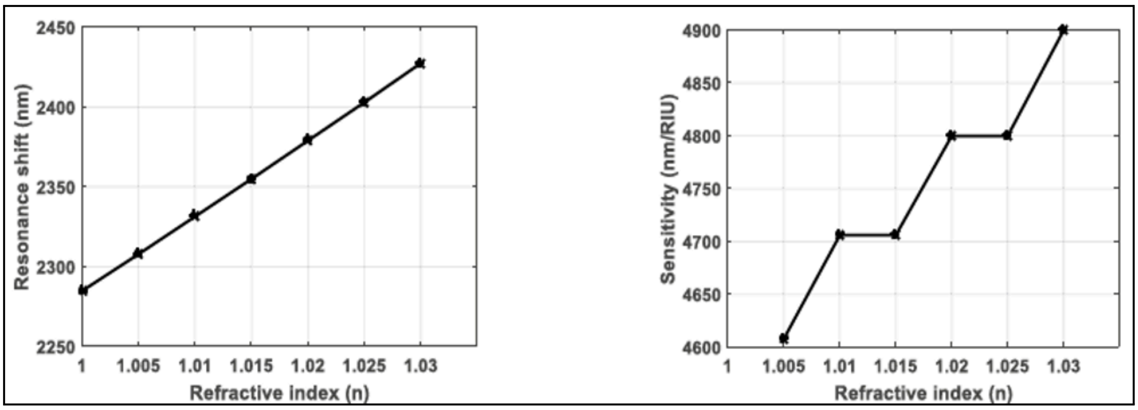

Fig. 2.4 Change of resonance & sensitivity with RI

In addition to its strong optical performance, the study provides valuable insights into the tunability of doped silicon-based plasmonic sensors through carrier concentration adjustment [2]. By varying the doping density, the plasma frequency and permittivity of silicon can be precisely controlled, allowing the sensor to operate effectively across a wide spectral range, from near-infrared to mid-infrared, illustrated in Fig. 2.4. This tunability enables customized sensor designs for different biological or chemical analytes, enhancing the versatility of the platform.

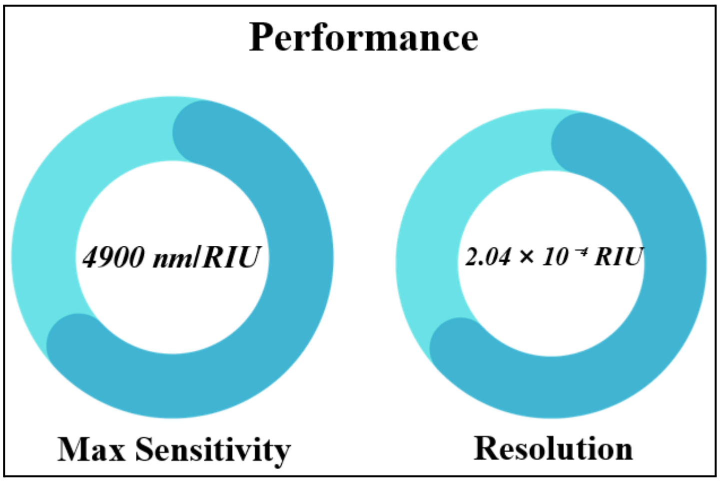

Fig. 2.5 Different performance metrics

The authors further demonstrated that doped Si exhibits improved thermal stability and chemical durability compared to noble metals such as gold and silver., which suffer through surface degradation. The performance characteristics are shown in Fig. 2.5. Consequently, the proposed n-doped silicon plasmonic sensor not only addresses the cost and compatibility limitations of traditional metals but also opens new opportunities for developing robust, miniaturized and efficient sensors for integrated photonic systems [2].

2.2.4 Biosensing applications in medical diagnostics

The use of plasmonic sensors in medical diagnostics was demonstrated with a focus on early detection of diseases such as diabetes, anemia and cancer [7]. This study showed that the sensor could effectively distinguish glucose concentrations, classify hemoglobin levels and differentiate between cancerous and normal cells through refractive index variations, as shown in Fig. 2.9. The reported maximum sensitivity was 2963.73 nm/RIU, indicating strong potential for reliable biosensing performance [7].

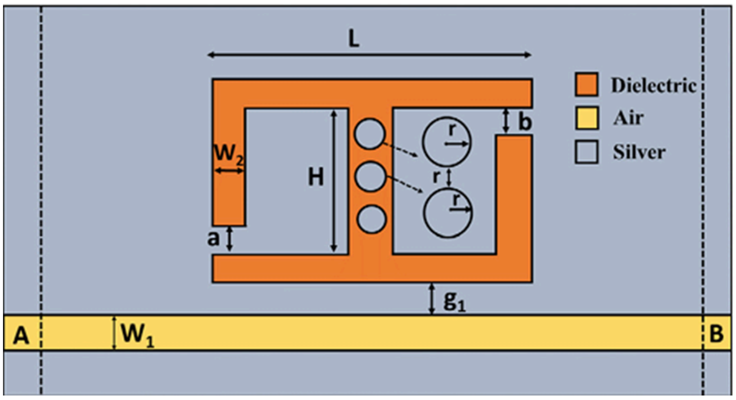

Fig. 2.6 Design of sensor

The work further highlighted the importance of plasmonic sensors in point-of-care and non-invasive diagnostic applications [7]. By detecting biomarkers associated with multiple diseases in real time, the sensor design in Fig. 2.6 underlines the versatility of plasmonic biosensing platforms for healthcare monitoring. This demonstrates that plasmonic-based refractive index sensing can be extended beyond single-analyte detection to a wide range of biomedical applications, thereby offering a pathway for practical clinical implementation [7].

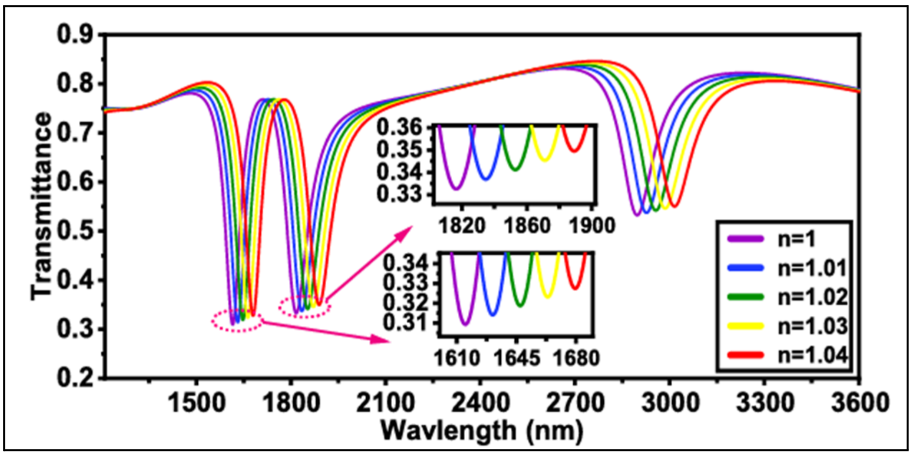

Fig. 2.7 Transmittance graph of the sensor

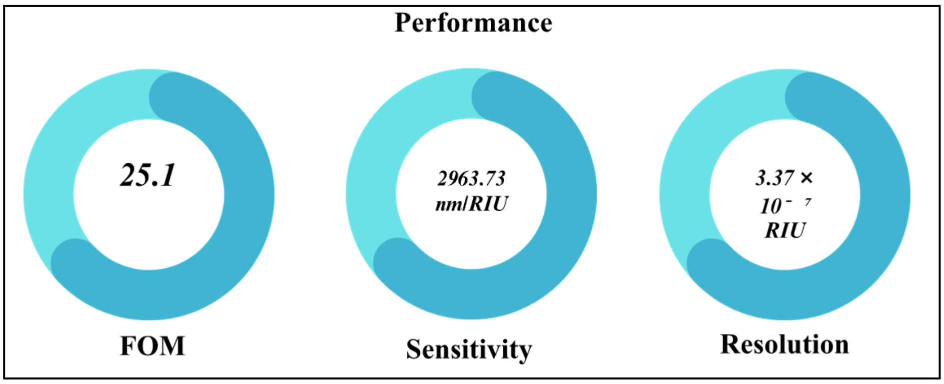

Fig. 2.8 Different performance metrics

Moreover, the study emphasized the correlation between the refractive index values of different biological fluids and specific disease states, enabling the sensor to act as a diagnostic fingerprinting tool [7]. Through simulation and experimental validation, such as Fig. 2.7, the researchers demonstrated how subtle refractive index shifts could be directly linked to physiological changes, such as glucose concentration fluctuations or variations in hemoglobin content. This precise mapping of RI variations to disease biomarkers highlights the potential of plasmonic sensors in continuous health monitoring and early-stage disease detection. The performance characteristics are shown in Fig. 2.8.

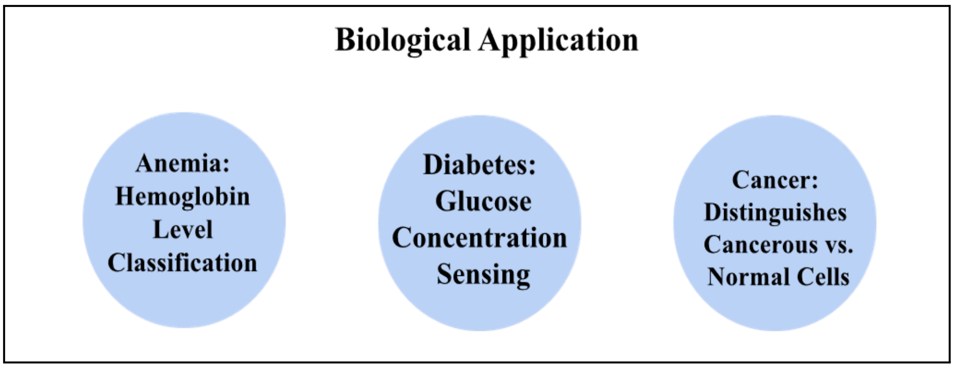

Fig. 2.9 Applications of the sensor

Additionally, the compact design and high sensitivity of the proposed system make it suitable for integration into portable medical devices, supporting real-time, low-cost and non-invasive diagnostics. Hence, the work in [7] establishes a significant advancement in applying plasmonic refractive index sensors to biomedical fields, making a path for coming generation diagnostic technologies that combine precision, speed and accessibility.

2.2.5 Fuel classification and environmental sensing

In a separate study, the use of plasmonic sensors, shown in Fig. 2.10, for fuel classification and the detection of adulterants, such as kerosene in diesel was explored [8]. The design achieved a peak of 3270.3 nm/RIU in terms of sensitivity. It also demonstrated a sensitivity of temperature of 1.159 nm/°C, indicating its potential for multifunctional sensing applications [8].

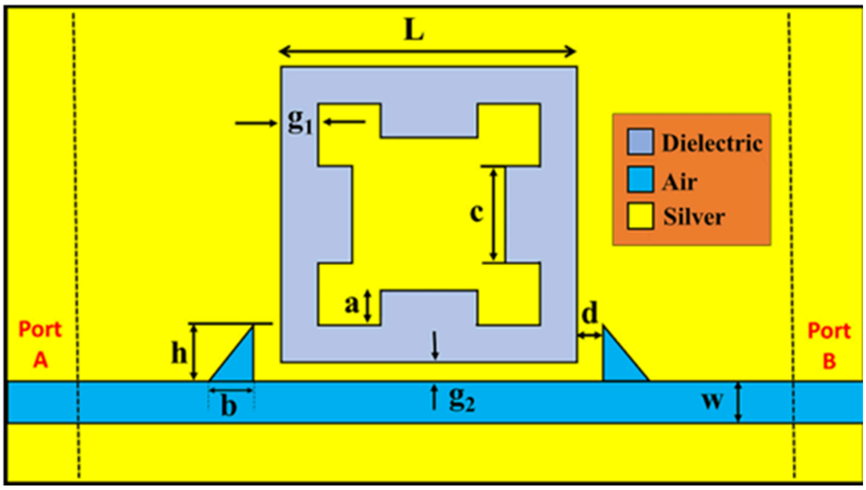

Fig. 2.10 Design of sensor

The study further highlighted the practicality of the approach, as the device was fabricated using nano-imprint lithography (NIL), demonstrating both scalability and cost-effectiveness for large-scale deployment [8]. This work underscores the versatility of plasmonic sensors, showing that they can be applied beyond biomedical diagnostics to industrial applications, while maintaining high sensitivity, precision and integration potential [8].

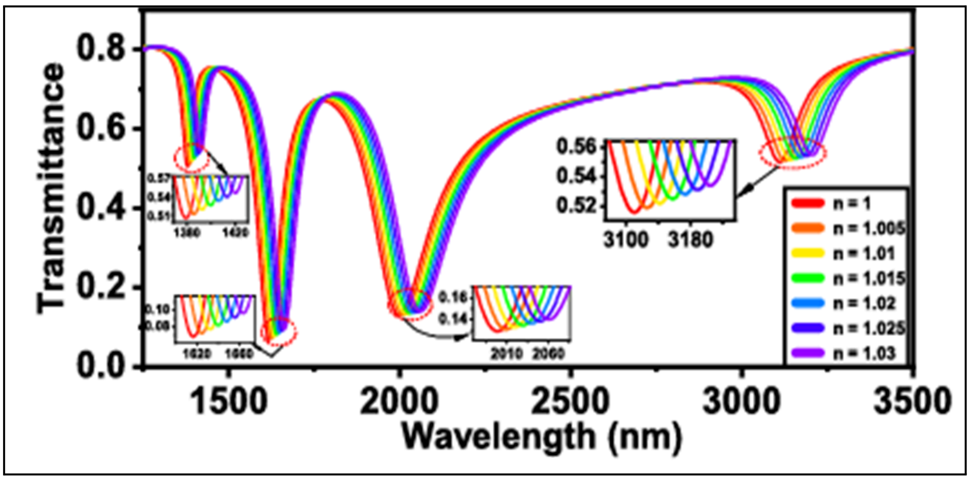

Fig. 2.11 Transmittance graph of the sensor

Furthermore, it demonstrated that the sensor's high refractive index sensitivity could effectively differentiate between various fuel types and identify even minimal levels of adulteration [8]. By monitoring the distinct refractive index signatures of pure and mixed fuels, from Fig. 2.11, the system provided a reliable method for ensuring fuel quality control.

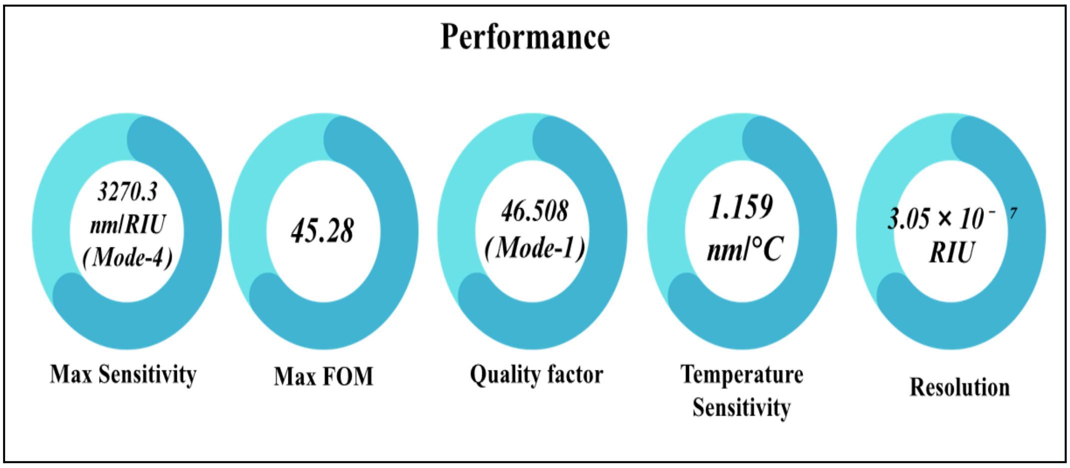

Fig. 2.12 Different performance metrics

The inclusion of temperature sensitivity analysis added another dimension to the sensor's capability, allowing it to compensate for thermal variations that could affect measurement accuracy in industrial environments. The successful use of nano-imprint lithography (NIL) not only validated the sensor's manufacturability but also positioned it as a scalable and low-cost solution suitable for commercial production. The performance characteristics are shown in Fig. 2.12.

Overall, the findings broaden the scope of plasmonic sensor applications, highlighting their adaptability to environmental and industrial monitoring while maintaining high performance and structural simplicity [8].

2.2.6 RI sensor based on ring-type pentagonal resonator

A plasmonic RI sensor, shown in Fig. 2.13, was made using a pentagonal resonator integrated with a MIM waveguide [27]. The pentagonal geometry with ring-type formation enhances light confinement and supports surface plasmon polaritons, resulting in a value of 2325 nm/RIU for maximum sensitivity . Its compact design also makes it suitable for integration with photonic circuits [27].

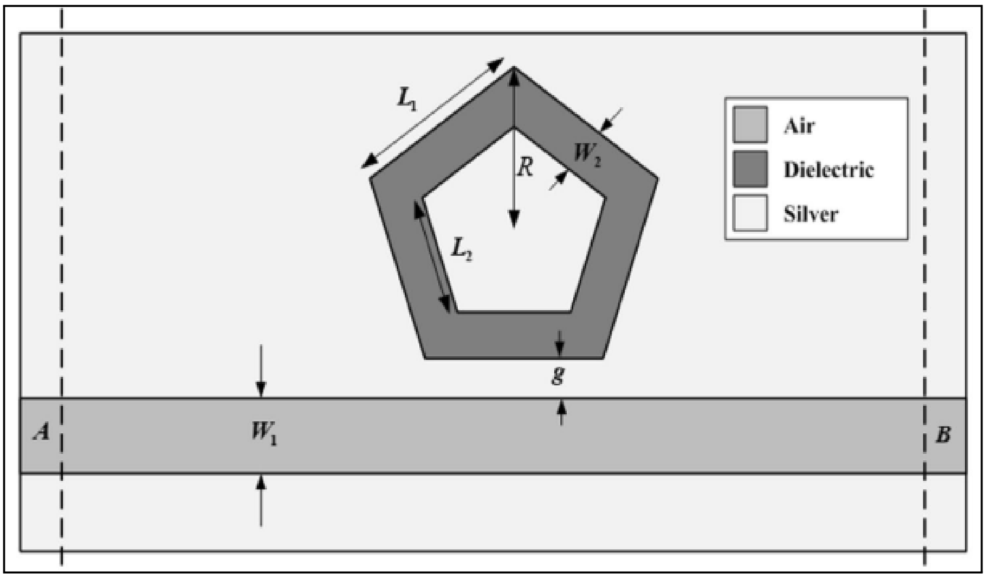

Fig. 2.13 Design of sensor

The sensor demonstrates improved light-matter interaction, enabling detection of small refractive index changes with high precision [27]. Its potential applications include sensing of biological components, detection of chemicals and monitoring of environment, highlighting the versatility of advanced geometric resonator designs in next-generation plasmonic sensors [27].

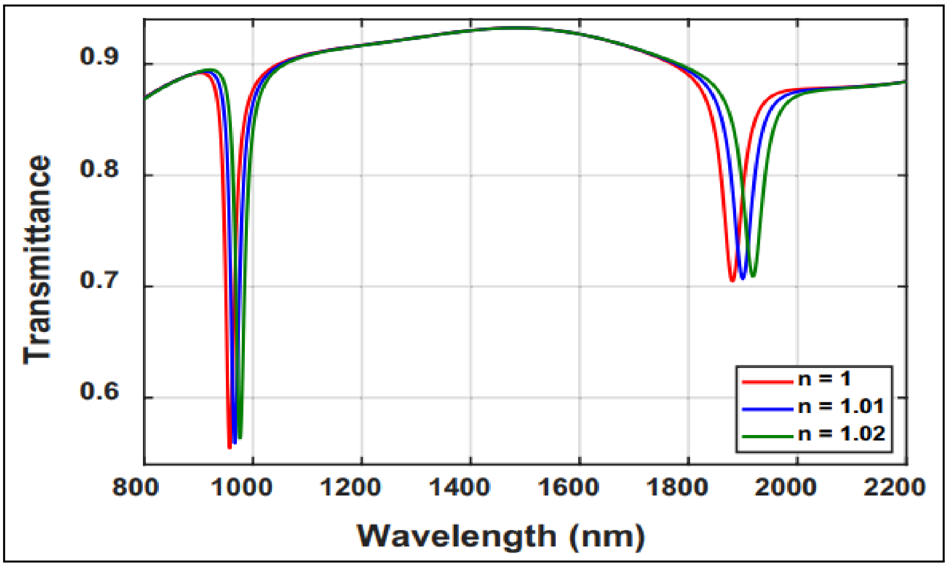

Fig. 2.14 Transmittance graph of the sensor

Additionally, the study in Fig. 2.14, emphasized that the pentagonal resonator structure provides multiple resonance modes due to its asymmetric geometry, allowing flexible tuning of the operating wavelength through adjustments in side length and coupling gap [27]. The study employed FEM simulations to obtain transmission graphs and distributions of E-field, revealing strong localization at the interface of metal and dielectric.

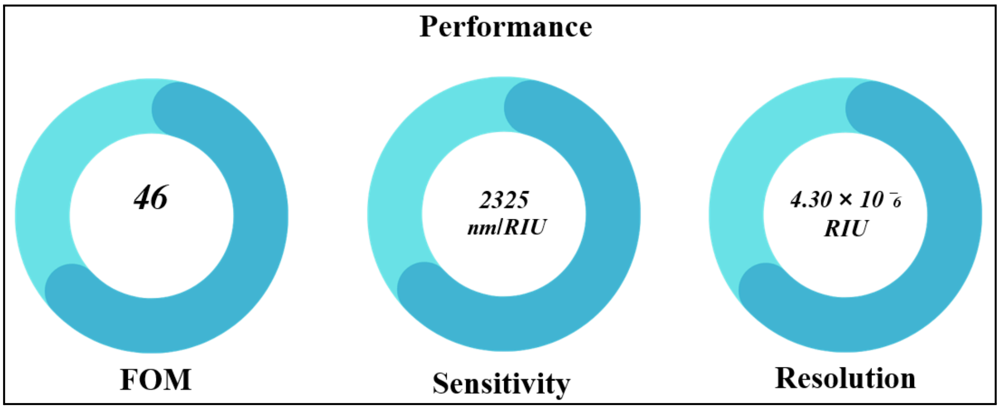

Fig. 2.15 Different performance metrics

Furthermore, the design's compactness and compatibility with MIM-based platforms make it a promising candidate for on-chip integration, supporting scalable fabrication for practical applications. The performance characteristics are shown in Fig. 2.15. Overall, the work establishes that tailoring resonator geometry, such as adopting a pentagonal configuration can significantly improve plasmonic sensor performance, opening opportunities for ultra-sensitive, miniaturized devices suited to real-time detection in biomedical and industrial environments [27].

2.2.7 ZrN based plasmonic sensor

A plasmonic sensor, shown in Fig. 2.16, was proposed based on zirconium nitride (ZrN) as an alternative to traditional noble metals [28]. The study highlights ZrN's tunable optical properties, chemical stability and CMOS compatibility, making it suitable for integration into modern photonic circuits. The sensor demonstrated strong plasmonic resonance and high sensitivity, showing that ZrN can overcome the limitations of Au and Ag, such as high optical losses and poor fabrication compatibility [28].

The work also emphasizes that ZrN based sensors can maintain performance under varying environmental conditions, including temperature changes, while providing efficient light confinement for enhanced refractive index detection [28]. This positions ZrN as a promising material for next generation plasmonic devices in applications like biosensing, chemical detection and integrated photonic systems [28].

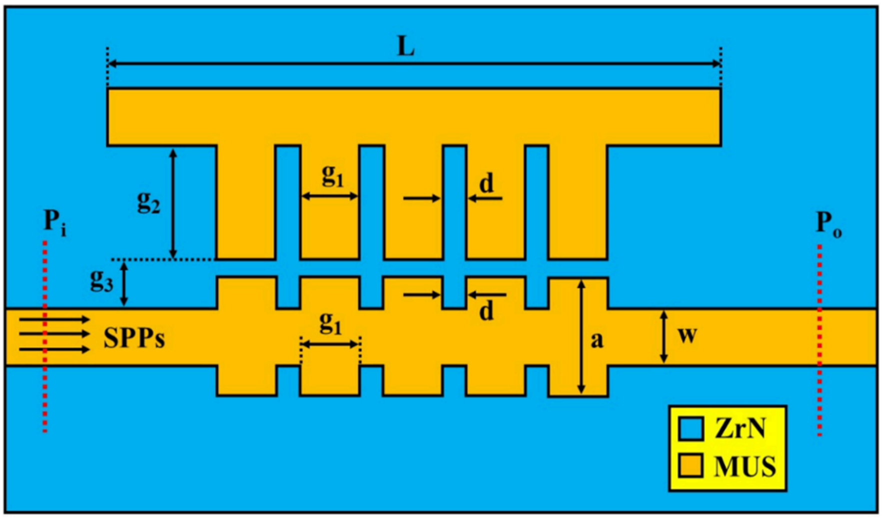

Fig. 2.16 Design of sensor

Furthermore, a comprehensive comparison between ZrN and conventional noble metals was conducted, demonstrating that ZrN offers a more stable plasmonic response across a broad spectral range, particularly in the visible and near-infrared regions [28]. Through numerical simulations and optical characterization, such as in Fig. 2.17, the study confirmed that ZrN exhibits lower damping losses and improved field at the interface of metal and dielectric, contributing to superior sensing performance.

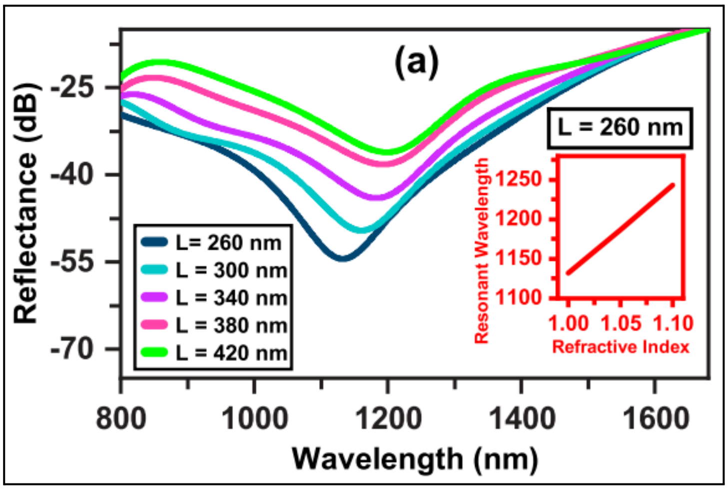

Fig. 2.17 Transmittance graph of the sensor

The authors also highlighted the material's robustness against oxidation and corrosion, which are common issues in Au- and Ag-based plasmonic structures. Additionally, the study showcased that the optical behavior of ZrN can be further tailored through controlled stoichiometry and deposition parameters, providing design flexibility for specific sensing applications. The performance characteristics are shown in Fig. 2.18.

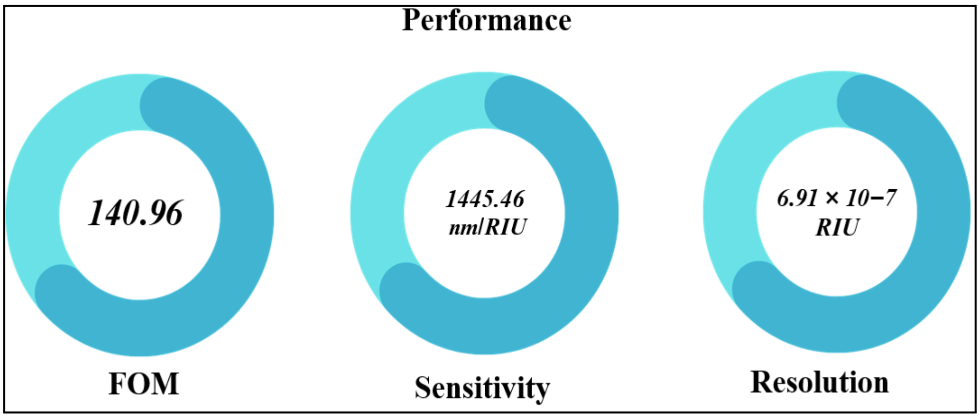

Fig. 2.18 Different performance metrics

Thus, the findings establish ZrN as a viable and sustainable alternative to noble metals, paving the way for durable, cost-effective and CMOS-compatible plasmonic sensors suitable for both biomedical and environmental monitoring [28].

2.2.8 High figure of merit based on concentric-rings resonator

The paper *"Plasmonic Refractive Index Sensor with High Figure of Merit Based on Concentric-Rings Resonator"* presents a structure of a plasmonic RI sensor utilizing concentric-ring resonators to achieve superior sensitivity value and FOM [23], as shown in Fig. 2.19. The design leverages surface plasmon resonance (SPR) modes confined within multiple metallic rings, enhancing field confinement and resonance sharpness.

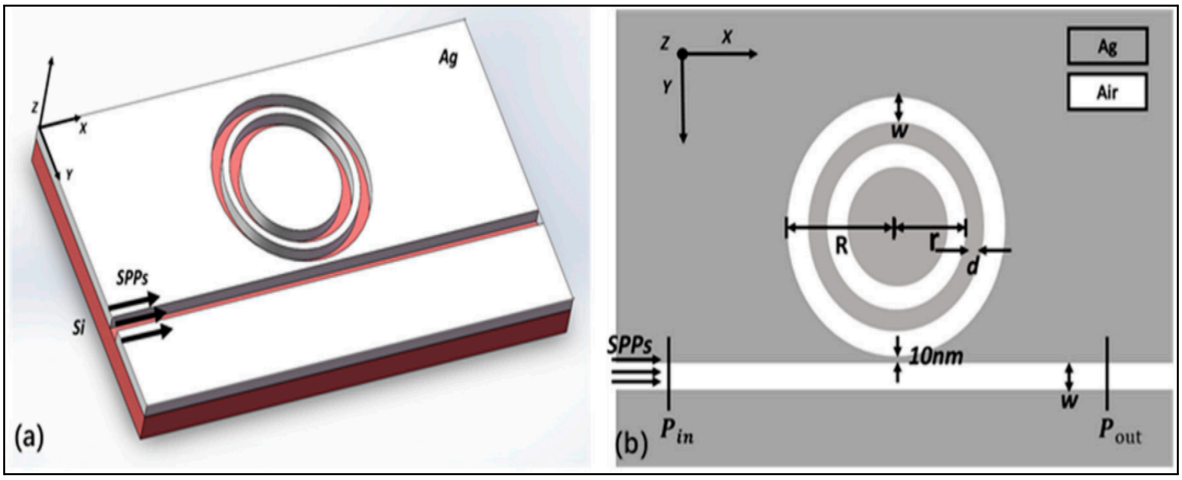

Fig. 2.19 (a) 3D design of sensor (b) 2D design of sensor

The configuration enables a strong light–matter interaction between the analyte and the plasmonic surface, resulting in a narrow linewidth and high-quality resonant peaks. By optimizing the geometrical parameters, such as ring radius, spacing and metal thickness, the authors report a significant improvement in sensing performance compared to conventional ring and MIM (metal–insulator–metal) resonators.

The study systematically investigates the transmission spectra and field distribution using FEM based analysis. Findings from the simulations, such as from Fig. 2.20, demonstrate that the concentric-rings resonator supports multiple resonant modes, among which the fundamental mode exhibits the highest sensitivity and stability under varying refractive index conditions.

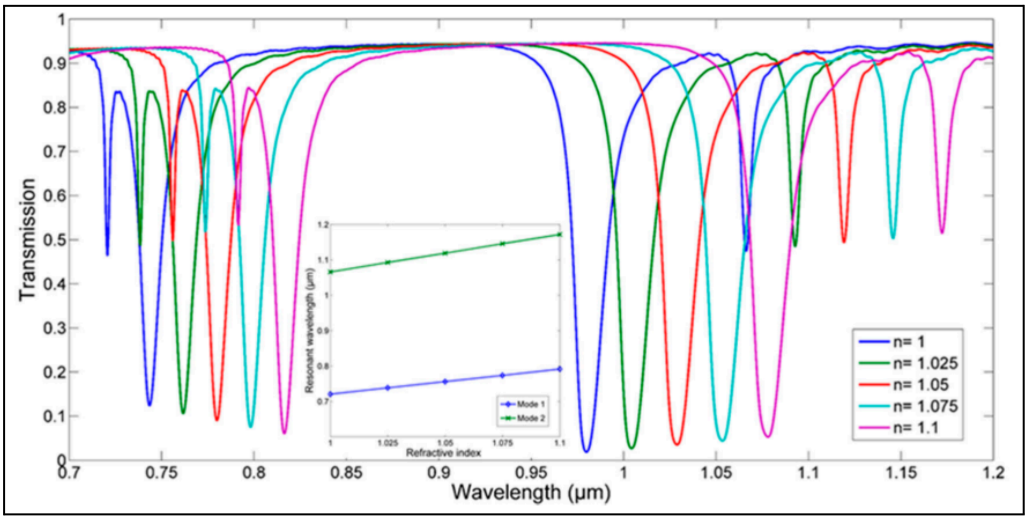

Fig. 2.20 Transmittance graph of the sensor

The design managed to result in a sensitivity of several hundred nm/RIU and a high FOM due to its narrow FWHM. The strong electric field localization at the metal–dielectric interface indicates the potential for detecting small changes in the surrounding medium, making the design suitable for high-precision biosensing applications [23]. The performance characteristics are shown in Fig. 2.21.

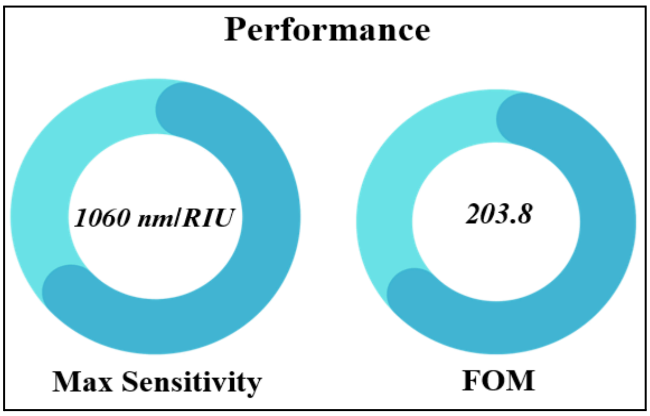

Fig. 2.21 Different performance metrics

Furthermore, the paper emphasizes the advantages of the concentric-rings configuration in terms of fabrication feasibility and integration compatibility with existing photonic systems. The circular symmetry ensures polarization-independent response, a desirable property for practical sensing environments. The study concludes that the proposed structure can outperform many previously reported plasmonic sensors in both sensitivity and FOM, establishing a promising platform for biochemical and environmental sensing applications. The findings thus contribute to the ongoing research on compact, high-performance plasmonic sensors capable of detecting minute refractive index variations with high accuracy [23].

2.2.9 Temperature and detection of biomolecules

The paper *"A plasmonic refractive index sensor with high sensitivity and its application for temperature and detection of biomolecules"* presents an innovative plasmonic sensor design capable of dual functionality, refractive index and temperature sensing, making it highly suitable for biological and environmental applications [29]. The proposed sensor leverages a MIM waveguide integrated with a resonant structure, consisting of cavity, to achieve strong light confinement and enhanced surface plasmon resonance (SPR), as shown in Fig. 2.22.

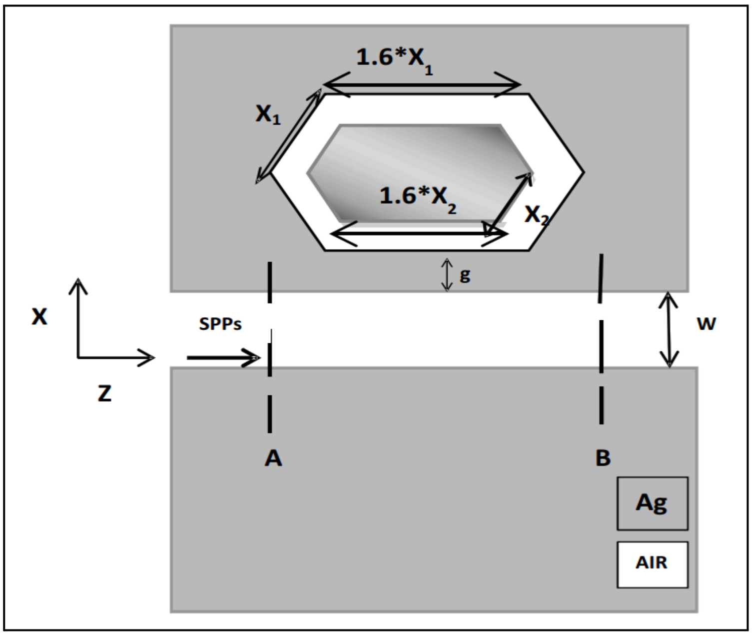

Fig. 2.22 Design of sensor

Through FEM analysis, the study demonstrates a sensitivity exceeding several thousand nm/RIU in maximum, indicating its potential for identification of minute variations in the RI caused by biomolecular interactions or environmental changes, as shown in Fig. 2.23. The incorporation of temperature responsiveness further enhances its versatility, allowing simultaneous measurement of thermal and optical variations [29].

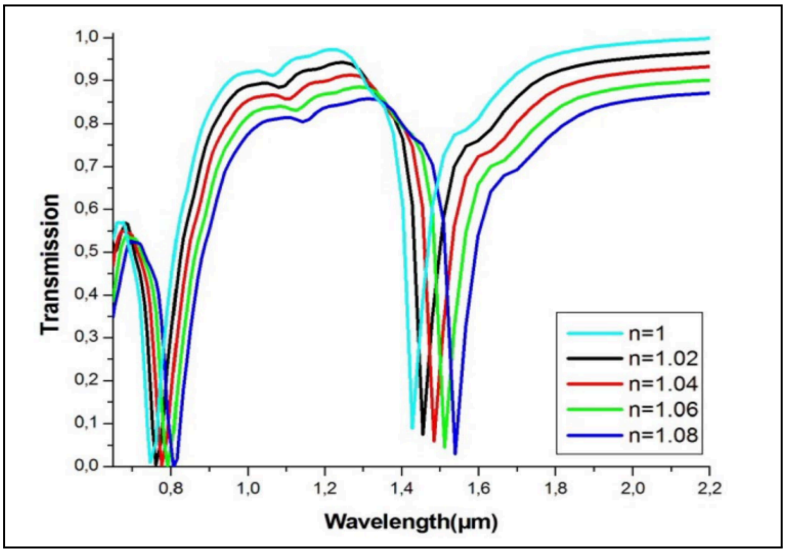

Fig. 2.23 Transmittance graph of the sensor

The authors performed a detailed analysis of how geometric parameters, such as cavity size, coupling gap and metal thickness, affect the resonance wavelength and overall sensor performance. The study reports that optimizing these structural parameters leads to narrow resonance linewidths and a high FOM, ensuring precise detection of biomolecules like proteins and glucose. The performance characteristics are shown in Fig. 2.24.

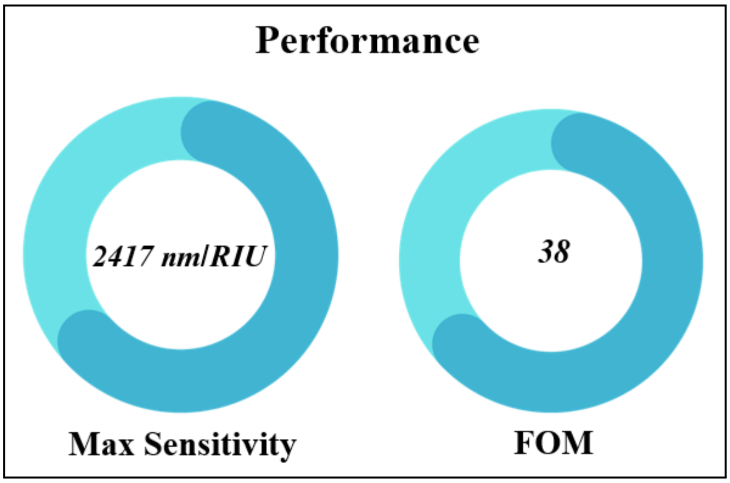

Fig. 2.24 Different performance metrics

The field distribution plots confirm strong electric field localization at the metal–dielectric interface, which facilitates effective light–matter interaction critical for biosensing. The temperature-dependent refractive index variations were also analyzed, demonstrating a linear response suitable for accurate thermal calibration. Such multifunctional sensing capability makes the design particularly useful for biomedical diagnostics and environmental monitoring [29].

Moreover, the work underscores the potential of integrating plasmonic refractive index sensors into lab-on-chip systems for real-time, label-free detection [29]. The combination of high sensitivity, compact design and compatibility with standard nanofabrication techniques highlights the sensor's practical feasibility. By demonstrating both temperature and biomolecular detection within a single platform, the study broadens the application scope of plasmonic sensors beyond traditional single-parameter measurement. Overall, the study provides an important contribution to the development of advanced, multifunctional plasmonic sensing devices with significant implications for biosensing, photonic circuitry and smart environmental monitoring technologies [29].

2.2.10 Nanoring-strip graphene arrays

The paper *"A Tunable Plasmonic Refractive Index Sensor with Nanoring-Strip Graphene Arrays"* introduces a unique, tunable sensor structure with periodic nanoring-strip arrays of graphene [30], as shown in Fig 2.25. By utilizing the ideal optical behaviour and electrical characteristics of graphene, the authors demonstrate a highly adjustable sensor capable of achieving superior refractive index sensitivity in the terahertz (THz) and infrared regions.

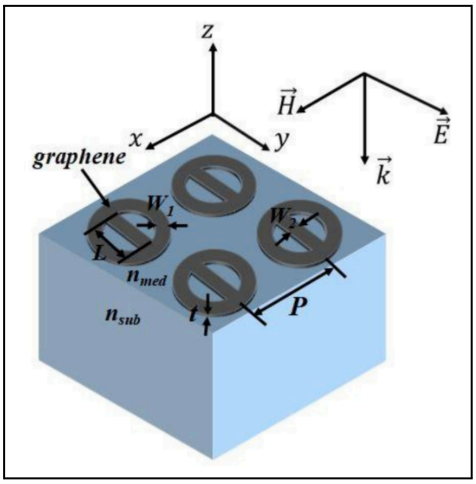

Fig. 2.25 Design of sensor

The design allows for dynamic control of plasmon resonance through modulation of graphene's Fermi level, enabling real-time tunability without altering the physical geometry of the device. Finite element method (FEM)-based simulations, shown in Fig. 2.26, reveal strong resonance peaks and high field confinement at the graphene–dielectric interface, confirming the device's ability to detect accurately [30].

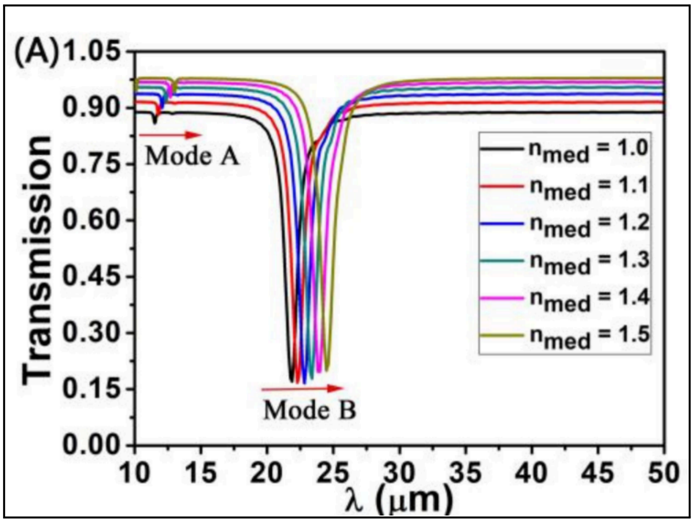

Fig. 2.26 Transmittance graph of the sensor

The study explores the influence of key design parameters such as ring radius, strip width and periodicity on the sensor's transmission spectra. The results show that varying the Fermi energy directly shifts the resonance wavelength, offering a convenient approach to tune the operational frequency range. This tunable nature enhances the flexibility of the sensor for various sensing applications, including chemical, biological and environmental detection.

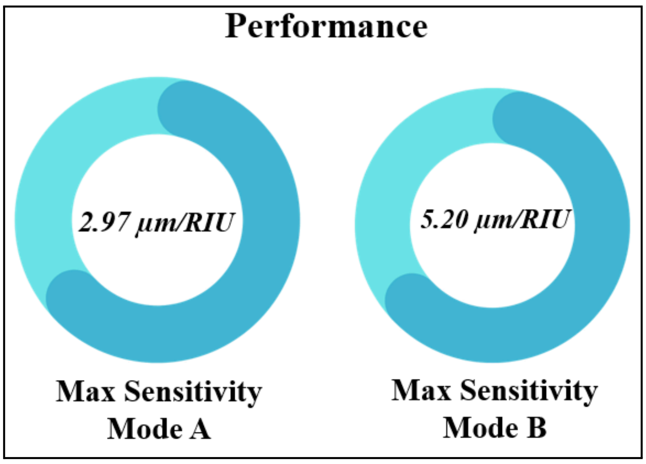

Fig. 2.27 Different performance metrics

The paper also reports a high FOM and narrow FWHM, attributed to the superior carrier mobility and low optical losses in graphene. Compared with traditional noble metal-based plasmonic sensors, the graphene-based nanoring-strip structure provides improved controllability and integration potential with modern optoelectronic systems [30]. The performance characteristics are shown in Fig. 2.27.

Furthermore, the authors highlight the compatibility of the proposed structure with current micro or nano-fabrication technologies, making it suitable for scalable production and on-chip integration. The sensor's reconfigurability through electrical biasing opens possibilities for adaptive and multifunctional sensing platforms capable of operating across a wide spectral range. The study concludes that graphene's exceptional tunability and optical confinement make it a promising alternative to metal-based plasmonic materials, particularly for applications requiring dynamic control and high detection precision.

Overall, the findings establish a solid foundation for the development of next-generation, tunable plasmonic sensors optimized for real-time monitoring in diverse scientific and industrial domains [30].

2.2.11 Applications & advantages of plasmonic RI sensors

Silicon (Si) based plasmonic RI sensors have garnered significant praise due to their high sensitivity, compactness and compatibility with existing semiconductor technology. These sensors exploit the strong confinement of SPPs at the Si-metal interface, enabling very accurate detection of minimal changes in the surrounding refractive index. For example, n-doped silicon plasmonic structures have demonstrated sensitivities up to 4900 nm/RIU, outperforming many traditional metal based sensors [28].

Their integration with standard CMOS fabrication processes allows scalable production and miniaturization, making them suitable for on-chip applications [31]. Innovative designs, such as metal-insulator-metal waveguides with square-ring or concentric-ring resonators, enhance performance by optimizing resonance characteristics [32].

The applications of Si based plasmonic RI sensors span a large variety of application grounds. In biosensing, the designed sensors can detect biomolecules like glucose, dopamine and other disease related markers by tracking changes in the refractive index of biological fluids [33]. Environmental monitoring also benefits from Si plasmonic sensors, which can detect pollutants such as nanoplastics or toxins in water with high sensitivity [31].

Chemical sensing applications leverage their precise refractive index detection to identify various chemicals in laboratory or industrial settings [28]. Overall, Si based plasmonic sensors combine high sensitivity, tunability and integration potential, making them versatile tools in modern sensing technologies.

2.2.12 Identified research gaps

Despite the progress in plasmonic sensor development, several research gaps remain, which can be listed to be -

Co-optimization of geometry and material properties

While individual optimization of structural geometry and material properties has been extensively studied, there is a lack of comprehensive research that simultaneously considers both aspects to enhance sensor performance. Recent studies have focused on optimizing plasmonic nanostructures to achieve high sensitivity and quality factor by adjusting geometric parameters and material properties [34].

Under-utilization of CMOS compatible materials

Materials like Titanium nitride (TiN) [17] and Zirconium nitride (ZrN) [16] offer promising plasmonic properties and are compatible with CMOS fabrication processes. But their application in biosensing remains limited. Research has shown TiN films can be tuned to enhance plasmonic properties, making them suitable for sensor applications.

Surface fouling and stability in biological media

Surface fouling due to nonspecific adsorption of biomolecules is a significant challenge in plasmonic sensing. Effectiveness of antifouling technology in complex biological media needs further investigation. Studies have highlighted the importance of low-fouling substrates to prevent nonspecific adsorption and improve sensor performance [10].

Integration with microfluidic platforms

The integration of plasmonic sensors with microfluidic platforms is crucial for real-world lab-on-chip applications. But research in this area is still developing. Recent advancements have explored the integration of plasmonic biosensors with microfluidic systems [18].

To bridge the gaps, this research aims to develop a silicon-based plasmonic sensor that emphasizes material–geometry co-design and CMOS compatibility.

2.3 Re-simulation of published papers

2.3.1 Re-simulation 01

Paper Title: *"Plasmonic refractive index sensing in the early diagnosis of diabetes, anemia, and cancer: An exploration of biological biomarkers."* [7]

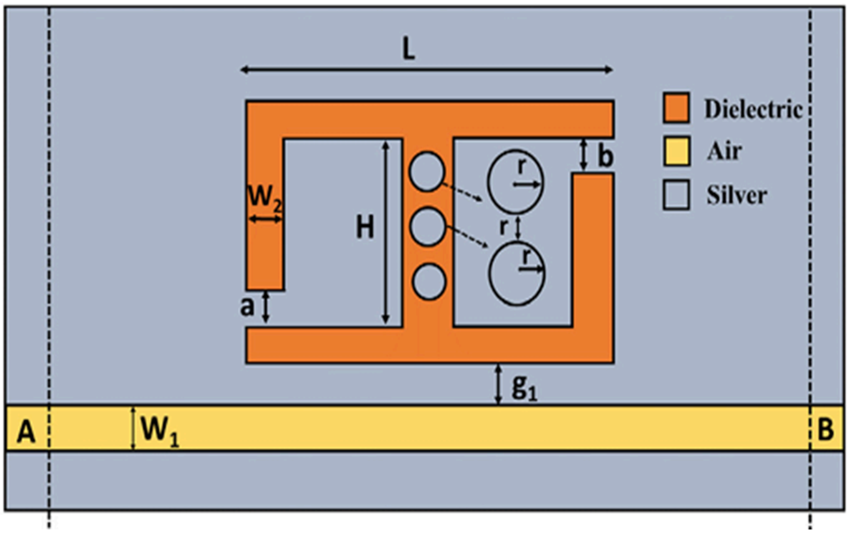

Fig. 2.28 Design of the sensor

A plasmonic RI nanosensor, shown in Fig. 2.28, was proposed along with a MIM waveguide, which was coupled with a rectangular resonator in which a silver nanorod was embedded and incorporated two baffles. By optimizing the geometry, the design achieved a high value of sensitivity measured at 2963.73 nm/RIU, with a FOM of 25.1 and a sensing resolution on the order of 3.37×10^{-7} RIU.

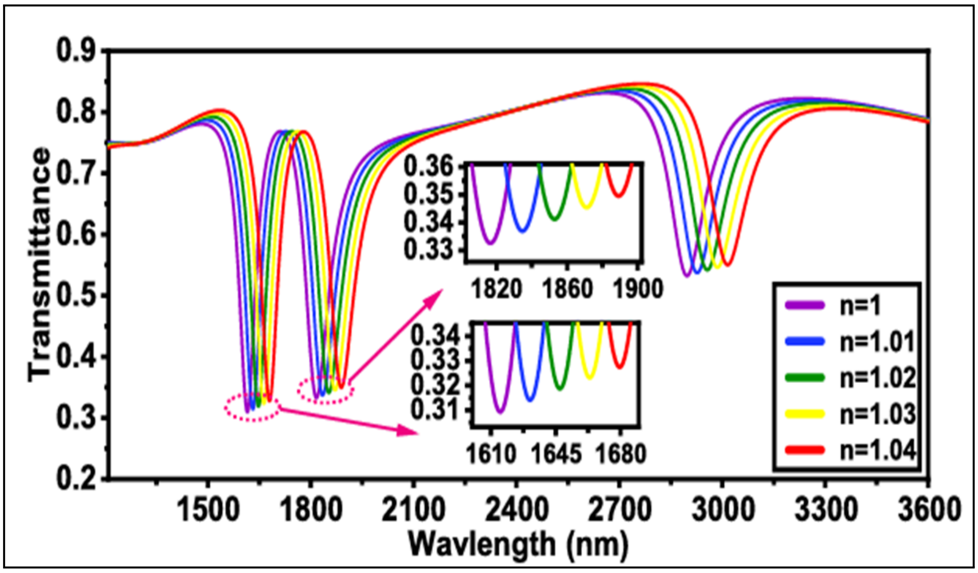

Fig. 2.29 Paper result

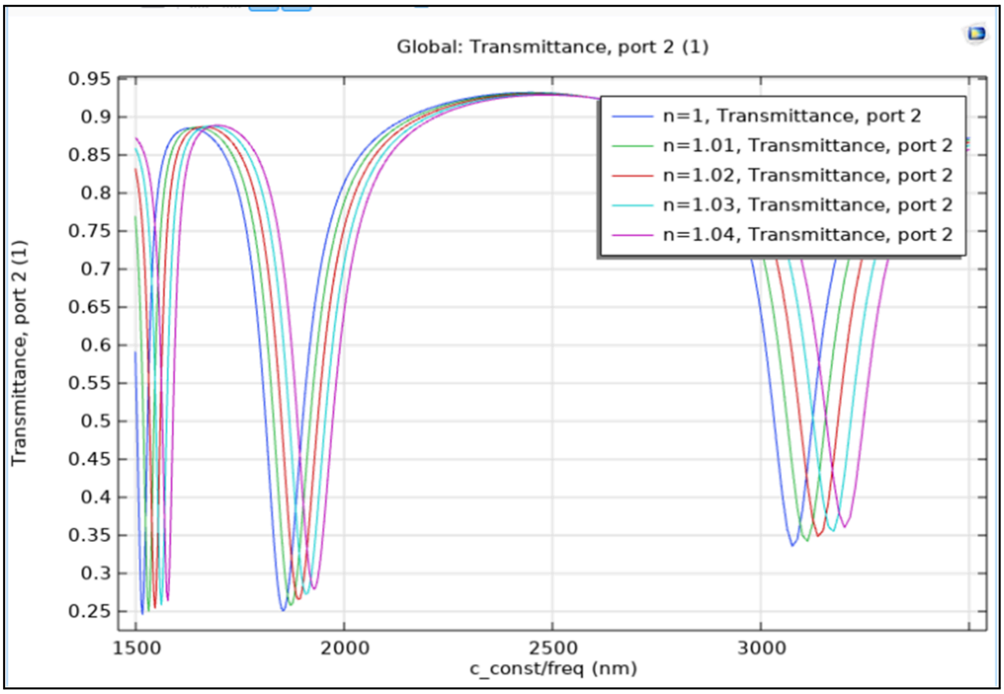

Fig. 2.30 Re-simulated result

Simulations, such as in Fig. 2.29, shows that this sensor can discriminate between different concentrations of glucose (for diabetes detection), hemoglobin (for anemia classification) and can distinguish healthy vs cancerous cells [7]. The re-simulation of this structure successfully reproduced a similar transmission spectrum, as shown in Fig. 2.30.

2.3.2 Re-simulation 02

Paper Title: *"A refractive index sensor based on an analogy T-shaped metal–insulator–metal waveguide."* [35]

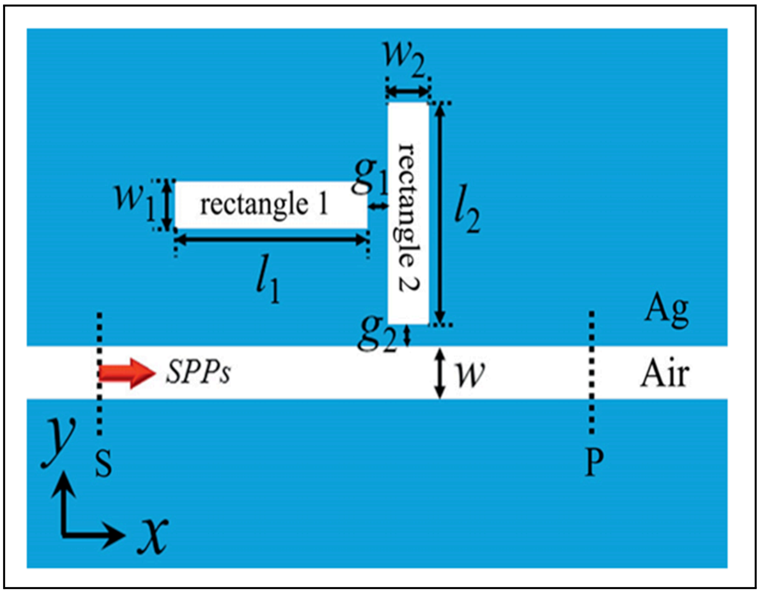

Fig. 2.31 Design of sensor

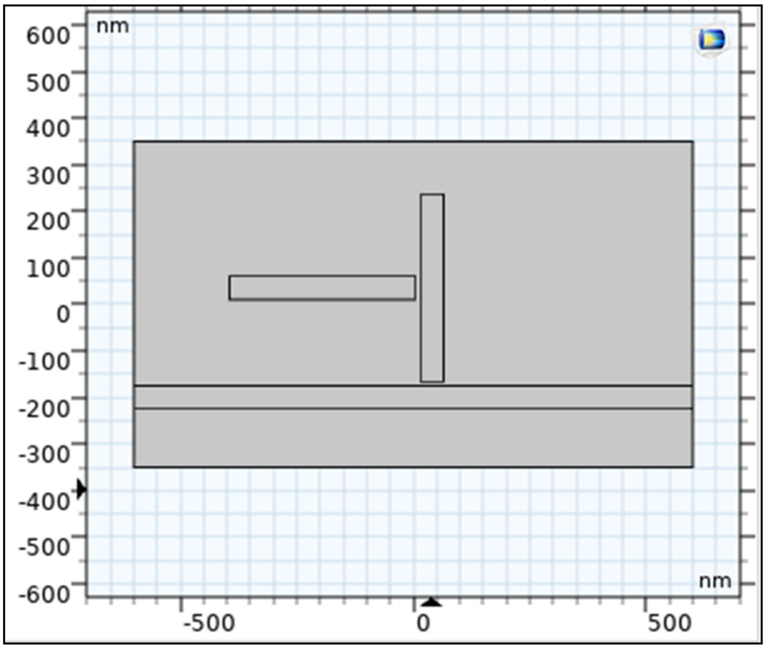

Fig. 2.32 Re-simulated design of the sensor

In the mentioned work, a plasmonic RI sensor, shown in Fig. 2.31, was proposed using a MIM waveguide coupled with a T-shaped and double ring type resonator. The re-simulated model of the sensor is presented in Fig. 2.32.

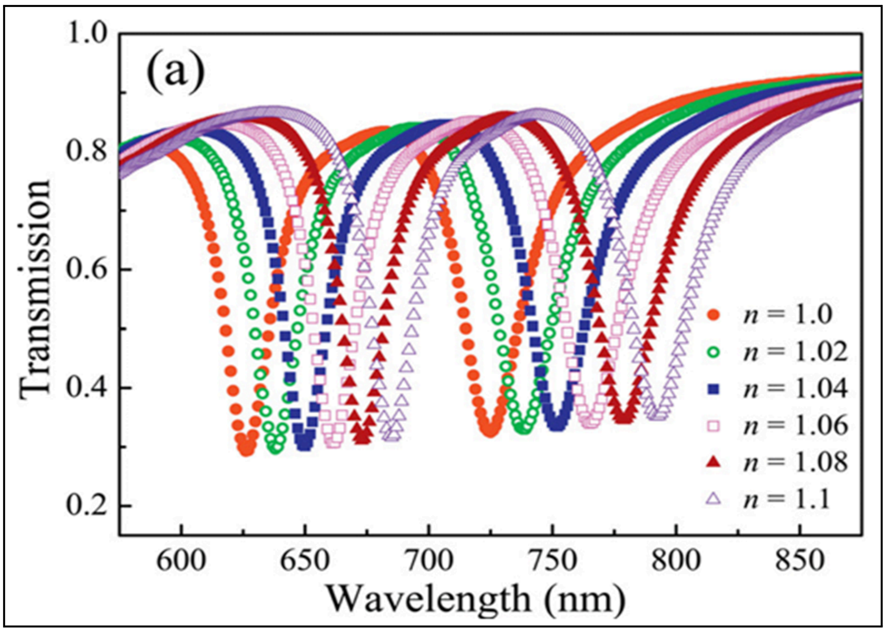

Fig. 2.33 Paper result

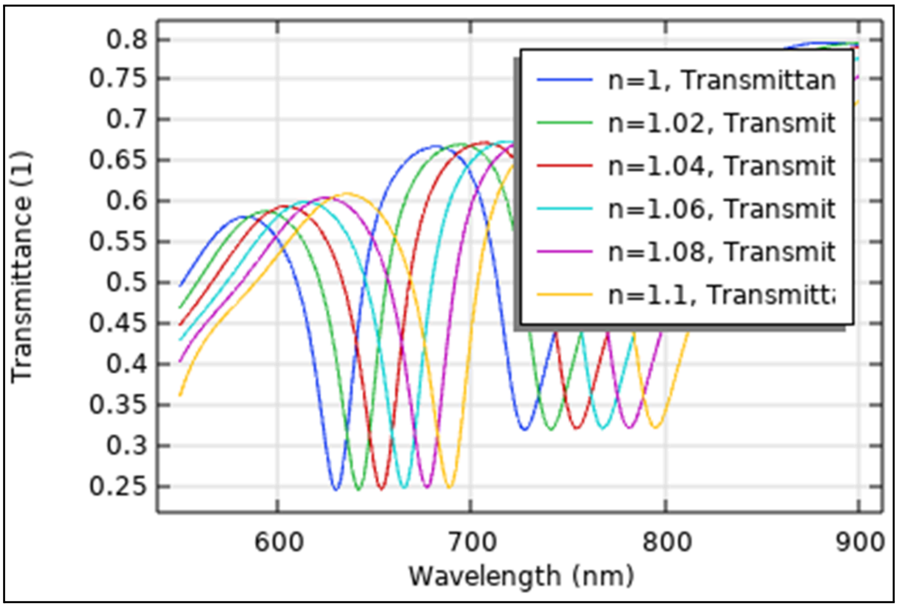

Fig. 2.34 Re-simulated result

By exploiting dual Fano resonances, in Fig. 2.33, the design achieved high sensitivity (1110 nm/RIU) and an exceptional FOM (1904). Simulations also showed potential for plasma and glucose detection, though practical use is limited by fabrication challenges and lack of experimental validation [35]. The re-simulation of this structure successfully reproduced a similar transmission spectrum, as shown in Fig. 2.34.

2.3.3 Re-simulation 03

Paper Title: *"Highly Sensitive Plasmon Refractive Index Sensor Based on MIM Waveguide."* [21]

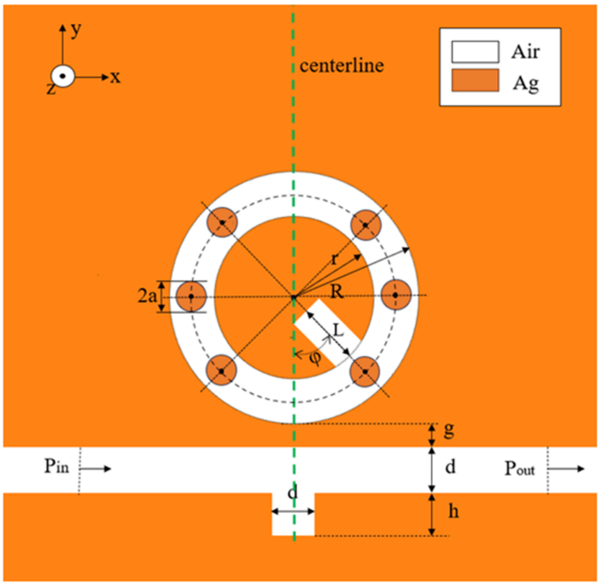

Fig. 2.35 Design of sensor

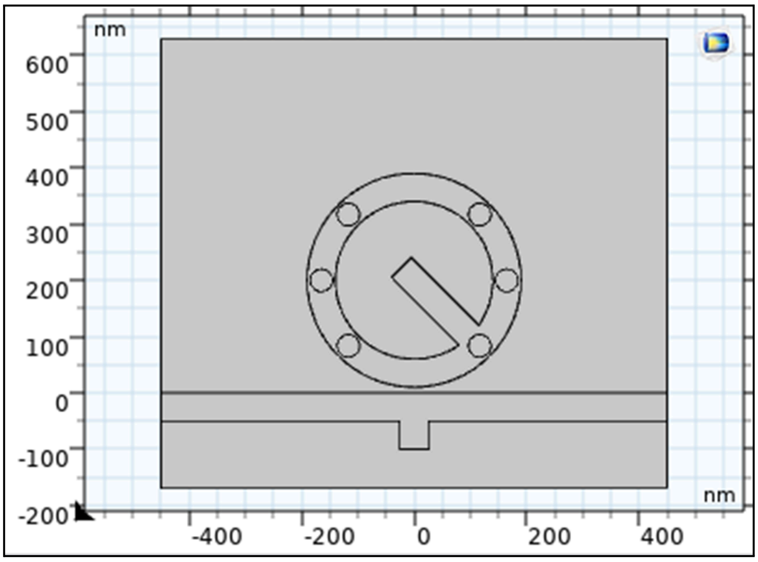

Fig. 2.36 Re-simulated design of the sensor

A plasmonic RI sensor, presented in Fig. 2.35, was presented based on a MIM waveguide that had been coupled with a hybrid structure with cavity, exploiting Fano resonance to achieve high sensitivity (3240 nm/RIU) and a FOM of 50. The re-simulated model of the sensor is presented in Fig. 2.36.

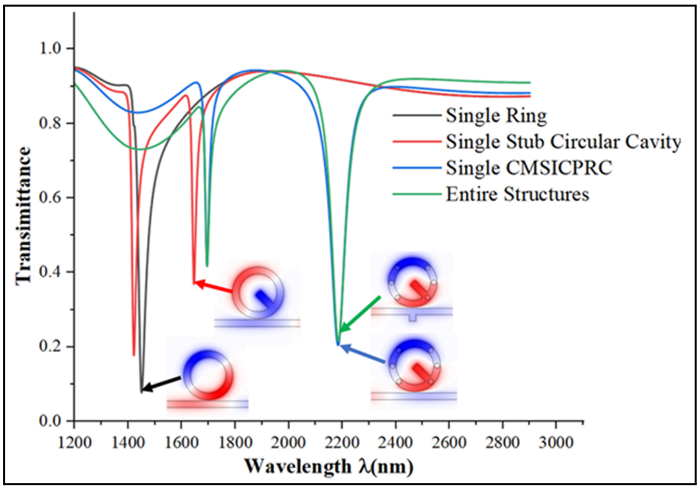

Fig. 2.37 Paper result

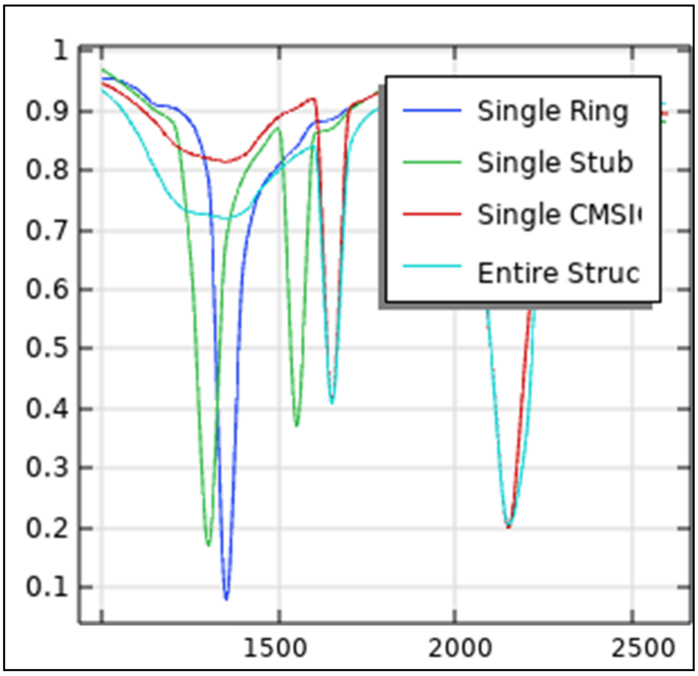

Fig. 2.38 Re-simulated result

Using FEM simulations, such as in Fig. 2.37, cavity parameters were optimized and it demonstrated potential for hemoglobin detection with sensitivity of 0.82 nm/g·L^{-1}. While the design showed excellent theoretical performance, it remains limited by fabrication challenges and lack of experimental validation [21]. The re-simulation of this structure successfully reproduced a similar transmission spectrum, as shown in Fig. 2.38.

2.4 Framework and strategy

The framework of this research, illustrated in Fig. 2.39 follows a structured approach, beginning with the conceptual basis, where the fundamental principles of plasmonics, surface plasmon resonance (SPR) and refractive index sensing were reviewed to establish the working mechanism of the sensor.

Next, an extensive literature review was carried out to identify the limitations of existing plasmonic sensors, especially those based on noble metals and to explore alternative materials such as doped silicon, TiN and ZrN that offer better CMOS compatibility and lower cost [20], [2], [9].

The study then proceeded with re-simulation of published designs to validate previous findings and benchmark performance parameters such as sensitivity, Q-factor and resonance shift [7], [8]. These results provided a foundation for identifying potential improvements.

Based on the insights gained, the motivation and objectives of the research were defined, focusing on developing a silicon-based plasmonic sensor with enhanced sensitivity, scalability and suitability for biomedical and environmental applications.

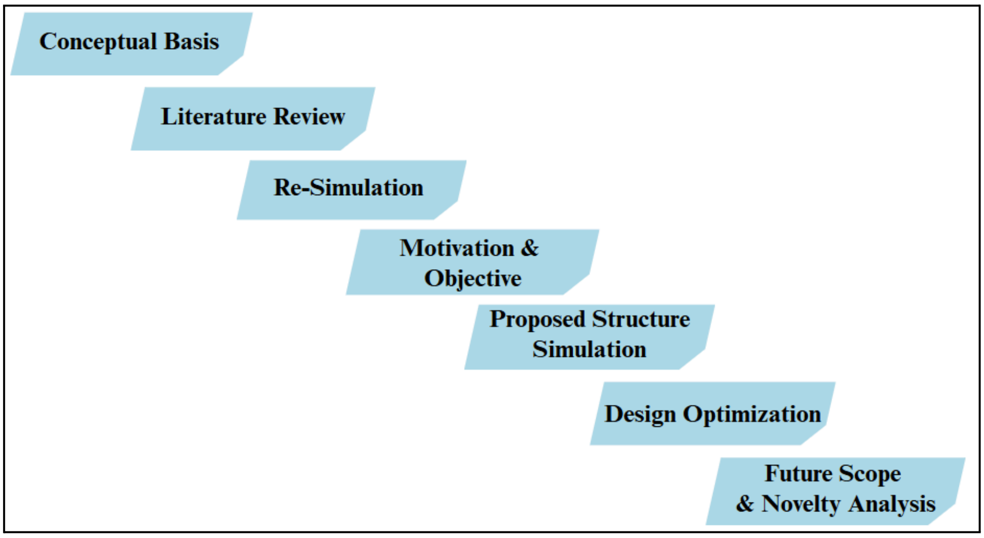

Fig. 2.39 Framework & Strategy

The core of the strategy involves designing and simulating the proposed structure using COMSOL Multiphysics. The structure was modeled with carefully assigned materials, boundaries and ports, followed by frequency-domain simulations to study resonance characteristics under different refractive index conditions.

Subsequently, design optimization was performed through systematic parametric sweeps of critical dimensions (resonator radius, grating spacing and coupling gaps). This allowed evaluation of trade-offs and identification of geometries that maximize sensor sensitivity and minimize loss.

Finally, the research included a future scope and novelty analysis, highlighting potential integration with microfluidic platforms for lab-on-chip applications, multiplexed biosensing arrays and CMOS-compatible fabrication strategies that can support large-scale deployment.

CHAPTER 3
MAIN WORK

3.1 Sensor design

The core principle behind the proposed sensor design is the excitation of SPPs at the interface between a plasmonic material (for this design, n-type doped silicon or n-Si) and a dielectric. When the refractive index or n of the surrounding medium changes, the resonance condition of the SPPs shifts correspondingly. This spectral shift forms the basis of sensing n and enables the detection of biomolecular interactions without requiring fluorescent or chemical labels.

The present work focuses on numerically designing and optimizing an n-Si based plasmonic sensor to achieve high sensitivity and resolution. The goal is to identify the optimal geometry and material parameters that maximize field confinement, enhance resonance sharpness and improve the sensor's overall performance.

3.1.1 General overview of the structure

The proposed plasmonic sensor employs a waveguide-resonator configuration in which n-type silicon (n-Si) serves as the plasmonic core material. When light interacts at the interface of n-Si and the surrounding dielectric, SPP modes can be efficiently excited.

The design integrates a waveguide format coupled with a circular dielectric ring resonator, supported by dielectric gratings for initial design or dielectric pillars for modified designs to enhance field confinement and resonance quality. This configuration supports strong localization of electromagnetic energy within the ring region, allowing spectacular dips of resonance in the transmission spectrum.

The geometry and arrangement of the dielectric features were optimized to achieve high sensitivity, figure of merit (FOM) and spectral resolution. Modifying structural parameters, such as ring radius, pillar height or coupling gap, affects the dispersion of the SPPs and consequently tunes the resonant modes.

3.1.2 Material selection

n-Doped silicon (n-Si) is selected as the plasmonic material because it can exhibit metallic (negative permittivity) behavior at near-infrared and mid-infrared wavelengths when appropriately doped. Compared with noble metals, n-Si offers lower losses, good stability and better integration for standard CMOS fabrication. These properties make it highly suitable for large-scale and integrated photonic sensor applications.

The dielectric medium serves as the sensing layer and its refractive index (n) is varied in simulations to represent different analytes. Changes in this n induce corresponding shifts in the wavelength of resonance. Air is used as the cladding layer for the waveguide structure.

3.1.3 Working principle

The device is optimised to work on the principle of surface plasmon resonance or SPR, where incident light at a specific wavelength excites SPPs at the n-Si dielectric interface [42]. Variations in n of the neighbouring medium modify the SPP dispersion relation and shift the wavelength of resonance by biomolecule binding. This enables label-free biosensing based solely on optical interrogation.

3.1.3.1 *lorentz–drude model*

Plasmonic materials interact strongly with light due to their magnetic permeability (μ) and dielectric permittivity (ε). For optical frequency values, (μ) is approximately unity, so the optical response is governed primarily by the complex value of ε. For highly doped n-type silicon or n-Si, this permittivity is frequency-dependent and the optical properties of n-Si can be more accurately illustrated by the help of Lorentz–Drude model, in which the Drude model for free carriers is combined with the Lorentz model for bound-electron oscillations.

The complex dielectric function of n-Si is expressed as,

$$\varepsilon(\omega) = \varepsilon_{\infty} - \frac{\omega_p^{2}}{\omega^{2}(1 + i\frac{1}{\omega\tau})} \tag{3.1}$$

where ε_∞ is the high-frequency permittivity of silicon, τ is the relaxation time for the electron/hole, ω_p is the plasma frequency of free carriers and $\omega = \frac{2\pi c}{\lambda}$ is the angular frequency of the incident light. The plasma frequency and relaxation time can be shown to be connected to the material properties for highly doped semiconductors by,

$$\omega_p^2 = \frac{Ne^2}{\varepsilon_0 m_{eff}} \tag{3.2}$$

$$\tau = \frac{\mu m_{eff}}{e} \tag{3.3}$$

where N is the concentration of free-carrier , m_{eff} is the effective carrier mass, μ is the mobility of carrier, e is the charge of electron and ε_0 is the permittivity of vacuum. Separating the real parts and the imaginary parts, the dielectric function becomes,

$$\varepsilon(\omega) = \left[\varepsilon_\infty - \frac{\omega_p^2\tau^2}{1+\omega^2\tau^2}\right] + i\,\frac{\omega_p^2\tau}{\omega(1+\omega^2\tau^2)} \tag{3.4}$$

(Real) (Imaginary)

Here, the real part determines the material's energy storage capability (dispersion), while the imaginary part represents energy losses (absorption). Crossing a certain value of doping as threshold, the real part of n-Si's permittivity can become negative, satisfying the fundamental goal of supporting surface plasmon polariton or SPP excitation as well as SPP propagation.

The refractive index of n-Si is related to the dielectric function by,

$$n = \sqrt{\frac{|\varepsilon| + Re(\varepsilon)}{2}} \tag{3.5}$$

$$\kappa = \sqrt{\frac{|\varepsilon| - Re(\varepsilon)}{2}} \tag{3.6}$$

where n is the real part of the refractive index (phase velocity) and κ is the imaginary part or extinction coefficient. Both parameters vary with wavelength and carrier concentration, directly affecting SPP confinement and propagation characteristics.

3.1.3.2 ***waveguide modes and dispersion***

For subwavelength n-Si waveguides, only the fundamental transverse magnetic (TM) mode is typically supported, which enables SPP excitation from the input port. The effective value of n or n_{eff} depends on both the geometry of the waveguide and the material's dielectric properties for the mode.

In a configuration of MIM kind, the TM mode dispersion relation can be expressed as,

$$\varepsilon_d \sqrt{n_{eff}^2 - \varepsilon_m}\, tanh(\frac{\pi W}{\lambda} \sqrt{n_{eff}^2 - \varepsilon_d}) + \varepsilon_m \sqrt{n_{eff}^2 - \varepsilon_d}) = 0 \quad (3.7)$$

where ε_d is the sensing medium permittivity, ε_m is that of n-Si, λ is the operating wavelength and W is the width for the waveguide. From Maxwell's equations, n_{eff} can also be calculated by,

$$n_{eff} = \frac{\beta_{SPP}}{k_0} \quad (3.8)$$

$$k_{d,m} = \sqrt{\beta_{SPP}^2 - \varepsilon_{d,m} k_0^2} \quad (3.9)$$

where β_{SPP} is propagation constant for the SPP and $k_0 = \frac{2\pi}{\lambda}$ is the free-space wavenumber.

3.1.3.3 ***resonance condition of the plasmonic resonator***

The resonance wavelength of the ring or rectangular resonator is determined by standing wave conditions along the optical path,

$$\lambda_{res} = \frac{2 n_{eff} L}{m - \phi_{ref}/\pi} \quad (3.10)$$

where λ is the resonator's effective length, m is the order of the mode and ϕ_{ref} can be said to be the shift of phase due to SPP propagation.

Surrounding n value change modifies n_{eff}, which as a result shifts the wavelength of resonance. This wavelength shift underpins refractive index sensing in n-Si based plasmonic devices, allowing detection of subtle changes in the dielectric environment.

3.2 Sensor implementation

The sensor implementation involves the systematic setup, modeling and integration of plasmonic components to enable accurate detection of biological analytes.

3.2.1 Design initialization

The numerical simulation is performed using COMSOL Multiphysics 6.2 which utilises the FEM method. The simulation begins by defining the sensor geometry composed of n-doped silicon (n-Si) as the plasmonic material, a dielectric sensing layer and an air region. The structure includes the waveguide, resonator and periodic dielectric gratings or dielectric pillars, modeled using predefined geometric parameters.

Most metal–insulator–metal (MIM) and similar plasmonic sensors are accurately analyzed using 2D models, particularly when the structure height exceeds 800 nm [46]. When the device height surpasses this threshold, 2D simulation results can be extrapolated to represent 3D behavior effectively, maintaining nearly identical performance characteristics [47], [48].

3.2.2 Material assignment

The materials for the sensor hold significant importance and need to be defined appropriately for proper working of the sensor.

3.2.2.1 *material - 1 : n-Si*

It is applied as the sensor substrate, acting as the plasmonic medium.

3.2.2.2 *material - 2 : dielectric (analyte layer)*

It models the sensing environment, whose refractive index (n) is varied to simulate analyte induced optical responses.

3.2.2.3 *material - 3 : Air*

It forms the cladding and ensures strong confinement of SPP modes.

This configuration supports the excitation and propagation of transverse magnetic (TM) surface plasmon polaritons along the n-Si and dielectric interface.

3.2.3 Boundary conditions and port definition

Input and output ports are defined at both ends of the waveguide to excite and detect SPPs, respectively. Scattering boundary conditions are applied to absorb outgoing waves and suppress artificial reflections, preventing interference and ensuring accurate field propagation within the computational domain.

3.2.4 Mesh generation

An extra-fine triangular mesh is applied, particularly in the regions of high field variation, such as the resonator cavity and dielectric gratings to enhance numerical precision. FEM divides the simulation domain into discrete finite elements, enabling accurate numerical solutions to the governing electromagnetic partial differential equations (PDEs) and ensuring reliable field distribution analysis [26], [49].

3.2.5 Study configuration

A frequency-domain study is performed to analyze the spectral response of the sensor. The frequency (or wavelength) range is set within the near-infrared region, where surface plasmon resonance (SPR) phenomena and biological detection sensitivity are most prominent.

3.2.6 Parametric sweep

To evaluate sensing performance, a parametric sweep is conducted by varying the n of the dielectric environment. This simulates practical changes in biological analyte concentration and allows monitoring of resonance wavelength shifts in the transmittance spectrum.

3.2.7 Output and analysis

The output is represented as transmittance vs. wavelength plots for each refractive index value. The shift in resonance dips provides quantitative data to compute sensitivity (S), resolution (R) and FOM. These metrics determine the sensor's efficiency in detecting refractive index variations and help identify the optimal geometry for maximum performance.

3.2.8 Performance metrics of the sensor

The proposed plasmonic sensor performance is evaluated by making use of several key metrics that collectively describe its optical response, detection capability and practical feasibility.

3.2.8.1 *transmittance*

The transmittance of a refractive index (RI) sensor can be explained as the ratio of the output optical power P_{out} to the incident optical power P_{in} .

$$Transmittance = \frac{P_{out}}{P_{in}} \tag{3.11}$$

Transmittance quantifies how much amount of light is being allowed to pass through the sensor. A lower transmittance indicates stronger interaction between the propagating optical field and the sensing medium, which is often desirable for enhancing light–matter interaction in plasmonic devices.

3.2.8.2 *sensitivity*

Sensitivity (S) is one of the key parameters when considering the case of RI sensors, measuring how effectively the sensor detects variations in n. It is defined as the shift in the wavelength of resonance ($\Delta\lambda_{res}$) for a per unit change in n (Δn).

$$S = \frac{\Delta\lambda_{res}}{\Delta n} \tag{3.12}$$

The sensitivity of a sensor is strongly influenced by its structural geometry. Optimizing the resonator design and maximizing the interaction between the optical field and the material under scrutiny can significantly enhance sensitivity.

High value of sensitivity is critical for identifying subtle changes in biomolecular concentrations, such as glucose or hemoglobin, which are important for early disease diagnostics.

3.2.8.3 *figure of merit*

The FOM evaluates the sensor's performance as a whole, by considering both sensitivity value and value of spectral sharpness. It is explained as ratio between the sensitivity to the FWHM of the peak resonance,

$$FOM = \frac{S}{FWHM} \tag{3.13}$$

A high FOM means the sensor has the ability to find out small changes in n with high precision, reflecting strong confinement of surface plasmon polaritons (SPPs) and efficient light–matter interaction.

3.2.8.4 *sensing resolution*

Sensing resolution or SR demonstrates the smallest possible value of change in n which can be accurately detected by the sensor. It depends on both the sensor's sensitivity and the resolution of the measurement system, such as the optical spectrum analyzer,

$$SR = \frac{\Delta\lambda}{S} \tag{3.14}$$

Here, $\Delta\lambda$ represents the minimum resolvable wavelength shift. High resolution enables detection of very minor variations in the dielectric environment, which is essential for high precision biosensing.

3.2.8.5 *quality factor*

The quality factor measures the sharpness of the sensor's peak resonance. It is defined as a ratio of wavelength of resonance λ_{res} to the resonance FWHM,

$$Q = \frac{\lambda_{res}}{FWHM} \tag{3.15}$$

A higher Q-factor indicates narrower resonance peaks, which enhance both sensitivity and resolution, contributing to the overall performance and reliability of the sensor.

3.2.8.6 *cmos compatibility*

The use of n-doped silicon as the sensing material provides full CMOS process compatibility, enabling low-cost fabrication and easy integration with existing electronic and photonic circuitry. This makes the sensor suitable for scalable production and practical deployment in commercial biosensing applications.

3.3 Experimentation & simulation

All analyses were conducted through comprehensive simulations of numerical type using FEM based software to model the electromagnetic behavior of the proposed n-Si plasmonic structures. The simulation framework replicates the experimental conditions virtually, enabling precise evaluation of resonance characteristics, field confinement and refractive index sensitivity.

3.3.1 Initial design

The geometric structure as well as parameters were arbitrarily selected to analyze the sensor optical performance and establish a benchmark for further optimization in the preliminary stage.

3.3.1.1 *structural overview*

The initial configuration of the plasmonic sensor that was initially designed is illustrated in Fig. 3.1 .

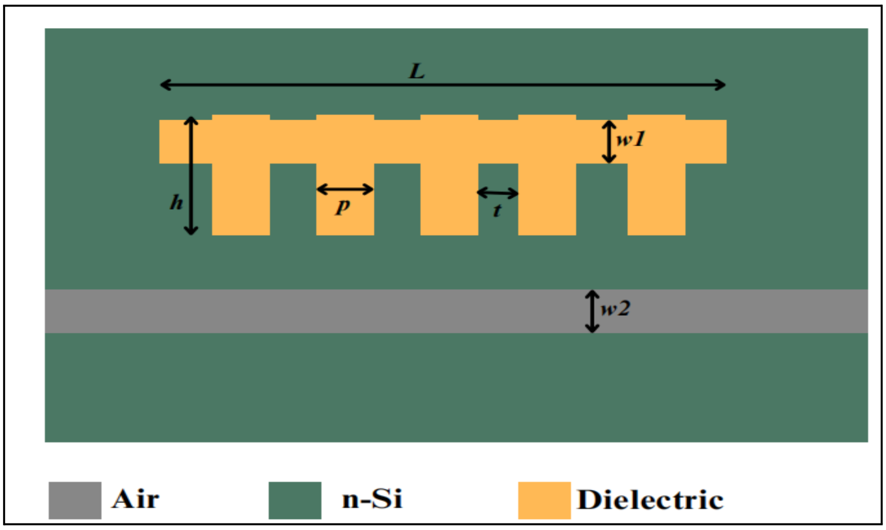

Fig. 3.1 Initial design

The structure is of a simple rectangular resonator coupled to a straight waveguide and integrated with a series of dielectric gratings. The gratings were introduced to enhance coupling of waveguide guided mode and the resonant mode within the cavity, so that better performance could be achieved.

The phenomenon of coupling of waveguide guided mode and the resonant mode within the cavity is achieved by promoting surface plasmon excitation along the n-Si and dielectric interface.

3.3.1.2 *design parameters*

The sensor geometry and material configuration utilised to investigate the fundamental resonance characteristics is listed in Table 3.1.

Table 3.1 Sensor design parameters

Parameters	Symbol	Proposed value (nm)
Length of resonator	L	280
Width of resonator	w1	35
Width of waveguide	w2	35
Width of gratings	p	35
Gap between gratings	t	15
Height of grating	h	50

The initial parameter set was chosen primarily to observe whether a measurable resonance shift could be obtained as a result of changes in the surrounding n.

3.3.1.3 *simulation*

The frequency domain simulation was carried out to analyze the optical transmittance characteristics of the initial grating based structure. The n of the dielectric sensing layer was changed from 1 to 1.3 in increments of 0.1.

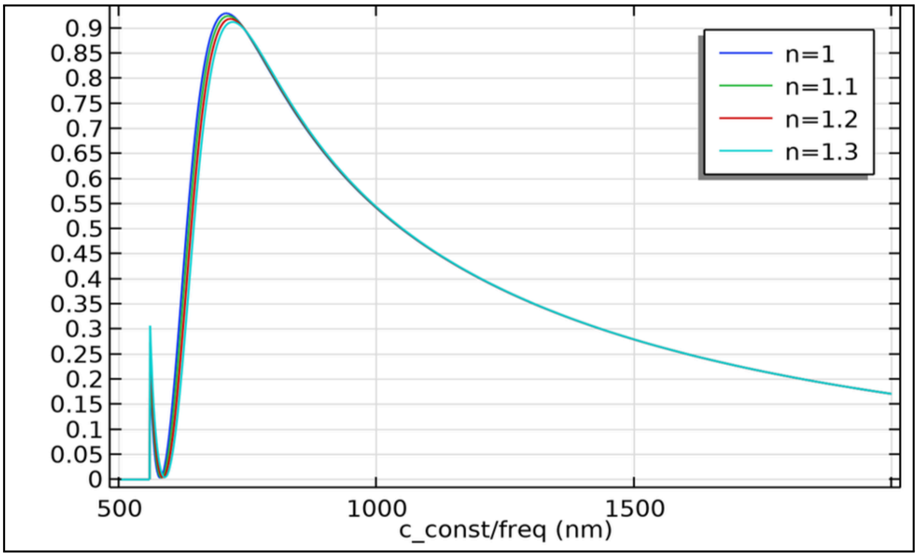

Fig. 3.2 Transmittance graph of initial design with Δn = 0.1

The resulting transmittance spectra of Fig. 3.2 revealed a single, well-defined resonance dip, confirming the excitation of a fundamental plasmonic mode within the rectangular resonator. This resonance wavelength exhibited a gradual redshift as the refractive index increased, consistent with the expected surface plasmon resonance (SPR) behavior.

3.3.1.4 *initial performance*

The single resonance dip confirmed that plasmonic resonance was successfully established, the magnitude of wavelength shift across the refractive index range was small, indicating limited sensitivity.

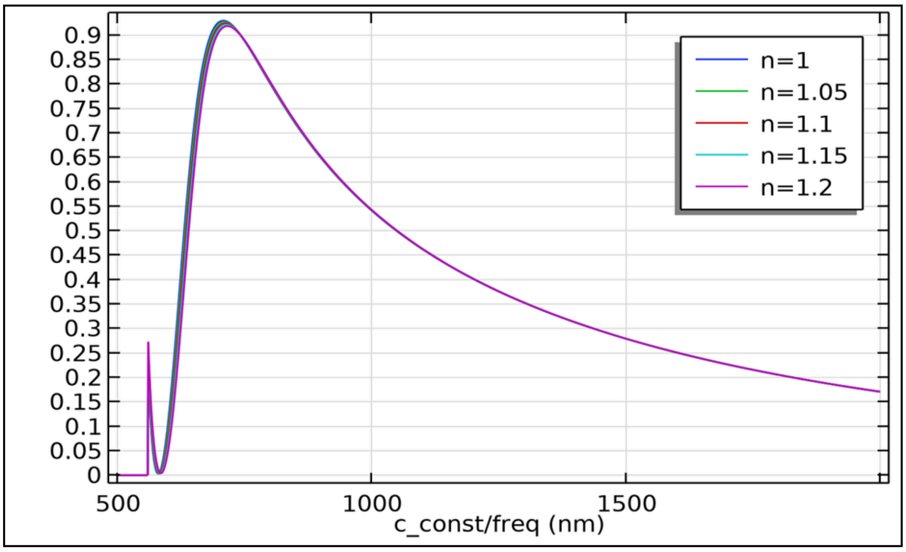

Fig. 3.3 Transmittance graph of initial design with Δn = 0.05

The overall sensitivity calculated from the resonance wavelength shift was found approximately 41.5 nm/RIU. To further investigate, the simulation was repeated using smaller refractive index steps ($\Delta n = 0.05$).

The updated results in Fig. 3.3 showed no significant improvement in resonance shift or overall sensitivity. This outcome suggested that the initial structure, while effective in supporting a basic plasmonic mode, was not optimized for strong field confinement or high refractive index responsiveness.

3.3.2 Modified design 01

The geometry was further modified to enhance light–matter interaction within the resonator, aiming to achieve greater sensitivity and a more pronounced resonance response in subsequent designs.

3.3.2.1 *structural overview*

In the design, four dielectric pillars are introduced, two on each side of the ring resonator, to form a ladder-like structure. The horizontal rectangular n-Si bars positioned at the top and bottom act as coupling regions, while the newly incorporated circular dielectric ring is embedded within the central cavity of the ladder, as shown in Fig. 3.4.

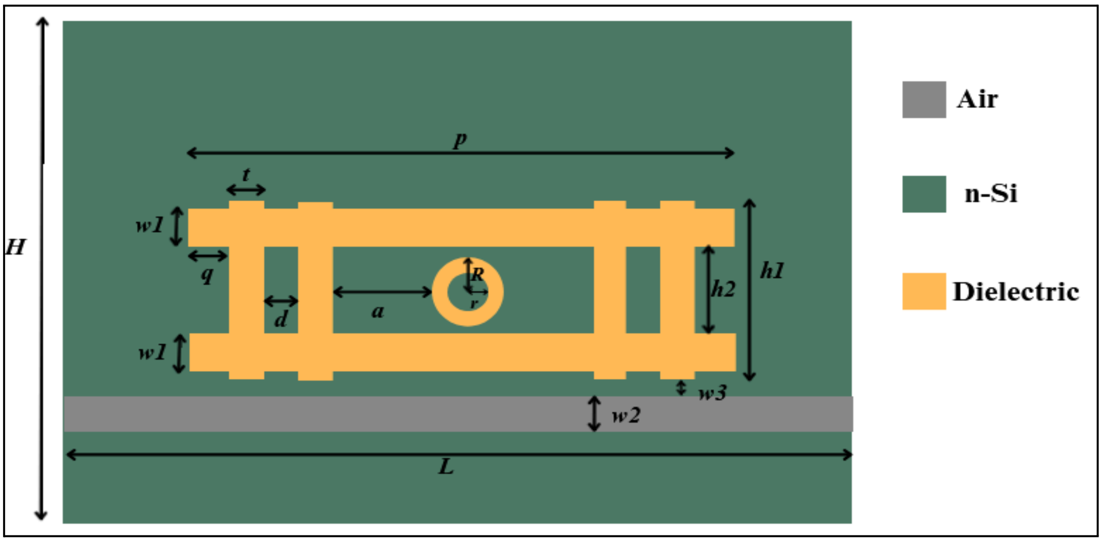

Fig. 3.4 Design of modified sensor 01

This configuration allows stronger confinement of the propagating plasmonic fields within the cavity region, effectively increasing the interaction length between the SPPs and the sensing dielectric layer. The ring serves as a resonant element, capable of supporting gap plasmon resonance (GPR) and whispering-gallery type plasmonic modes, leading to multiple resonant features in the transmission spectrum.

3.3.2.2 *design parameters*

The sensor geometry and material configuration utilised in the design is listed in Table 3.2.

Table 3.2 Sensor design parameters

Parameters	Symbol	Proposed value (nm)
Length of resonator	p	600
Width of resonator	w1	35
Width of waveguide	w2	40
Width of pillar	t	35
Gap between pillars	d	75
Height of pillar	h1	180
Distance between ring and nearby pillar	a	107.5
Inner ring radius	r	20
Outer ring radius	R	40
Gap between resonator and waveguide	w3	10
Length of waveguide	L	900
Upward length of pillar from resonator	b	7.5
Height of sensor surface	H	600
Height of pillar excluding resonator	h1	95
Extended resonator from pillar	q	32.5

3.3.2.3 *working mechanism and resonance behavior*

The introduction of the circular ring within the n-Si framework significantly modifies the propagation of SPPs along the waveguide-resonator system. The ring forms a localized plasmonic cavity, enabling the excitation of multiple coupled resonances due to the behaviour of guided mode and confined plasmonic fields.

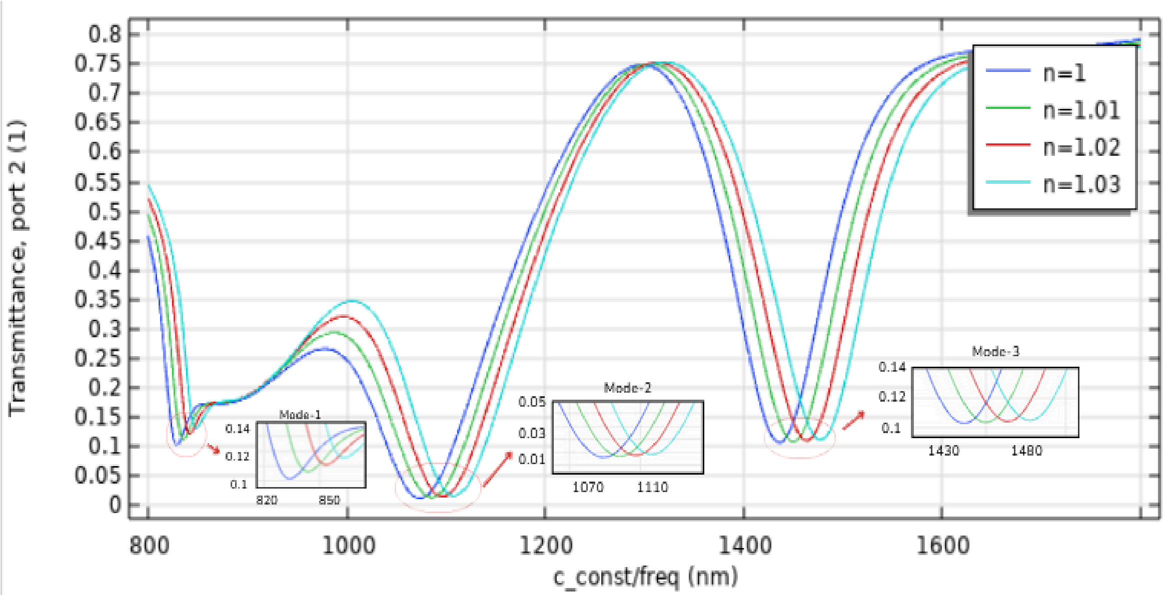

Fig. 3.5 Transmittance graph of modified design 01

As illustrated in Fig. 3.5, the transmittance spectra for varying n (from n = 1.00 to 1.03, in increments of 0.01) display three distinct resonance dips, each corresponding to a specific plasmonic resonance mode of the structure. These dips exhibit noticeable redshifts with increasing n, confirming the sensor's capability to identify subtle refractive index variations within the surrounding medium.

The variation in resonance depth and wavelength demonstrates a strong form of coupling between guided SPP mode and resonant cavity formed by the dielectric ring and pillar framework. The hybridization of modes within the ladder-like geometry enhances field localization, resulting in improved spectral response compared to the initial single-dip.

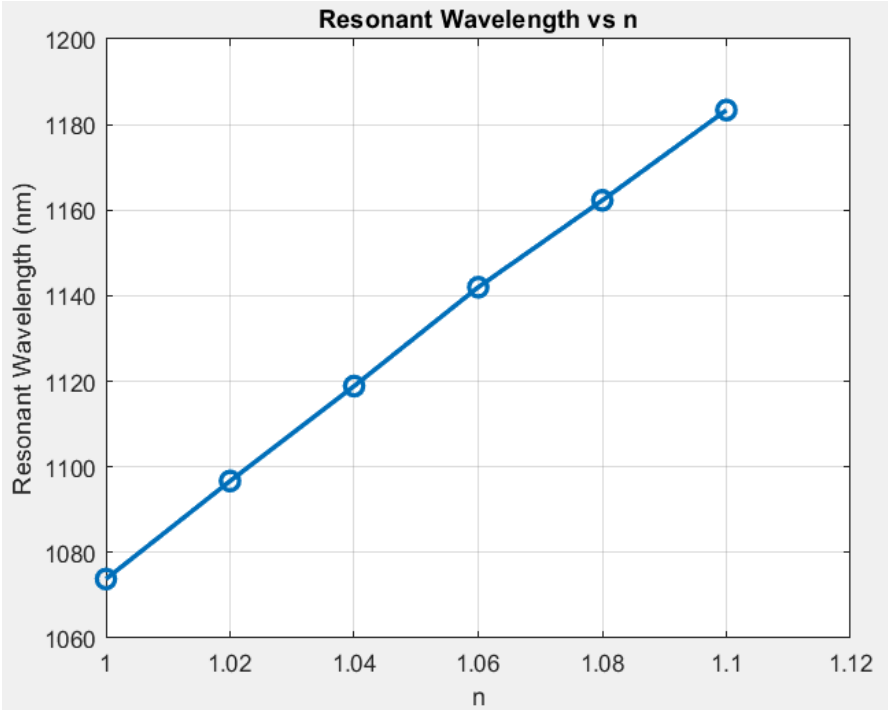

Fig. 3.6 Relation of resonant wavelength with refractive index for mode-2

The resonant wavelength vs n characteristics revealed in Fig. 3.6 shows that an increase in n results in a redshift for resonant wavelength, that is the value increases with the increase of n. This phenomenon strongly indicates enhanced light–matter interaction within the sensing region.

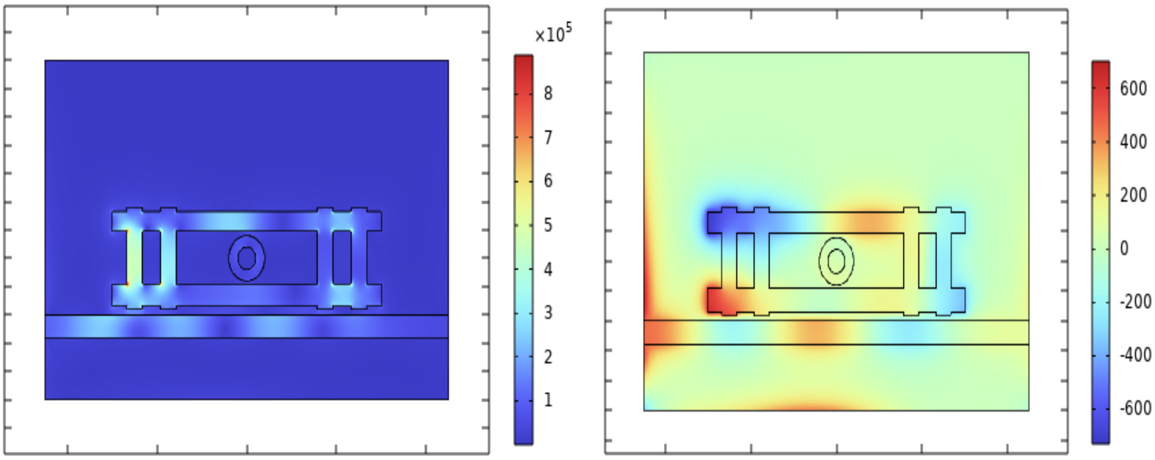

Fig. 3.7 E - field (V/m) & H - field (A/m) distribution at λ = 836.31 nm

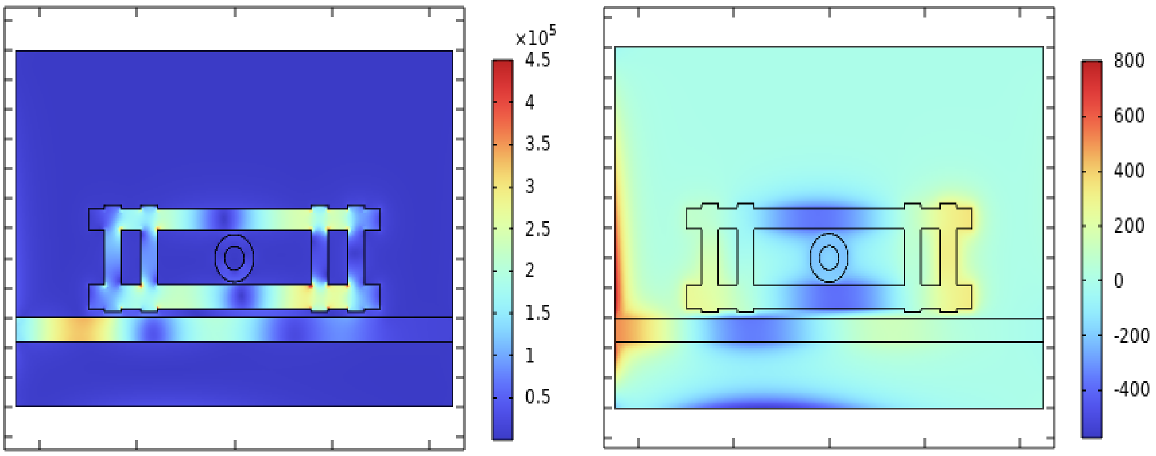

Fig. 3.8 E - field (V/m) & H - field (A/m) distribution at $\lambda = 1086.8$ nm

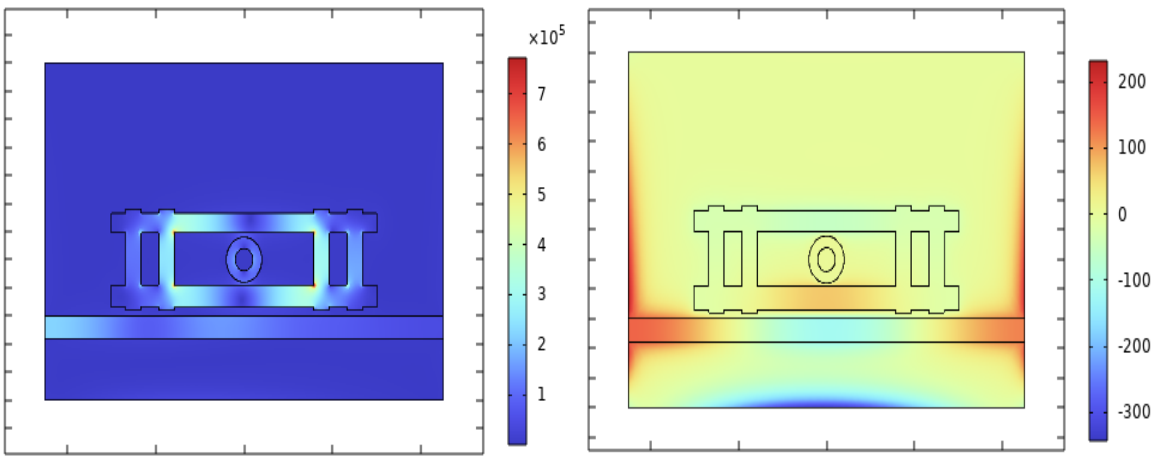

Fig. 3.9 E - field (V/m) & H - field (A/m) distribution at $\lambda = 1451.1$ nm

The electric and magnetic field for the three resonance dips, illustrated in Fig. 3.7, Fig. 3.8 and Fig. 3.9 exhibits highly confined field localization within the sensing cavity, confirming strong plasmonic coupling in the modified structure.

3.3.2.4 *performance evaluation*

The modified design exhibits a substantial improvement in sensitivity. Each of the three observed resonance dips corresponds to distinct plasmonic coupling conditions, producing sensitivities of approximately 771 nm/RIU , 990 nm/RIU, and 1180 nm/RIU respectively.

The sharpness and clear separation of these dips indicate efficient confinement and effective interaction between the SPP fields and the sensing region. While the Figure of

Merit (FOM) values for these modes require further optimization, the presence of multiple resonant features marks a significant advancement over the initial configuration.

The results confirm that the inclusion of dielectric pillars and a central circular ring not only increases field confinement but also enables multi-mode resonance tuning, offering greater flexibility and improved sensitivity for refractive index sensing applications.

3.3.3 Modified design 02

The design was further streamlined and explored to assess the influence of structural simplification on resonance characteristics and aiming to achieve enhanced mode confinement, reduced propagation loss and improved sensing performance through optimized geometry.

3.3.3.1 *structural overview*

In this structure, the bottom horizontal n-Si bar of the ladder-like configuration is removed. This modification transforms the system into a rectangular resonator that retains four dielectric pillars, two pillars each on each side of the central circular ring, as shown in Fig. 3.10.

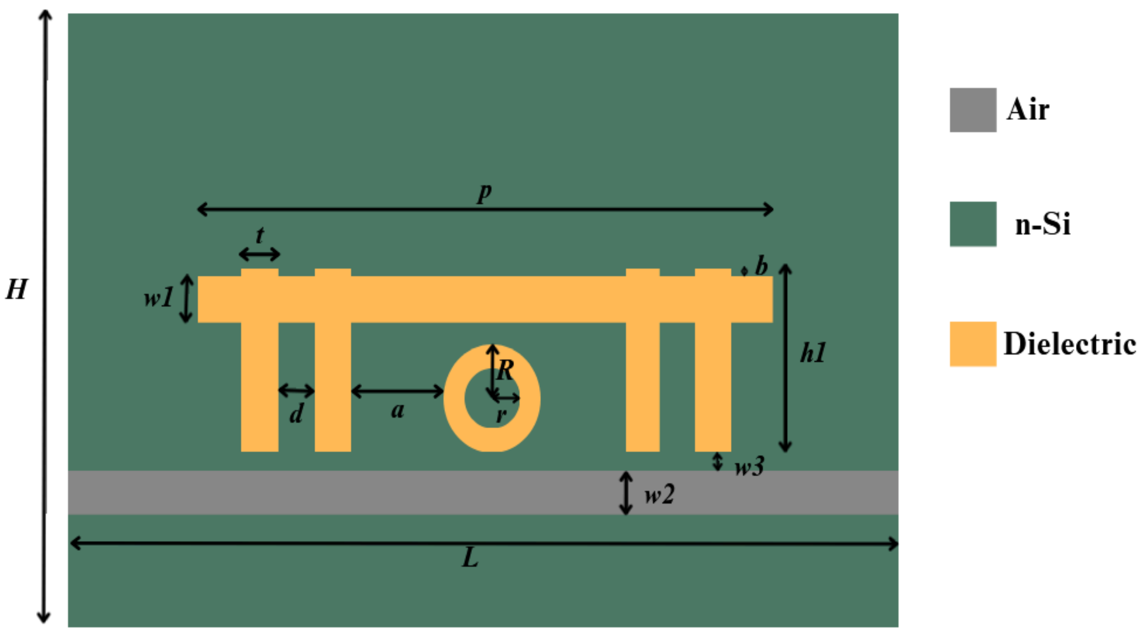

Fig. 3.10 Design of modified sensor 02

The pillars continue to facilitate field confinement around the resonator, while the circular ring serves as the primary plasmonic cavity element. This simplified structure maintains efficient light–matter interaction within a more compact footprint. By reducing the number of horizontal bars, the design allows for easier fabrication while preserving strong localized plasmonic fields around the ring and the adjacent pillars.

3.3.3.2 *design parameters*

The sensor geometry and material configuration utilised in the design is listed in Table 3.3.

Table 3.3 Sensor design parameters

Parameters	Symbol	Proposed value (nm)
Length of resonator	p	600
Width of resonator	w1	35
Width of waveguide	w2	40
Width of pillar	t	35
Gap between pillars	d	75
Height of pillar	h1	150
Distance between ring and nearby pillar	a	107.5
Inner ring radius	r	30
Outer ring radius	R	50
Gap between resonator and waveguide	w3	10
Length of waveguide	L	900
Upward length of pillar from resonator	b	7.5
Height of sensor surface	H	600

3.3.3.3 *working mechanism and resonance behavior*

The rectangular resonator with embedded ring supports coupled plasmonic modes originating from interactions between the guided surface plasmon polaritons (SPPs) and the dielectric ring.

Unlike the previous ladder-like configuration, the absence of the bottom horizontal bar reduces mode hybridization, resulting in a simpler resonance spectrum.

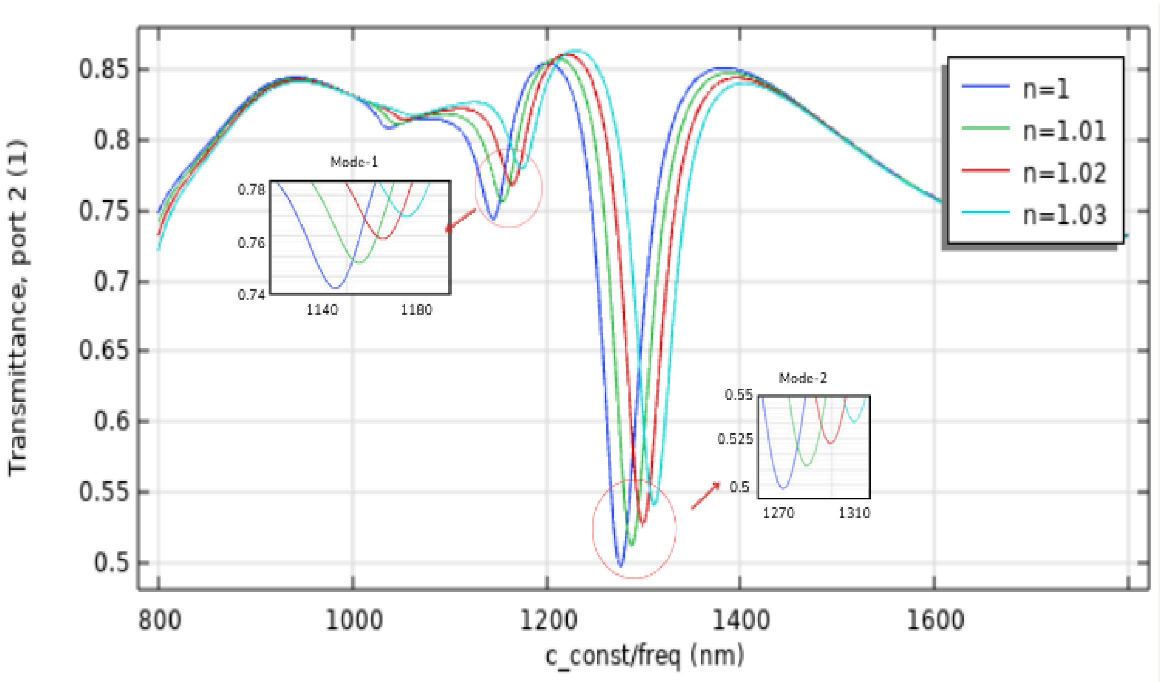

Fig. 3.11 Transmittance graph of modified design 02

As illustrated in Fig. 3.11, the simulated transmittance spectra were obtained for refractive indices ranging from n = 1.0 to 1.3, with increments of 0.1. The results reveal two distinct resonance dips, each corresponding to a unique plasmonic mode supported by the resonator.

Both dips shift toward longer wavelengths as the surrounding n increases, demonstrating the responsiveness of the sensor to changes in the environment. The spectral characteristics indicate that the two-dip configuration still preserves strong field confinement near the ring and pillars.

This result is quite similar to the initial design but the overall number of accessible resonance modes is reduced compared to the ladder-like design. The simplified structure thus provides a trade-off between fabrication complexity and multi-mode tunability.

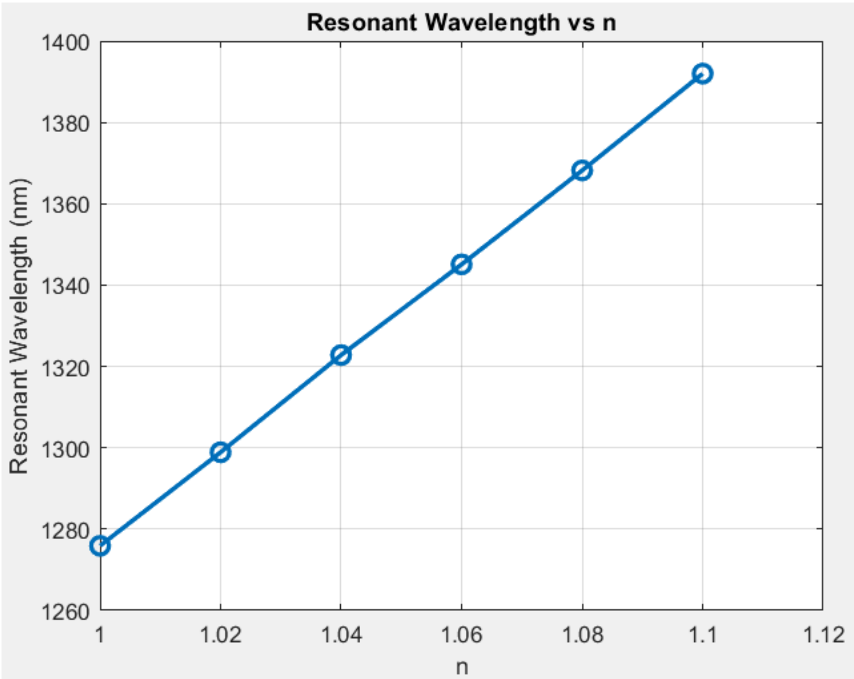

Fig. 3.12 Relation of resonant wavelength with refractive index for mode-2

The resonant wavelength vs n characteristics revealed in Fig. 3.12 shows that an increase in n results in a redshift of the wavelength of resonance, that is the wavelength of resonance increases with the increase of n. This phenomenon strongly indicates enhanced light–matter interaction within the sensing region.

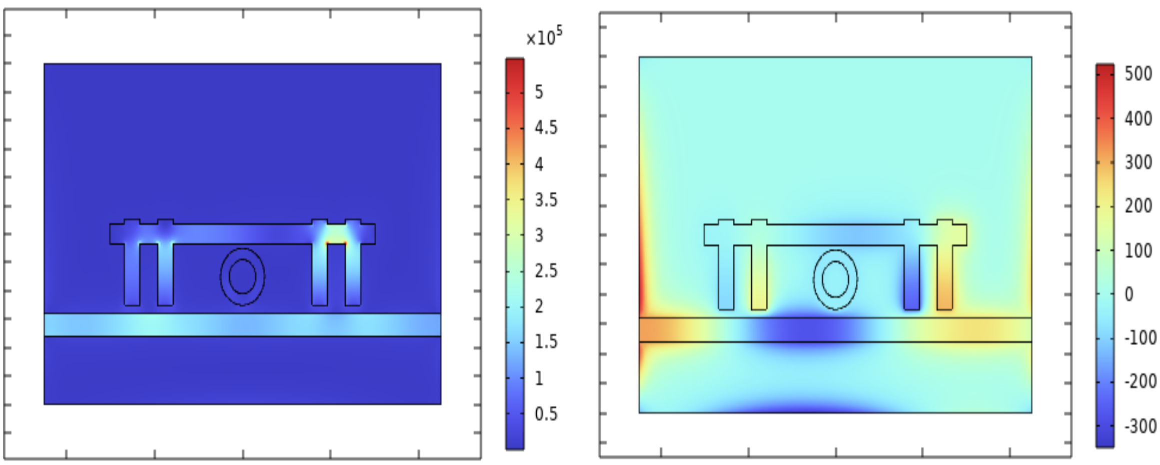

Fig. 3.13 E - field (V/m) & H - field (A/m) distribution at $\lambda = 1154.9$ nm

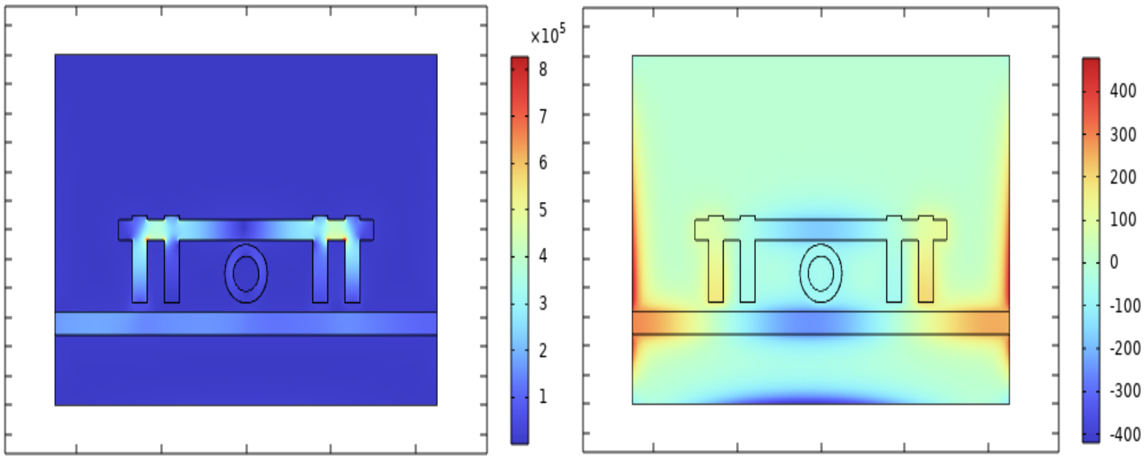

Fig. 3.14 E - field (V/m) & H - field (A/m) distribution at λ = 1287.3 nm

The electric and magnetic field for the resonance dips, shown in Fig. 3.13 and Fig. 3.14, exhibit highly confined field localization within the sensing cavity, confirming strong plasmonic coupling in the modified structure.

3.3.3.4 ***performance evaluation***

The simplified rectangular resonator exhibits a robust sensing performance with the two resonance dips showing measurable wavelength shifts across the range of n = 1.0-1.3 . The observed sensitivities are approximately 920 nm/RIU for the first mode and 1140 nm/RIU for the second mode, indicating effective interaction between the SPP fields and the sensing medium.

The reduction in the number of resonance dips leads to a clearer, more easily analyzable transmission spectrum, which may be advantageous in practical sensing applications. While the Figure of Merit (FOM) for mode-1 is slightly lower than the previous ladder-like design, but for mode-2, FOM is much higher.

Also the simplified structure demonstrates that strong sensitivity can still be achieved with a compact rectangular geometry incorporating a central ring and supporting pillars.

This design thus provides a balanced approach, combining reduced structural complexity with efficient plasmonic field confinement, paving the way for straightforward fabrication and practical implementation in refractive index sensing applications.

3.3.4 Modified design 03

In an attempt to obtain even more enhanced resonance characteristics and sensitivity, the design was further modified and explored by reducing the number of pillars and introducing six smaller n-Si rings within the central circular ring.

3.3.4.1 *structural overview*

The design has small rings embedded within the larger ring resonator and is symmetrically arranged around the central axis. The structure also retains four dielectric pillars, two on either side of the main ring, providing continued field confinement and interaction with the sensing medium, as illustrated in Fig. 3.15.

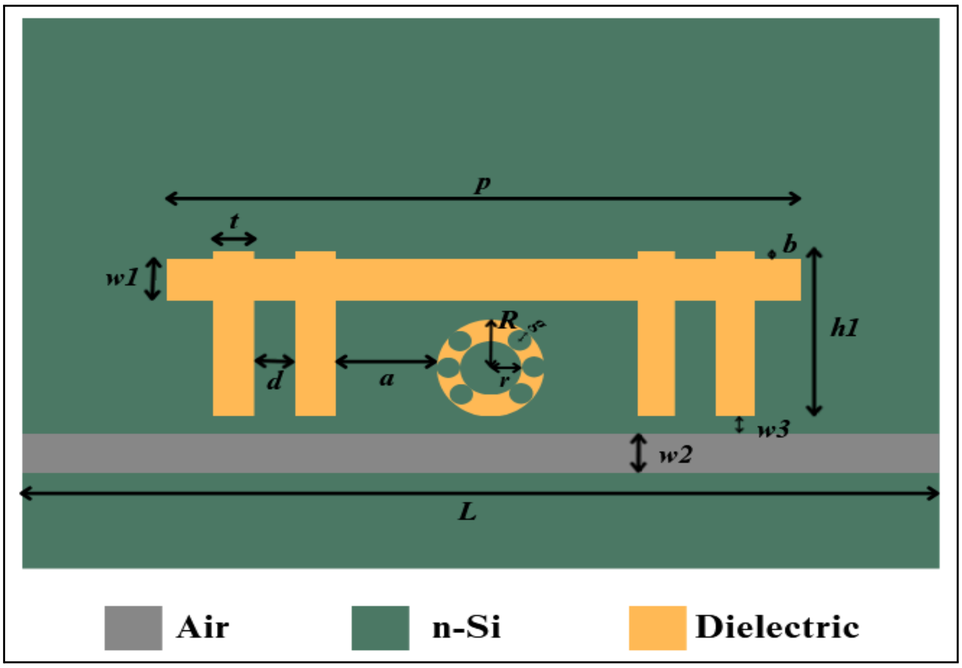

Fig. 3.15 Design of modified sensor 03

This configuration aims to investigate whether additional internal resonators can produce new plasmonic modes and sharper resonance features, thereby improving the overall sensing performance.

3.3.4.2 *design parameters*

The sensor geometry and material configuration utilised in the design is listed in Table 3.4.

Table 3.4 Sensor design parameters

Parameters	Symbol	Proposed value (nm)
Length of resonator	p	600
Width of resonator	w1	35
Width of waveguide	w2	40
Width of pillar	t	35
Gap between pillars	d	75
Height of pillar	h1	150
Distance between ring and nearby pillar	a	107.5
Inner ring radius	r	20
Outer ring radius	R	50
Gap between resonator and waveguide	w3	10
Length of waveguide	L	900
Upward length of pillar from resonator	b	7.5
Height of sensor surface	H	600
Radius of embedded n-Si ring	g	8

3.3.4.3 ***working mechanism and resonance behavior***

The inclusion of the six inner n-Si rings creates multiple coupled plasmonic cavities, which strongly influence the propagation of surface plasmon polaritons (SPPs) within the rectangular resonator. The localized plasmonic cavities formed by the small rings support additional gap plasmon resonance (GPR) modes, leading to a more complex resonance spectrum.

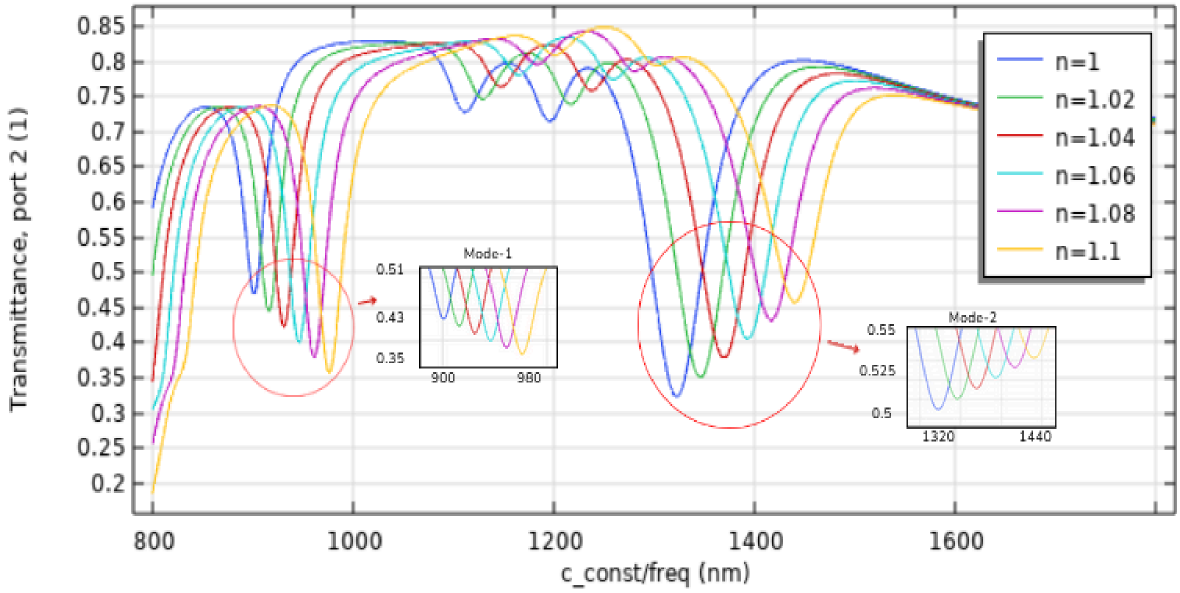

Fig. 3.16 Transmittance graph of modified design 03

As shown in Fig. 3.16, the transmittance spectra were simulated for refractive indices ranging from n = 1.0 to 1.3 with increments of 0.1. The results reveal two distinct resonance dips, Mode-1 and Mode-2, which are sharp and deep, indicating strong coupling between the SPPs and the resonator.

There are two smaller and less pronounced dips, corresponding to weaker localized modes, which can be attributed to interference between adjacent resonant paths or partial mode overlap within the multi-ring cavity.

The wavelength shifts of mode-1 and mode-2 with increasing value of n confirm the sensor's ability to find variations in the neighbouring medium. The sharper dips demonstrate enhanced field confinement due to the interplay between the main ring and the six internal rings, providing stronger light–matter interaction compared to previous designs.

Fig. 3.17 Relation of resonant wavelength with refractive index for mode-2

The resonant wavelength vs n characteristics revealed in Fig. 3.17 shows that an increase in n results in a redshift of the wavelength of resonance, that is the wavelength of resonance increases with the increase of n. This phenomenon strongly indicates enhanced light–matter interaction within the sensing region.

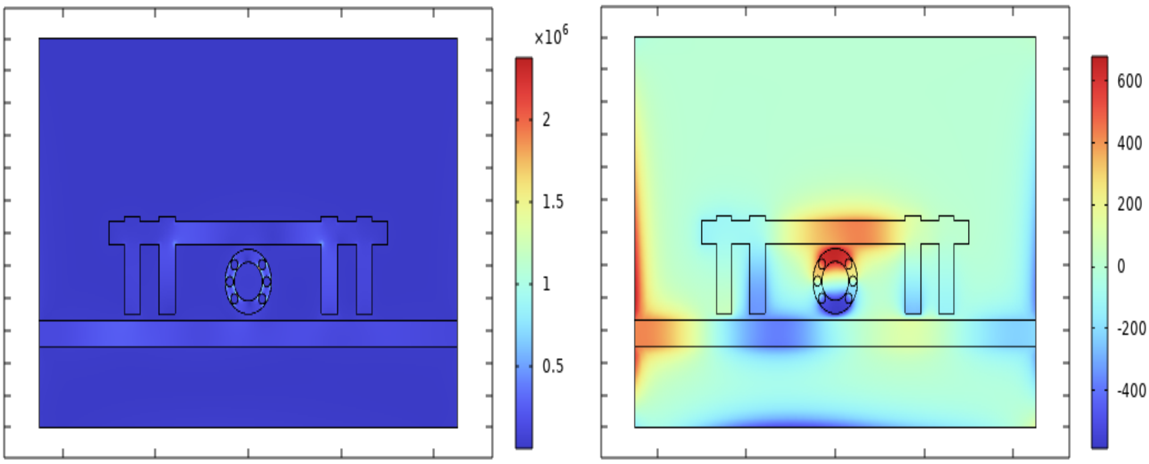

Fig. 3.18 E - field (V/m) & H - field (A/m) distribution at $\lambda = 916.3$ nm

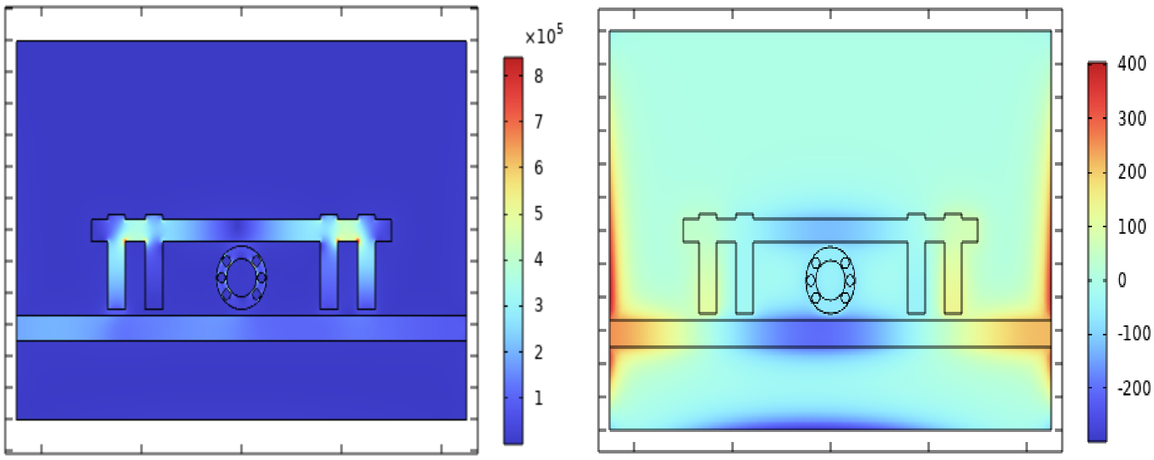

Fig. 3.19 E - field (V/m) & H - field (A/m) distribution at $\lambda = 1346.1$ nm

The electric and magnetic field distributions corresponding to the two resonance dips, shown in Fig. 3.18 and Fig. 3.19, exhibit highly confined field localization within the sensing cavity, confirming strong plasmonic coupling in the modified structure.

3.3.4.4 *performance evaluation*

The final structure exhibits significant improvement in sensitivity and spectral resolution. The sharp dips show large resonance shifts, yielding sensitivities of approximately 796.5 nm/RIU and 1165 nm/RIU. The deep and shallow dips allow for both high-resolution detection and multi-range sensing capabilities.

The reduction in pillar complexity, along with the addition of inner rings, results in a compact yet highly responsive plasmonic sensor. The enhanced spectral behavior confirms that the design modifications effectively increase light confinement and improve tunability of resonance modes.

CHAPTER 4
RESULTS AND DISCUSSIONS

4.1 Plasmonic resonator designs and performances

Progressive modifications in the resonator geometry led to noticeable variations in plasmonic response and sensing efficiency. Different configurations exhibited distinct resonance behaviors depending on their structural complexity and coupling mechanisms. Table 4.1 presents the comparative performance of the designed plasmonic resonators, emphasizing how geometric refinement influenced sensitivity and field confinement.

Table 4.1 Comparison of plasmonic resonator designs

Design	Sensitivity (nm/RIU)	Key Observations
Initial grating based structure	120.57	Basic plasmonic coupling, single dip with moderate confinement
Ladder-like resonator with ring and four pillars	771, 990 & 1180	Multiple dips with strong hybridization, improved field confinement, moderate FOM
Simplified rectangular resonator with ring and four pillars	920 & 1140	Reduced complexity; fewer dips, clear and sharp spectral features, slightly lower FOM
Rectangular resonator with six inner n-Si rings	796.5 & 1165	Two sharp dips with strong field confinement, two smaller dips, optimized sensitivity, multi-mode

4.2 Finalised design

Following the systematic study, the Modified design 03 with one main rectangular resonator, four supporting dielectric pillars and six embedded n-Si rings within the central ring, as shown in Fig. 4.1 was selected as the final design .

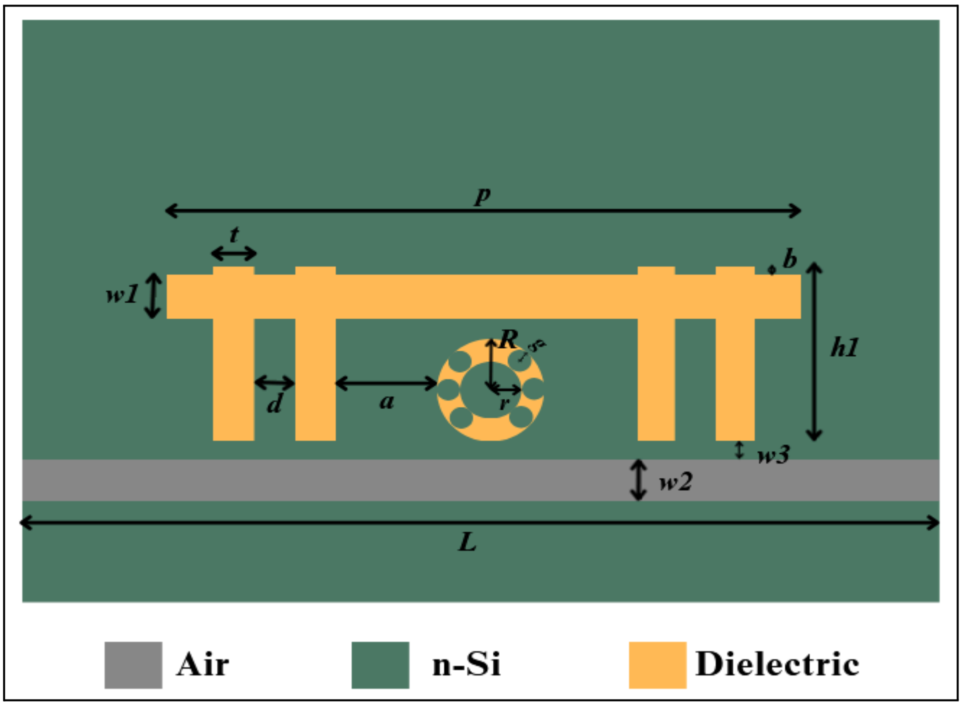

Fig. 4.1 Design of finally selected sensor

This configuration provides an optimal balance between structural simplicity, strong field confinement and multi-dip resonance performance, making it the ideal candidate for practical refractive index sensing applications.

4.3 Fine-tuning of finalised design parameters

Optimization of the sensor geometry is essential to enhance plasmonic coupling efficiency and overall sensing performance. To achieve the optimal configuration, key structural parameters were systematically varied.

Their effects on the transmittance spectra were analyzed through FEM-based numerical simulations to identify the configuration that provides the best values of sensitivity. The identification of structure with best FOM was also aimed simultaneously.

4.3.1 Effect of gap between pillars (d)

The influence of the gap between the pillars was investigated by varying d from 55 nm to 95 nm in increments of value of 10 nm.

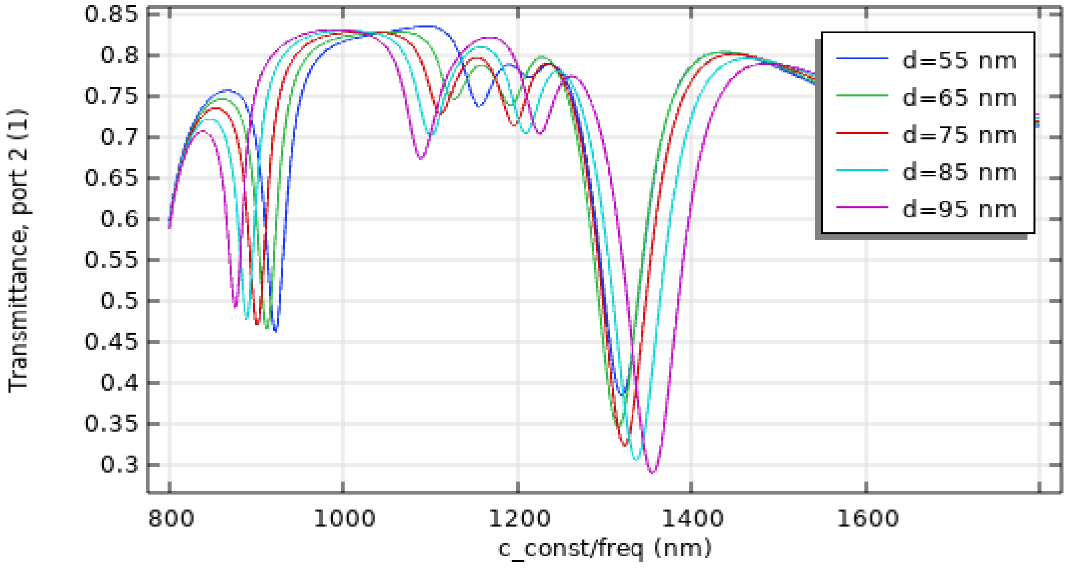

Fig. 4.2 Transmittance graph of finalised design for varying d

As illustrated in Fig. 4.2, increasing the gap results in a clear redshift of the resonance wavelengths, that is the resonant wavelength increases with increase of gap between the pillars. This phenomenon is more pronounced in Fig. 4.3. The result also shows a reduction in the resonance depth, which can be more clearly identified in Fig. 4.2.

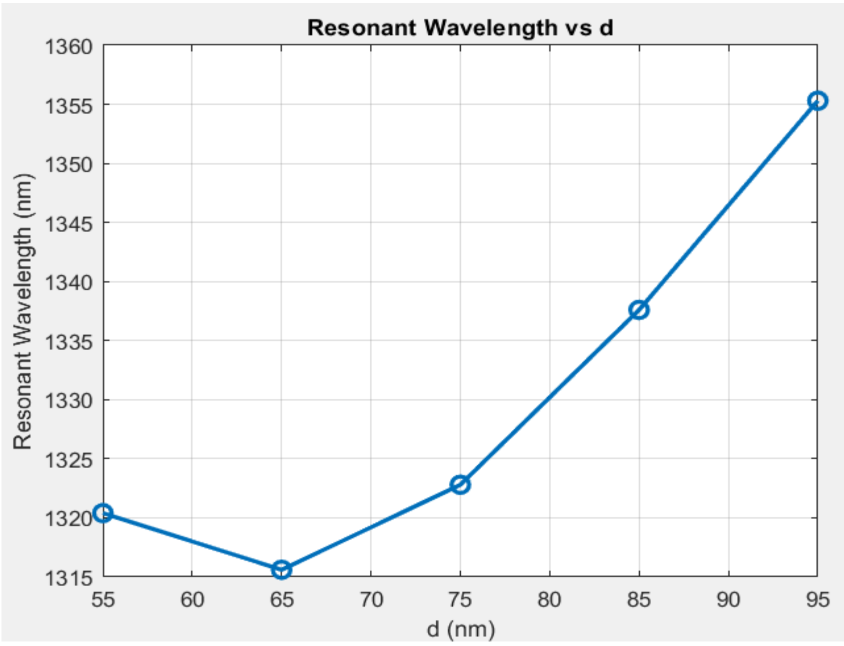

Fig. 4.3 Relation of resonant wavelength with varying d

This behavior can be attributed to the weaker interaction as the separation increases. A smaller gap enhances mode overlap, thereby improving the confinement and strength of surface plasmon polaritons (SPPs).

Based on the analysis, an optimal gap of d = 85 nm was selected, as it ensures strong mode coupling and stable spectral features without excessive loss.

4.3.2 Effect of pillar height (h_1)

To study the impact of vertical confinement on resonance behavior, between 120 nm and 160 nm, the pillar height (h_1) was changed with an interval of 10 nm.

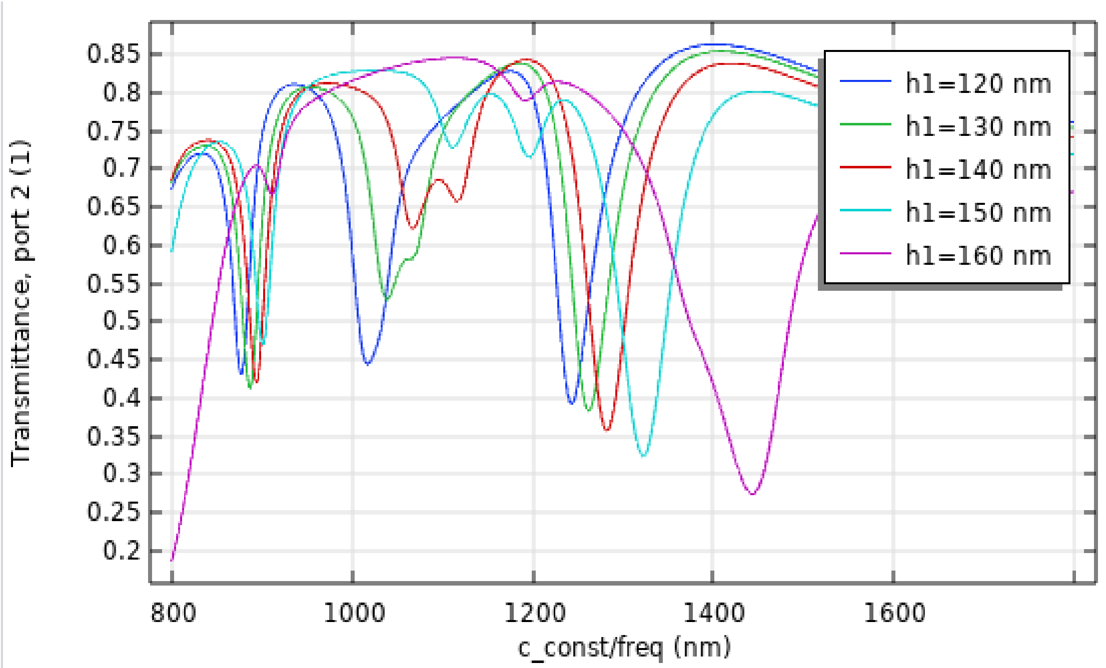

Fig. 4.4 Transmittance graph of finalised design for varying h_1

The corresponding transmittance spectra, shown in Fig. 4.4, reveal that the resonance dips shift with changes in height. It is also evident that both the depth and sharpness of the dips vary significantly with the change of height.

The change of resonant wavelength with change of height is plotted in Fig. 4.5. The figure shows, for the designed structure, as the height increases from h_1 = 120 nm to h_1 = 160 nm, the resonant wavelength slowly increases at first. Later on, there is a large increase in the wavelength. This behaviour of redshift of wavelength can be attributed to stronger field confinement at increased heights.

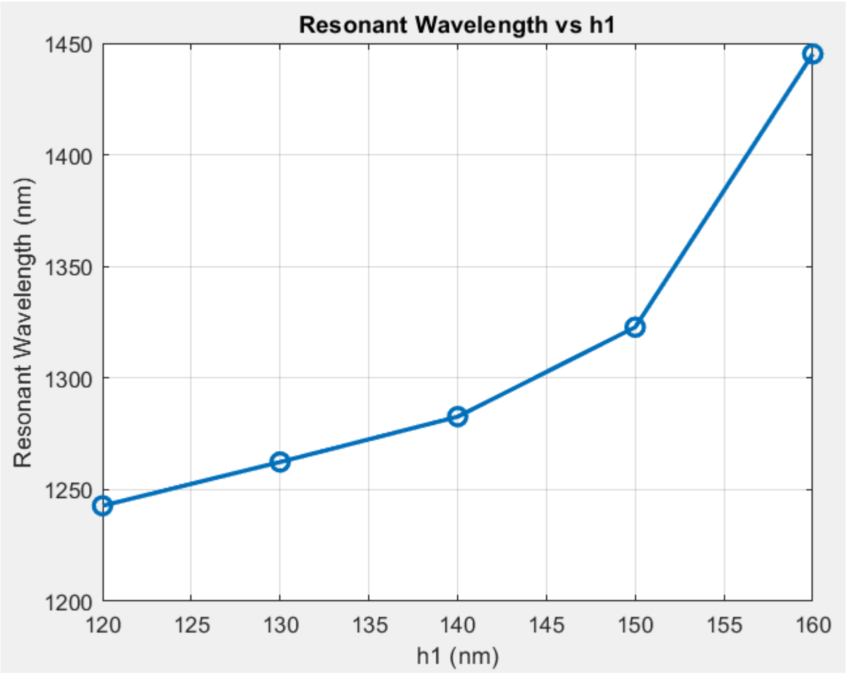

Fig. 4.5 Relation of resonant wavelength with varying h1

Taller pillars promote stronger light–matter interaction due to increased confinement but can introduce additional propagation losses at excessive heights. From the simulation outcomes, h_1 = 150 nm was identified as the optimal, which gave a balance between resonance confinement, transmission intensity and FOM.

4.3.3 Effect of resonator width (w_1)

The resonator width (w_1), in 5 nm steps, was changed from 25 nm to 45 nm to evaluate its impact on plasmonic coupling efficiency and resonance characteristics.

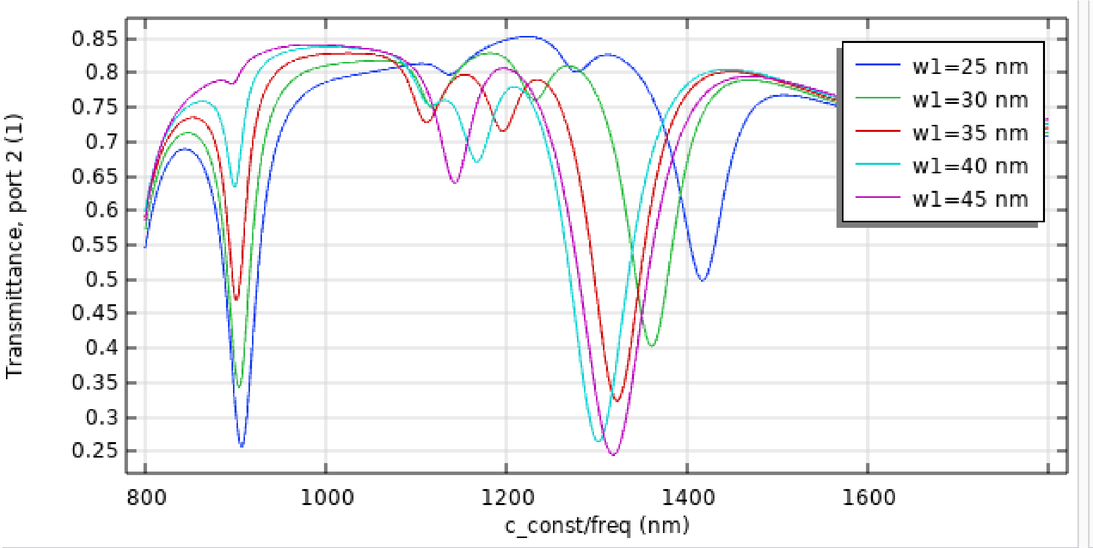

Fig. 4.6 Transmittance graph of finalised design for varying w_1

The transmittance spectra, shown in Fig. 4.6, demonstrate that increasing w_1 leads to a redshift of the resonance dips and alters their depth. The change of resonant wavelength with change of w_1 is shown in Fig. 4.7.

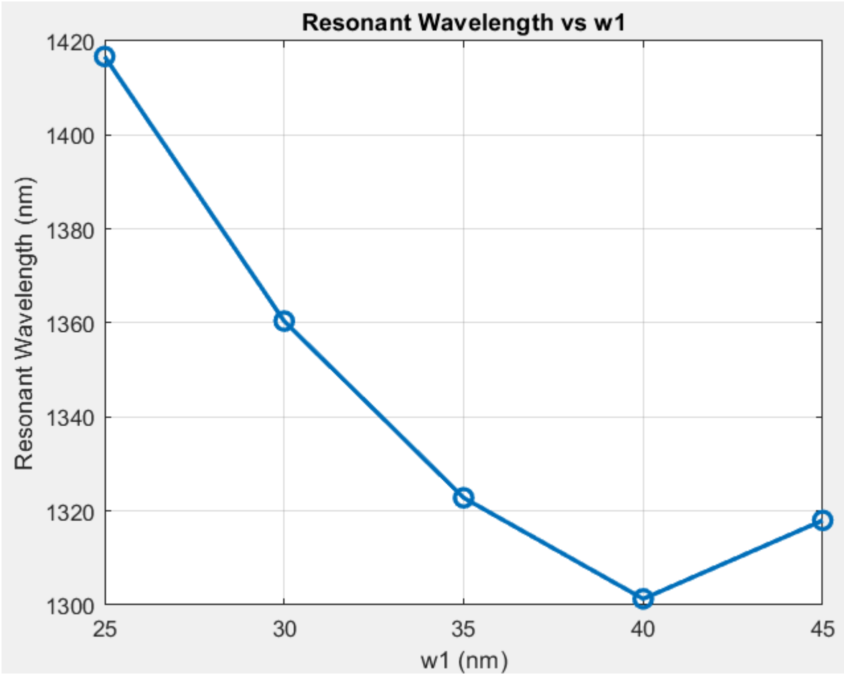

Fig. 4.7 Relation of resonant wavelength with varying w_1

Narrower resonators (w_1 = 40 nm) exhibit deeper and sharper resonances, indicating enhanced confinement and stronger coupling. But, excessive narrowing increases losses and reduces propagation stability.

Wider resonators (w_1 = 40 - 45 nm) exhibit shallower resonances, indicating weaker field interaction, making these widths not so much of an ideal choice, for selection for the optimal design.

The optimal configuration is obtained for w_1 = 35 nm, hence this is chosen for the optimal design, yielding well-defined resonances, balanced coupling and high spectral stability.

4.3.4 Effect of outer radius of ring resonator (R)

The impact of varying the ring resonator outer radius (R) was studied for a range of 50 nm to 56 nm in 2 nm intervals.

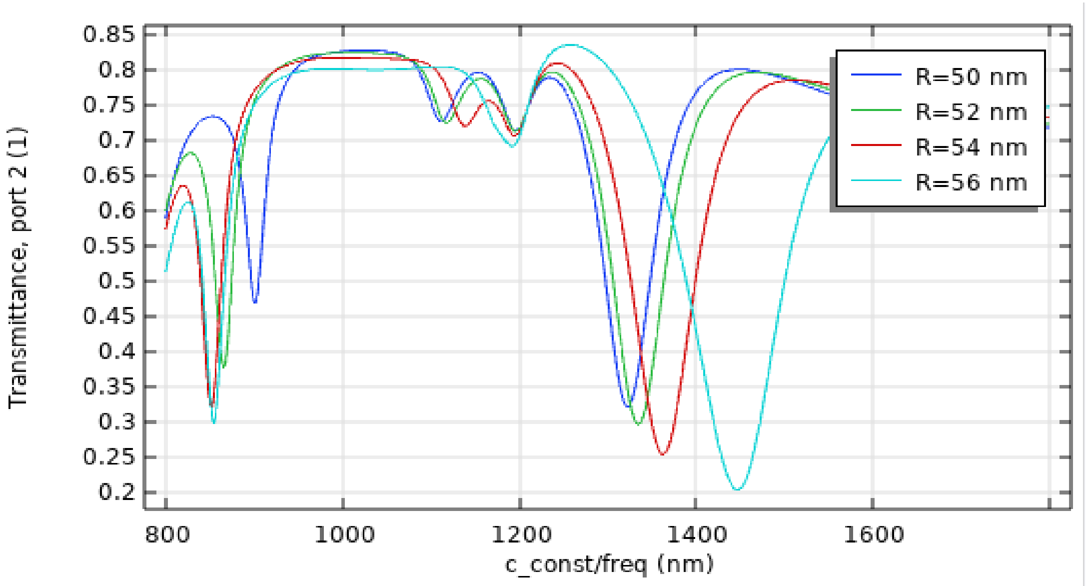

Fig. 4.8 Transmittance graph of finalised design for varying R

As shown in Fig. 4.8, increasing the radius produces a redshift in the resonance wavelength, signifying enhanced light–matter interaction due to stronger field confinement. This feature is also observed through Fig. 4.9.

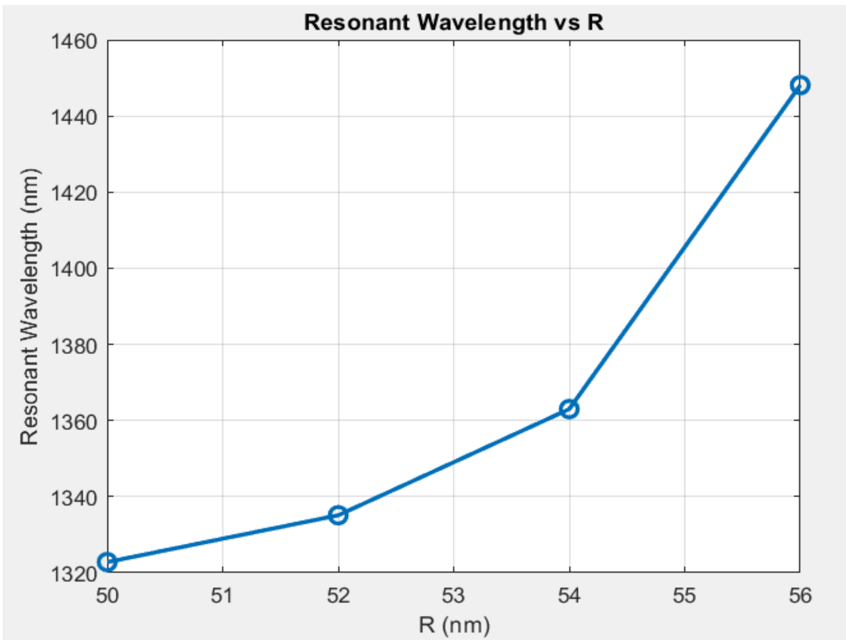

Fig. 4.9 Relation of resonant wavelength with varying R

However, larger radii broaden the resonance dips, slightly reducing the figure of merit (FOM). Among the tested values, R = 54 nm offers the best compromise between sensitivity and dip sharpness and is therefore selected as the optimal radius for achieving balanced sensor performance.

4.3.5 Effect of inner radius of ring resonator (r)

The transmittance spectra for different inner radii (r = 10 - 30 nm) are shown in Fig. 4.10.

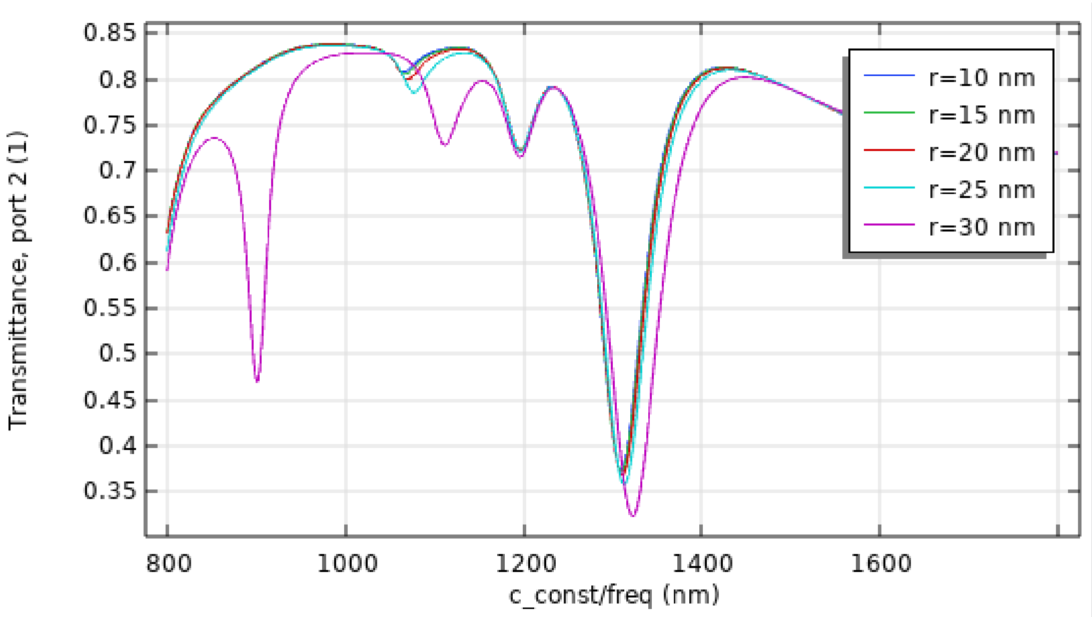

Fig. 4.10 Transmittance graph of finalised design for varying r

A slight redshift is observed with the increase in radius. There is also a presence of a minor reduction in transmittance at certain dips as well. The redshift of resonance is illustrated in Fig. 4.11.

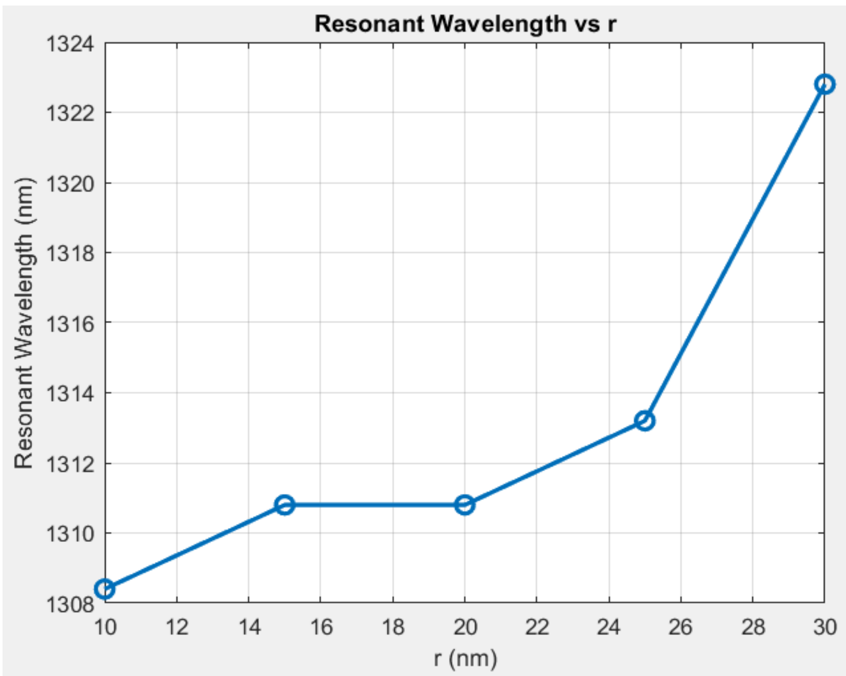

Fig. 4.11 Relation of resonant wavelength with varying r

Larger radii enhance light confinement and sensitivity by strengthening the coupling between the resonator and the guided modes. Nonetheless, an excessive increase can degrade resonance sharpness and reduce FOM.

The optimal configuration is determined as r = 25 nm, hence this is chosen for the optimal design, offering a strong balance between sensitivity, confinement and spectral quality.

4.3.6 Effect of n-Si ring radius (g)

The transmittance for varying n-Si ring radii (g = 4 - 8 nm) is presented in Fig. 4.12.

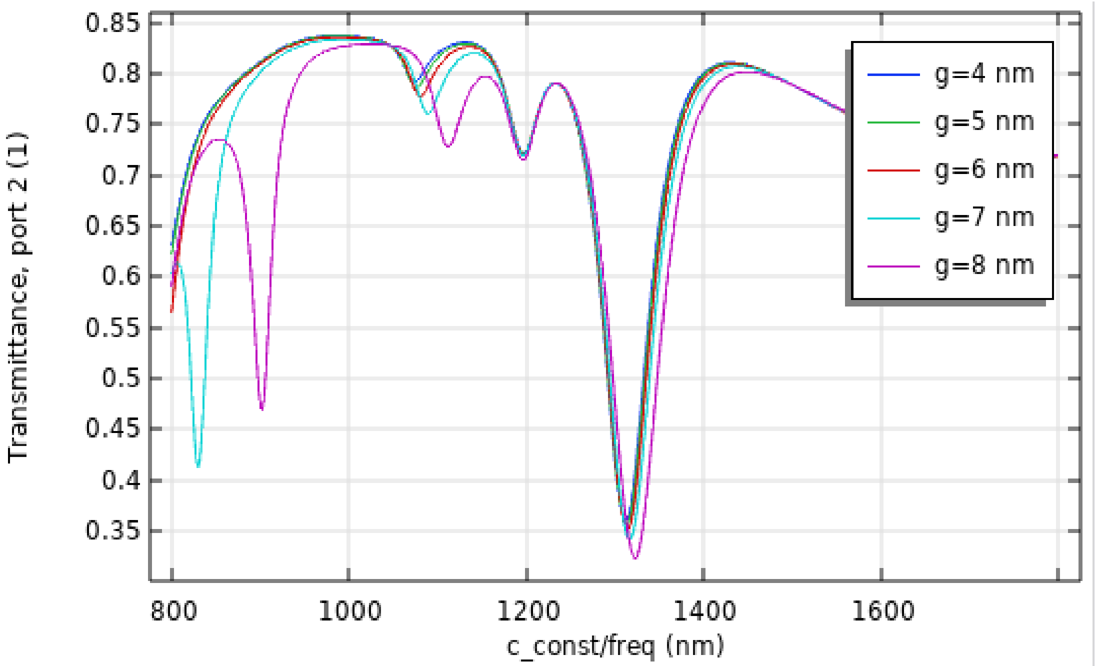

Fig. 4.12 Transmittance graph of finalised design for varying g

As the radius increases, the resonance dips experience a slight red shift, that is the resonant wavelength increases with increase of the ring radius. The resonance dips also exhibit an increased depth, indicating stronger coupling between the resonator and waveguide.

The change of resonant wavelength with varying g can be seen from Fig. 4.13, which demonstrates the connection between wavelength of resonance and the radius of the n-Si ring.

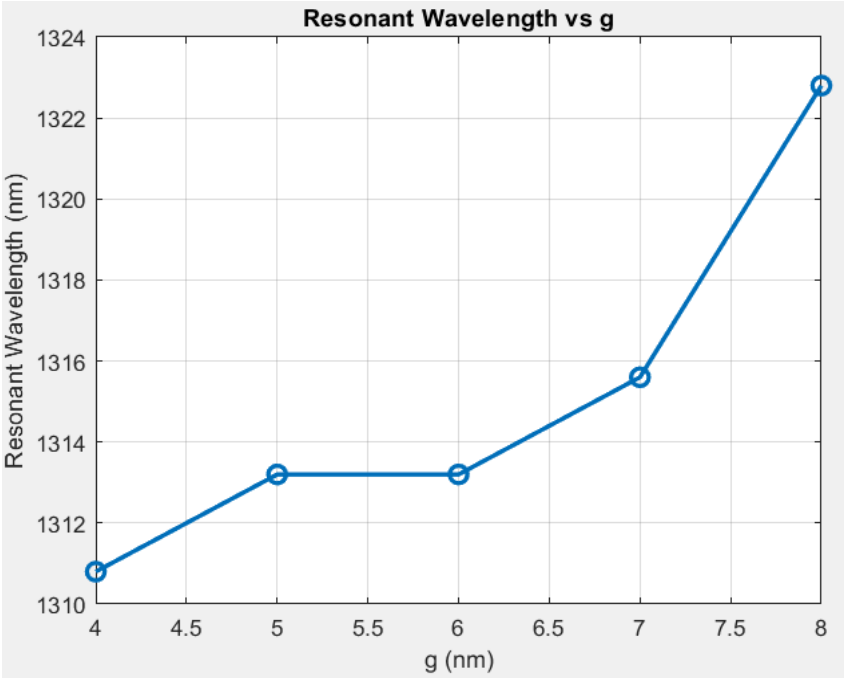

Fig. 4.13 Relation of resonant wavelength with varying g

When *g* is too small, over-coupling occurs, which deteriorates transmittance and resonance quality. The best overall performance is obtained for g = 8 nm, which maintains strong resonance with moderate radius, ensuring balanced sensitivity and FOM.

4.3.7 Effect of pillar width (t)

The effect of pillar width (t) on the sensor's optical response was evaluated by varying it in a range 30 - 50 nm in increments of 5 nm.

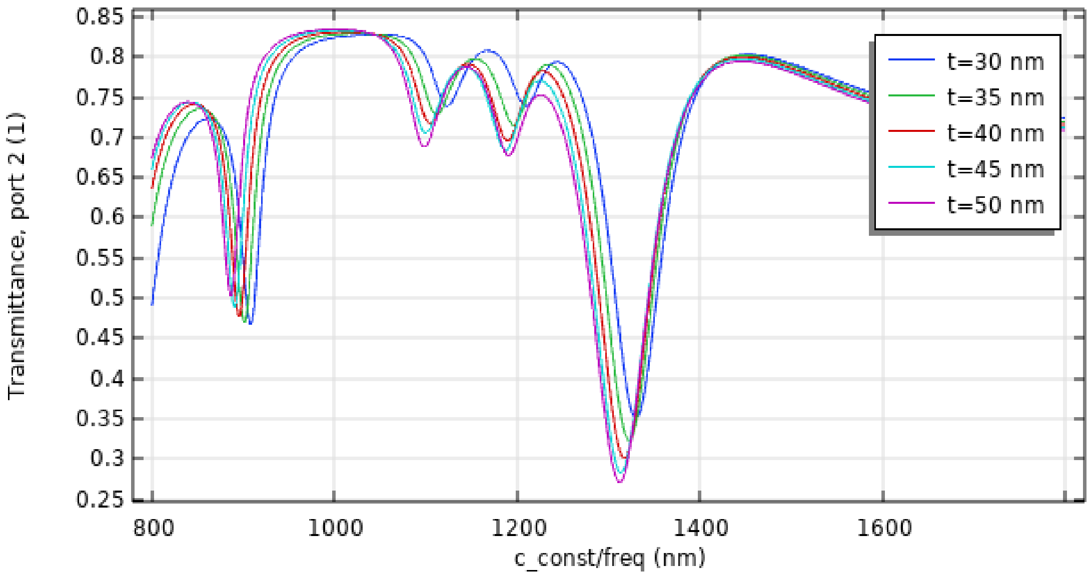

Fig. 4.14 Transmittance graph of finalised design for varying t

As illustrated in Fig. 4.14, increasing *t* leads to a blueshift of the resonance peaks and a moderate reduction in transmittance intensity at certain wavelengths. The change of resonant wavelength with varying t is plotted in Fig. 4.15, where it is clearly noticeable that as the value of t increases, the resonant wavelength decreases gradually.

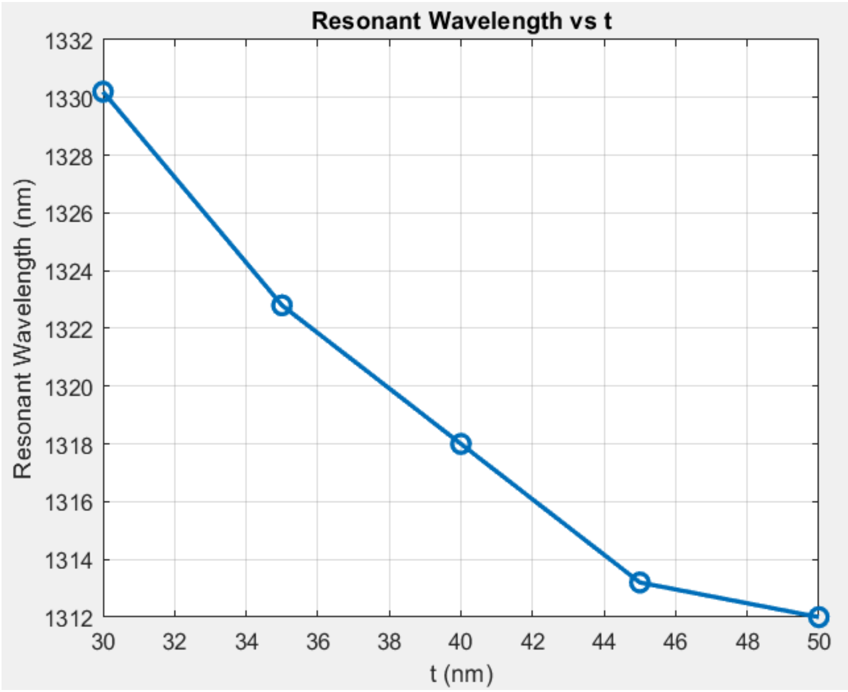

Fig. 4.15 Relation of resonant wavelength with varying t

This trend arises from enhanced plasmonic confinement and increased absorption losses, which broaden the resonance dips. Beyond t = 45 nm, the spectral shift becomes less significant.

The optimal value, t = 45 nm, provides a suitable balance between sharp resonance features and strong surface plasmon excitation without excessive optical loss, hence this is selected for the optimal design.

4.3.8 Effect of resonator length (p)

The impact of the resonator length (p) on resonance behavior was studied for lengths ranging from 500 nm to 700 nm, with 50 nm increments and simulation was run on the finalised design.

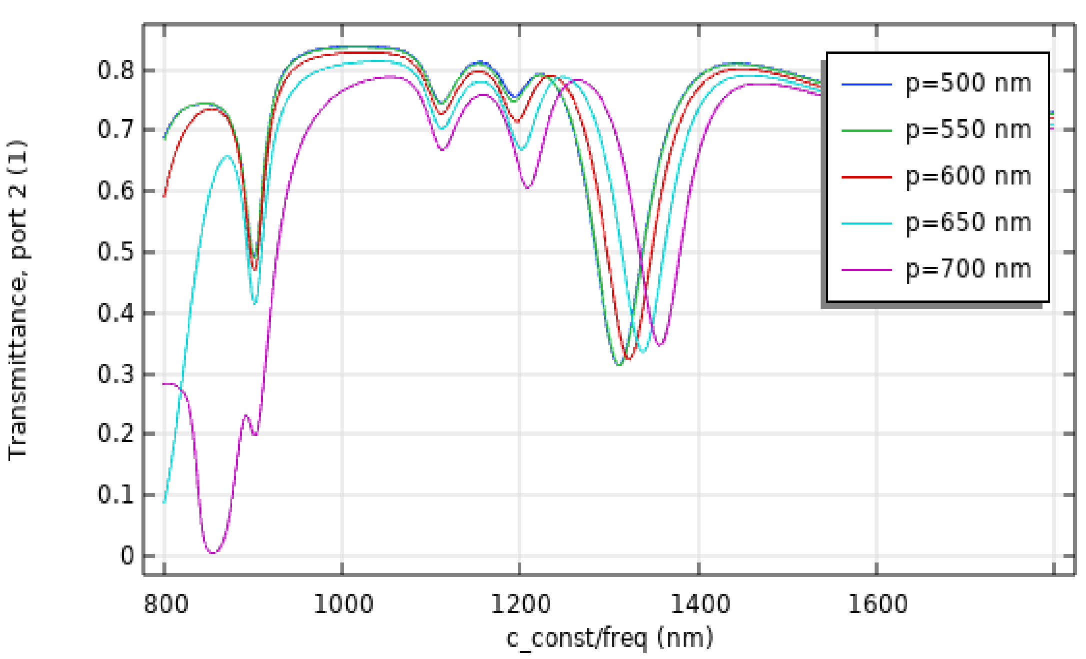

Fig. 4.16 Transmittance graph of finalised design for varying p

As illustrated in Fig. 4.16, increasing p causes a pronounced redshift in resonance wavelengths, confirming that resonator length directly affects coupling between the incident light and plasmon modes. The change of resonant wavelength with varying p is observable from Fig. 4.17.

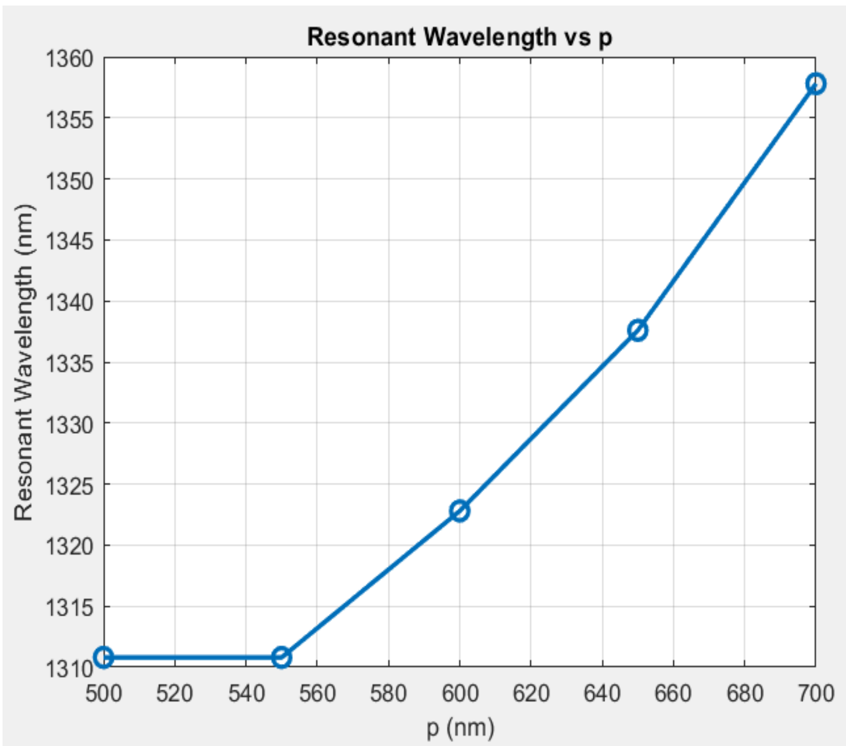

Fig. 4.17 Relation of resonant wavelength with varying p

Shorter lengths (p = 500 - 550 nm) produce resonance dips at shorter wavelengths with higher transmittance, whereas longer lengths (p = 650–700 nm) shift the dips toward longer wavelengths and reduce transmission due to weaker confinement.

The optimal configuration, p = 600 nm, yields well-defined resonance features with strong transmittance and stable spectral behavior.

4.3.9 Effect of coupling distance between ring and waveguide (w_3)

The coupling distance (w_3) is a critical parameter controlling the coupling strength and resonance behavior of the sensor. As shown in Fig. 4.18, w_3 was varied from 5 nm to 25 nm to evaluate its influence on transmittance characteristics for the design that was finalised.

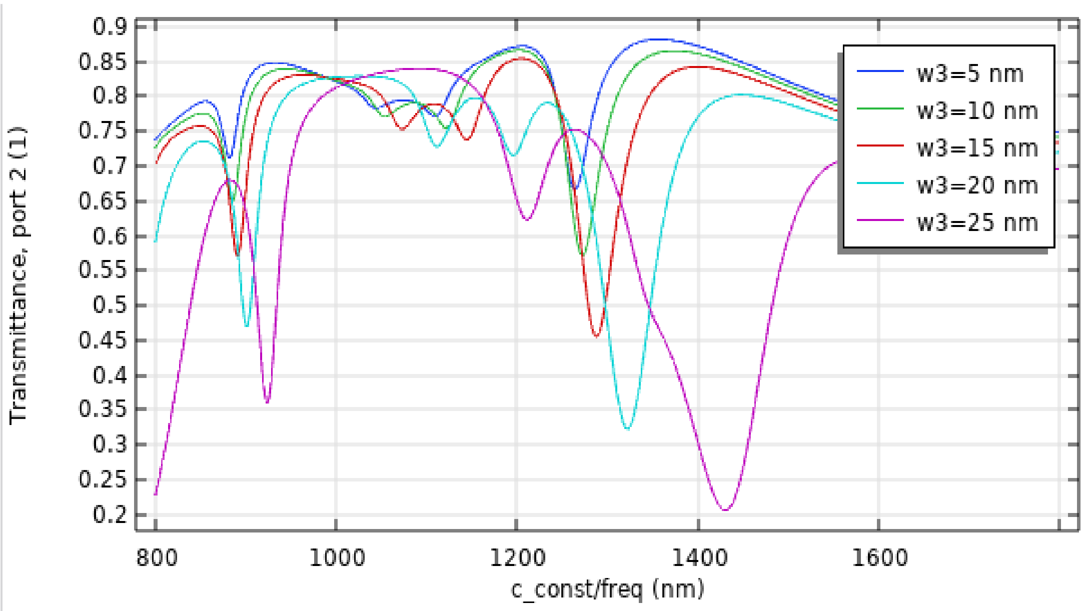

Fig. 4.18 Transmittance graph of finalised design for varying w_3

At smaller distances (w_3 = 5 - 10 nm), sharp and well-defined resonance dips are observed, indicating strong coupling and efficient plasmon excitation.

Increasing w_3 beyond 15 nm results in a redshift and broadening of resonance peaks with reduced transmittance, due to weaker confinement and higher propagation losses. For w_3 = 25 nm, the dips become considerably weaker, indicating poor performance.

The change of resonant wavelength with varying p was also plotted in Fig. 4.19 for better observation of the effect.

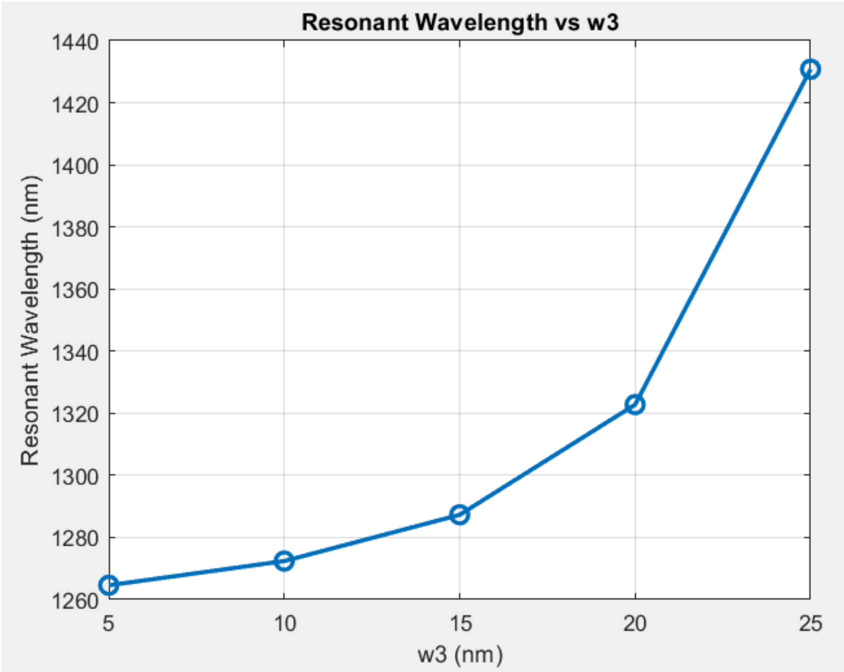

Fig. 4.19 Relation of resonant wavelength with varying w_3

Based on the results, w_3 = 20 nm is selected as the optimal, providing balanced coupling strength, transmittance intensity and overall sensor stability.

4.4 Optimal design

The finalized design parameters were determined to achieve optimal sensor performance after an elaborate optimization process. The parameter's optimized values are summarized in Table 4.2, representing the most effective combination of geometrical dimensions that balance sensitivity, resonance sharpness and overall spectral stability.

Table 4.2 Optimal sensor design parameters

Parameters	Symbol	Proposed value (nm)
Resonator length	p	600
Width of resonator	w1	40
Width of waveguide	w2	40
Width of pillar	t	45

Gap between pillars	d	85
Height of pillar	h1	150
Distance between ring and nearby pillar	a	107.5
Inner ring radius	r	25
Outer ring radius	R	54
Resonator and waveguide gap	w3	20
Waveguide length	L	900
Upward length of pillar from resonator	b	7.5
Height of sensor surface	H	600
Radius of embedded n-Si ring	g	7

The transmittance spectra corresponding to the optimized configuration are presented in Fig. 4.20, plotted for varying values of the n.

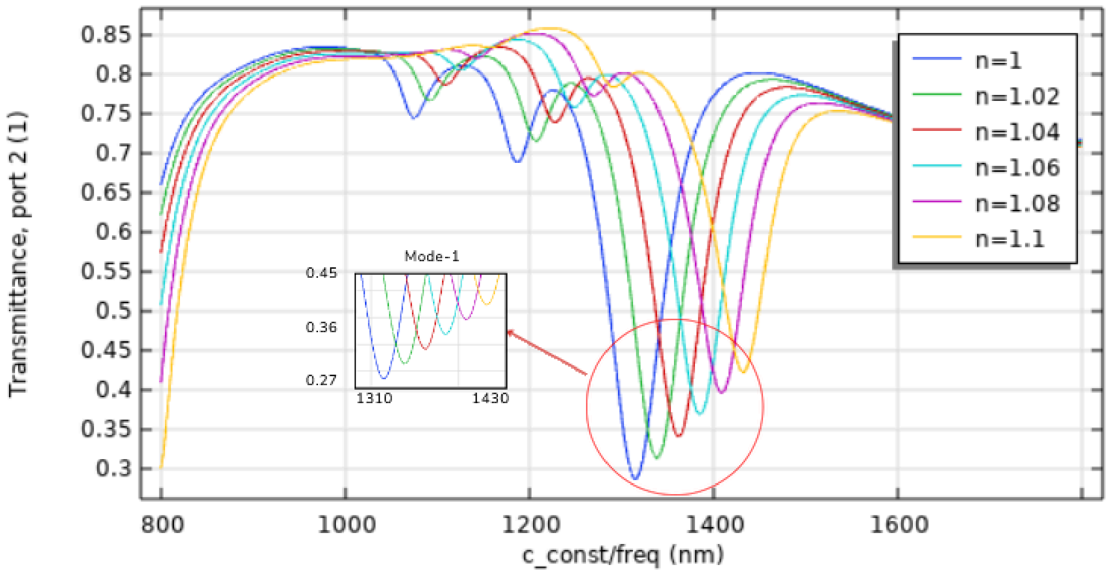

Fig. 4.20 Transmittance graph of optimal design

The results clearly demonstrate well-defined and distinct resonance dips that redshift progressively with increasing n, confirming refractive index (n) sensitivity that is very high and strong light–matter interaction.

From the simulation analysis, the proposed structure obtains a sensitivity of 1270 nm/RIU that is maximum and a corresponding FOM of 22.3, indicating superior detection performance compared to conventional plasmonic designs.

The optimized parameters together form a configuration that provides strong confinement of surface plasmon polaritons (SPPs) with minimal propagation loss.

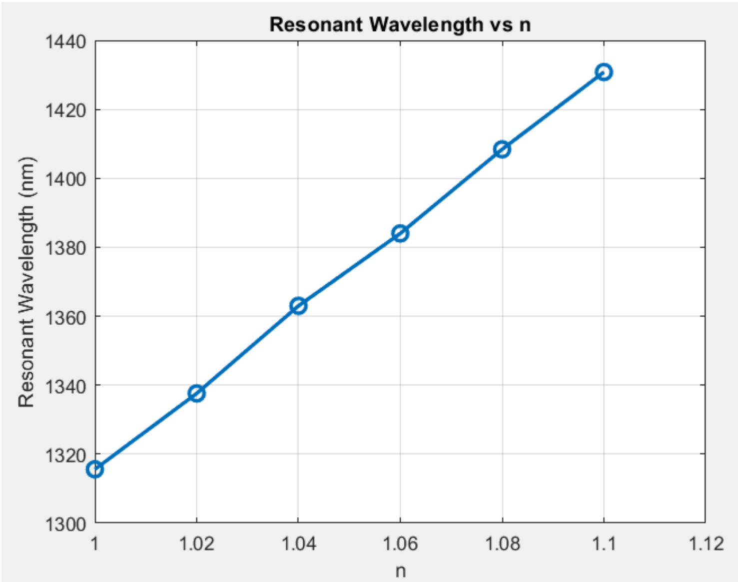

Fig. 4.21 Relation of resonant wavelength with refractive index (n) for mode-2

The resonant wavelength vs refractive index (n) characteristics of Fig. 4.21 reveals a redshift for the increase of n, meaning resonant wavelength increases, indicating enhanced light–matter interaction within the sensing region.

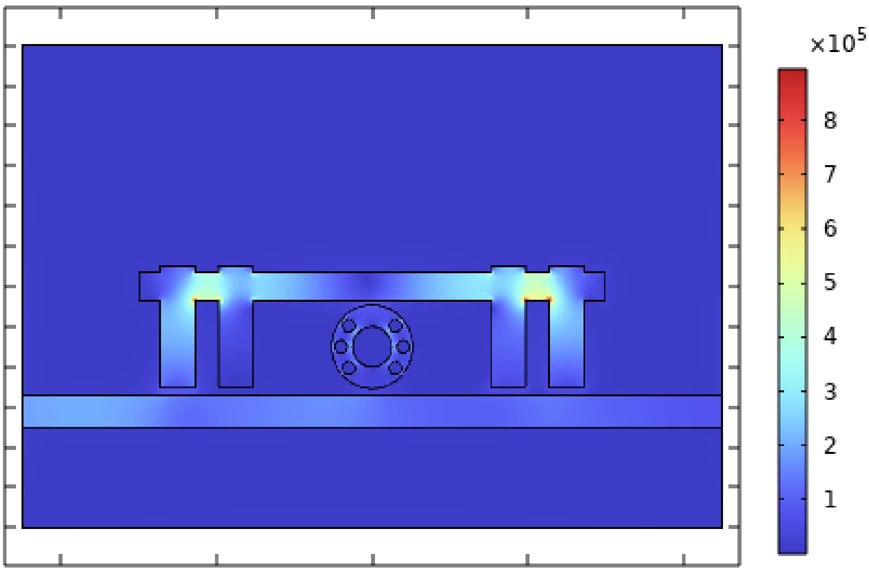

Fig. 4.22 Electric field (V/m) distribution at $\lambda = 1337.6$ nm

Furthermore, Fig. 4.22 illustrates the electric field distributions of the optimized structure for the main resonant mode, showing highly localized and intense field concentrations around the metal–dielectric interface.

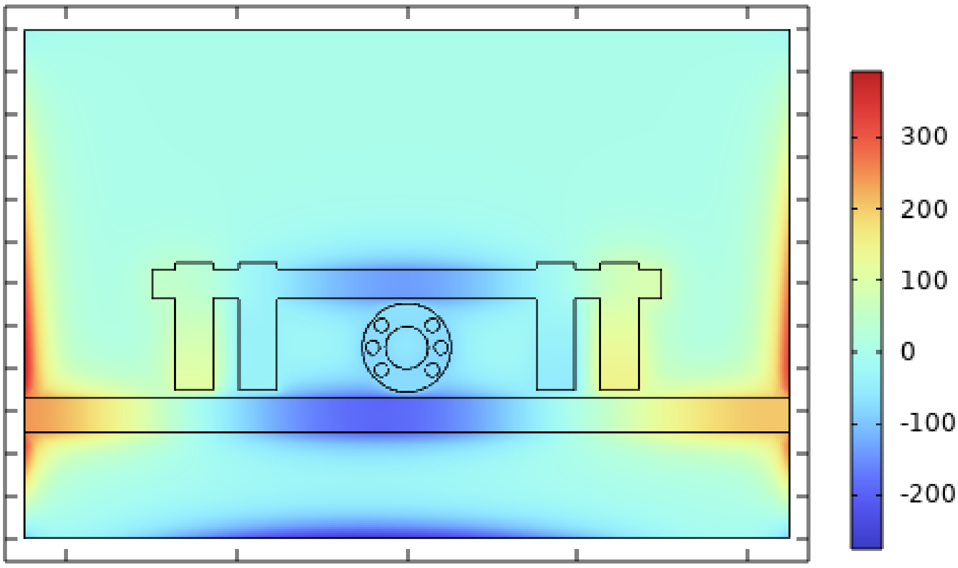

Fig. 4.23 Magnetic field (A/m) distribution at $\lambda = 1337.6$ nm

The magnetic field distribution is presented in Fig. 4.23, further confirming efficient plasmonic coupling and robust field enhancement within the sensing region.

The optimized sensor design demonstrates excellent field confinement, high sensitivity and stable resonance characteristics, making it a strong candidate for high-performance refractive index sensing and other nanoscale optical detection applications.

4.5 Applicability of the optimal sensor

In this section, the practical applications of a silicon-based plasmonic refractive index (RI) sensor that has been proposed for the purpose of detecting biological analytes was explored. The sensor operates by monitoring the reflectance spectrum and identifying the resonant wavelength corresponding to a specific refractive index.

Different biological components, such as tissues, blood, brain matter and various cell types, possess characteristic refractive indices. By accurately detecting these indices, the sensor can effectively find and distinguish between these biological components, which reinforces the goal of the study.

This approach highlights the potential of the Si plasmonic RI sensor for non-invasive and label-free detection in biomedical diagnostics and health monitoring.

For bio-sensing applications, the resonant mode with highest sensitivity was selected. This mode exhibits a sufficiently strong evanescent field, allowing the sensor to detect small changes in n with accuracy that is very high [46].

4.5.1 Biological detection of "Blood components"

Blood consists of various components, each having a distinct refractive index, as shown in Table 4.3.

Table 4.3 Refractive index of different "Blood components"

Blood component	Refractive index [50]	Resonant wavelength (nm)
Water	1.33	919.82
Plasma	1.35	930.54
White blood cells	1.36	935.38
Hemoglobin	1.38	946.47
Red blood cells	1.4	956.55

These differences can be exploited to analyze and identify specific blood components using the proposed Si plasmonic RI sensor. For instance, red blood cells exhibit a higher n than white blood cells, allowing their detection through shifts in the resonant wavelength.

The data in Table 4.3 can be employed for monitoring conditions such as anemia, infections and other blood-related disorders.

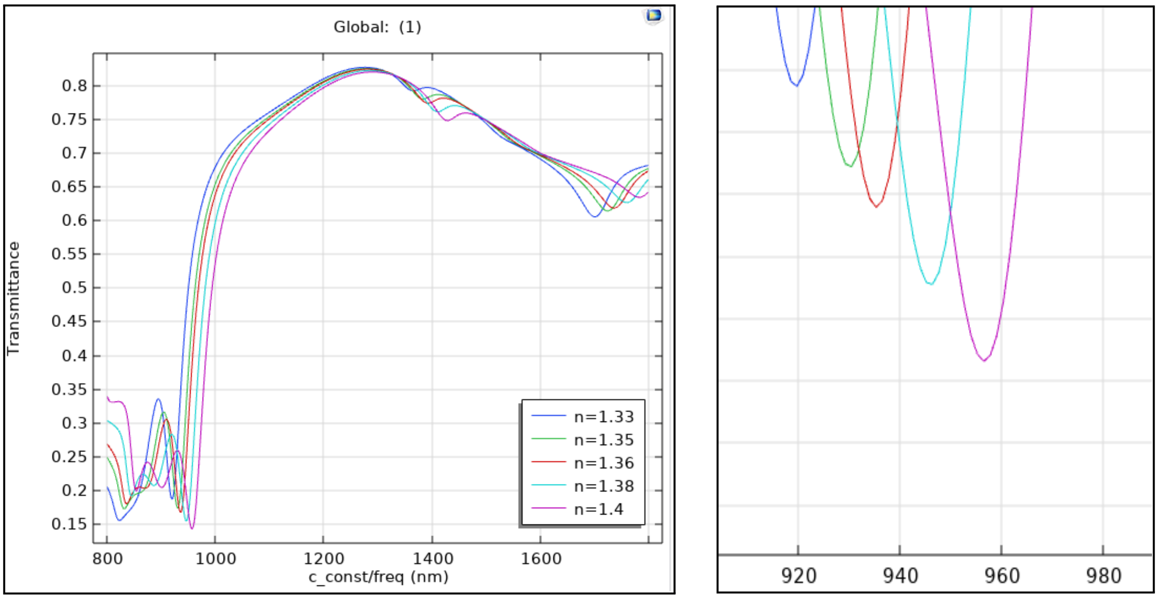

Fig. 4.24 Transmittance graph for different "Blood components"

Fig. 4.24 illustrates the transmittance versus wavelength profile for different blood components, highlighting the resonant wavelengths corresponding to their respective refractive indices.

4.5.2 Biological detection of "Brain components"

Brain components, such as gray matter, white matter, cerebrospinal fluid and other neural tissues, possess unique refractive indices, which result in distinct resonant wavelengths when analyzed with the Si plasmonic RI sensor.

Table 4.4 Refractive index of different "Brain components"

Brain component	Refractive index [51]	Resonant wavelength (nm)
Grey matter	1.395	954.01
Medulla	1.438	976.04
Cortex	1.444	980.03
White matter	1.467	992.21
Cerebellum	1.470	993.58

The differences in refractive index are captured in Fig. 4.25, showing the reflectance versus wavelength profiles, while Table 4.4 provides a detailed summary of the corresponding data.

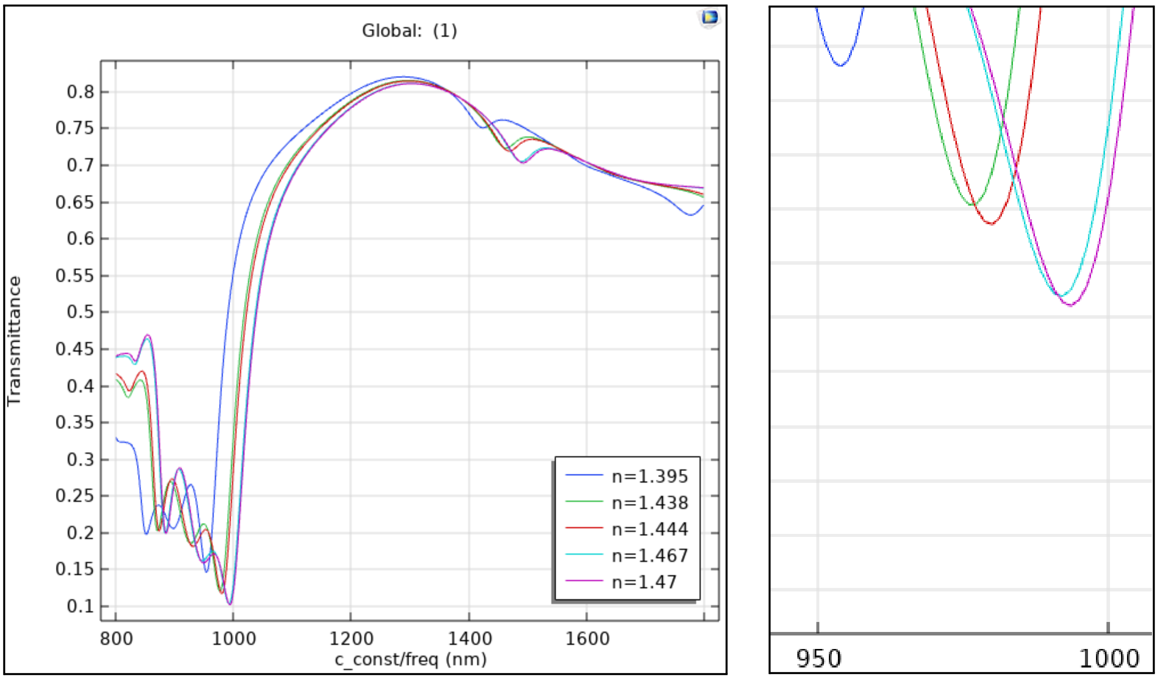

Fig. 4.25 Transmittance graph for different "Brain components"

By identifying the resonant wavelength associated with each component, the sensor can non-invasively detect and differentiate between various brain tissues. This capability is particularly useful for biomedical applications such as monitoring neural health, detecting abnormalities or assisting in neurological research.

The high sensitivity of the sensor allows even small variations in refractive index to be observed, enabling precise mapping of brain tissue properties and potentially aiding in early diagnosis of neurological disorders.

4.5.3 Biological detection of "Intracellular components"

Detection of intracellular components using the Si plasmonic RI sensor requires proper sample preparation. Homogenization is performed to release intracellular contents, while filtering removes large debris and cell membranes, ensuring that only the relevant components enter the sensor [18].

Upon optical excitation, the sensor detects shifts in the wavelength of resonance corresponding to the n of the intracellular material. These shifts allow precise determination of the refractive index, as summarized in Table 4.5.

Table 4.5 Refractive index of different "Intracellular components"

Intracellular component	Refractive index [52]	Resonant wavelength (nm)
Water	1.33	919.82
Protein	1.4	956.55
Lipid	1.42	966.85
DNA	1.44	977.37
Bi-lipid membrane	1.46	988.12

The reflectance versus wavelength profile is illustrated in Fig. 4.26.

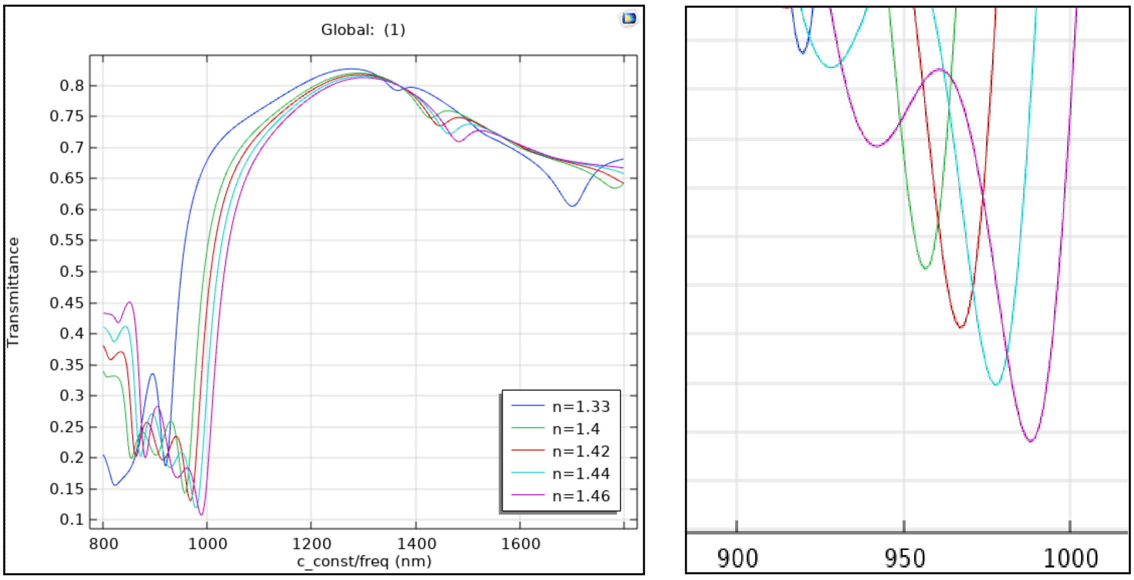

Fig. 4.26 Transmittance graph for different "Intracellular components"

By analyzing the resonant shifts, the sensor can identify and differentiate various intracellular components, providing valuable insights for cellular biology studies, disease diagnostics and monitoring of cellular processes. The sensitivity of the sensor is very high which aids to detect even subtle variations in refractive index, making it suitable for applications requiring fine discrimination of intracellular materials.

4.5.4 Biological detection of "Various tissues"

Different tissue types exhibit distinct refractive indices due to variations in their chemical composition, cellular density and molecular structure. These differences lead to characteristic shifts in the resonant wavelength when analyzed with the Si plasmonic RI sensor.

Table 4.6 Refractive index of "Various tissues"

Tissue types	Refractive index [27]	Resonant wavelength (nm)
Pancreas	1.3517	930.54
Muscle	1.3713	941.51
Liver	1.3791	945.22
Dermis	1.3818	946.47

The reflectance versus wavelength spectra shown in Fig. 4.27 illustrates how the resonant wavelength varies for each tissue type, while Table 4.6 provides the corresponding refractive index values.

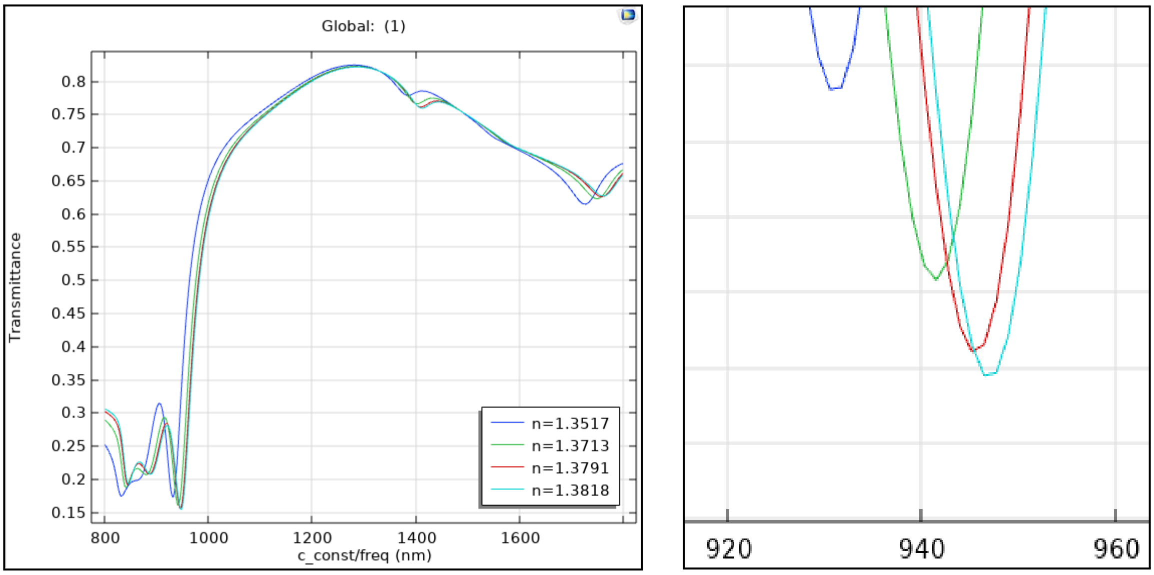

Fig. 4.27 Transmittance graph for "Various tissues"

By equating the measured n of an under-test tissue sample with these reference values, the sensor can accurately identify the tissue type. To ensure reliable and precise measurements, proper tissue preparation and standardized measurement protocols are essential [53]. This approach highlights the potential of the sensor for biomedical diagnostics, histological analysis and tissue characterization in research and clinical applications.

CHAPTER 5
DEMONSTRATION OF OUTCOME BASED EDUCATION (OBE)

The design and simulation of a silicon plasmonic refractive index sensor reflect core OBE principles through applied learning and research [42].

5.1 Introduction

The industry witnessed rapid advancements in photonic sensing technologies, necessitating outcome-based engineering education to equip graduates with practical, research-oriented skills. This chapter demonstrates how the principles of Outcome Based Education (OBE) were applied and achieved through the development of our silicon plasmonic refractive index sensor.

5.2 Course outcomes (COs) and their mapping with program outcomes (POs)

The following table shows the COs addressed in EEE 4800 for Project and Thesis.

Table 5.1 Course outcomes (CO)s addressed

COs	CO Statement	POs	Put Tick
			EEE4800
CO1	Apply knowledge of electrical and electronic engineering to the solution of complex engineering problems.	PO1	
CO2	Identify a contemporary real-life problem related to electrical and electronic engineering by reviewing and analyzing existing research works.	PO2	√

CO3	Determine functional requirements of the problem considering feasibility and efficiency through analysis and synthesis of information.	PO4	√
CO4	Select a suitable solution and determine its method considering professional ethics, codes, and standards.	PO8	√
CO5	Adopt modern engineering resources and tools for the solution of the problem.	PO5	√
CO6	Prepare a management plan and budgetary implications for the solution of the problem.	PO11	√
CO7	Analyze the impact of the proposed solution on health, safety, culture, and society.	PO6	√
CO8	Analyze the impact of the proposed solution on the environment and sustainability.	PO7	√
CO9	Develop a viable solution considering health, safety, cultural, societal and environmental aspects.	PO3	√
CO10	Work effectively as an individual and as a team member for the accomplishment of the solution.	PO9	√
CO11	Prepare various technical reports, design documentation, and deliver effective presentations for demonstration of the solution.	PO10	√
CO12	Recognize the need for continuing education and participation in professional societies and meetings.	PO12	√

5.3 Aspects of program outcomes (POs) addressed

The following table shows the aspects addressed for certain program outcomes (POs) addressed in EEE 4800 for project and thesis.

Table 5.2 Aspects of program outcomes (PO)s addressed

	Statement	Different Aspects	Put Tick (√)
PO3	**Design/development of solutions**: Design solutions for complex electrical and electronic engineering problems and design systems, components or processes that meet specified needs with appropriate consideration for public health and safety, cultural, societal, and environmental considerations.	Public health	
		Safety	
		Cultural	
		Societal	
		Environmental	
PO4	**Investigation:** Conduct investigations of complex electrical and electronic engineering problems using research-based knowledge and research methods including design of experiments, analysis and interpretation of data, and synthesis of information to provide valid conclusions.	Design of experiments	√
		Analysis and interpretation of data	√
		Synthesis of information	√
PO6	**The engineer and society:** Apply reasoning informed by contextual knowledge to assess societal, health, safety, legal and cultural issues and the consequent responsibilities relevant to professional engineering practice and solutions to complex electrical and electronic engineering problems.	Societal	√
		Health	√
		Safety	√
		Legal	
		Cultural	√
PO7	**Environment and sustainability:** Understand and evaluate the sustainability and impact of professional engineering work in the solution of	Societal	√

	complex electrical and electronic engineering problems in societal and environmental contexts.	Environmental	√
PO8	**Ethics:** Apply ethical principles embedded with religious values, professional ethics and responsibilities, and norms of electrical and electronic engineering practice.	Religious values	
		Professional ethics and responsibilities	√
		Norms	√
PO10	**Communication:** Communicate effectively on complex engineering activities with the engineering community and with society at large, such as being able to comprehend and write effective reports and design documentation, make effective presentations, and give and receive clear instructions.	Comprehend and write effective reports	√
		Design documentation	√
		Make effective presentations	√
		Give and receive clear instructions	√
PO11	**Project management and finance:** Demonstrate knowledge and understanding of engineering management principles and economic decision-making and apply these to one's own work, as a member and leader in a team, to manage projects and in multidisciplinary environments.	Engineering management principles	√
		Economic decision-making	√
		Manage projects	√
		Multidisciplinary environments	√

5.4 Knowledge profiles (K3 – K8) addressed

The following table shows the Knowledge Profiles (K3 – K8) addressed in EEE 4800 for Project and Thesis.

Table 5.3 Knowledge profiles (K3 – K8) addressed

K	Knowledge Profile (Attribute)	Put Tick (√)
K3	A systematic, theory-based formulation of engineering fundamentals required in the engineering discipline	√
K4	Engineering specialist knowledge that provides theoretical frameworks and bodies of knowledge for the accepted practice areas in the engineering discipline; much is at the forefront of the discipline	√
K5	Knowledge that supports engineering design in a practice area	√
K6	Knowledge of engineering practice (technology) in the practice areas in the engineering discipline	√
K7	Comprehension of the role of engineering in society and identified issues in engineering practice in the discipline: ethics and the engineer's professional responsibility to public safety; the impacts of engineering activity; economic, social, cultural, environmental and sustainability	√
K8	Engagement with selected knowledge in the research literature of the discipline	√

The following table explains or justifies how the Knowledge Profiles (K3 – K8) have been addressed in EEE 4800 (Project and Thesis).

Table 5.4 Knowledge profiles (K3 – K8) explanation

K	Explanation/Justification
K3	The project applies core concepts like electromagnetic theory and plasmonics to design a biosensor, integrating theoretical knowledge into practical solutions.

K4	By leveraging advanced materials like silicon, ZrN and TiN, the project pushes the boundaries of nanotechnology and biosensing, aligning with cutting-edge engineering practices.
K5	The project focuses on design and optimization of sensor performance metrics such as sensitivity and Q-factor, using tools like COMSOL Multiphysics to translate theory into functional design.
K6	It utilizes modern tools and technologies such as COMSOL and MATLAB for simulation and analysis, ensuring alignment with current engineering practices in nano-fabrication.
K7	The project addresses public health and safety through improved biosensing, using sustainable materials like silicon and adhering to ethical engineering to minimize environmental impact.
K8	The project builds on the latest research in plasmonic biosensing, comparing designs with existing literature to ensure its contributions are aligned with current advancements in the field.

5.5 Use of complex engineering problems

The project addressed several complex engineering problems that reflect the core competencies emphasized in Outcome Based Education (OBE), such as problem analysis, design and modern tool usage.

5.5.1 Nanoscale optical modeling

Applied Maxwell's equations for simulating light behavior at the nanoscale.

5.5.2 Material optimization

Selected and optimized silicon and plasmonic materials for enhanced sensor performance.

5.5.3 Waveguide design

Engineered waveguide structures to support surface plasmon resonance effectively.

5.5.4 Refractive index sensitivity analysis

Evaluated sensor response to minimal changes in surrounding media.

5.5.5 Multiphysics simulation

Integrated optical and material simulations using advanced tools like COMSOL or Lumerical.

5.5.6 Data interpretation

Analyzed complex simulation outputs to assess performance.

5.5.7 Design constraints handling

Managed trade-offs between sensor performance, fabrication feasibility and scalability.

5.6 Socio-cultural, environmental and ethical impact

The project carries meaningful socio-cultural, environmental and ethical implications, contributing positively to health, sustainability and responsible innovation.

5.6.1 Socio-Cultural Impact

The sensor can contribute significantly to public health by enabling early detection of diseases like cancer, dengue and Alzheimer's, especially in low-resource settings. Its potential for integration into compact, affordable diagnostic devices aligns with global health equity goals.

5.6.2 Environmental Impact

The project promotes sustainability by using silicon, a widely available, non-toxic and recyclable material. Additionally, the sensor's miniaturized and low-power design reduces electronic waste and energy consumption compared to traditional diagnostic equipment.

5.6.3 Ethical Impact

Ethically, the project supports responsible innovation in medical diagnostics by prioritizing accessibility, non-invasive detection and accurate results. It also aligns with ethical standards in biomedical research by aiming to improve human well-being without causing harm.

5.7 Attributes of ranges of complex engineering problem solving (P1 – P7) addressed

The following table shows the attributes of ranges of Complex Engineering Problem Solving (P1 – P7) addressed in EEE 4800 for Project and Thesis.

Table 5.5 Attributes of complex engineering problem solving (P1 – P7) addressed

P	**Range of Complex Engineering Problem Solving**	**Put Tick (√)**
Attribute	Complex Engineering Problems have characteristic P1 and some or all of P2 to P7:	
Depth of knowledge required	**P1:** Cannot be resolved without in-depth engineering knowledge at the level of one or more of K3, K4, K5, K6 or K8 which allows a fundamentals-based, first principles analytical approach	√
Range of conflicting requirements	**P2:** Involve wide-ranging or conflicting technical, engineering and other issues	
Depth of analysis required	**P3:** Have no obvious solution and require abstract thinking, originality in analysis to formulate suitable models	√
Familiarity of issues	**P4:** Involve infrequently encountered issues	√
Extent of applicable codes	**P5:** Are outside problems encompassed by standards and codes of practice for professional engineering	√
Extent of stakeholder involvement and conflicting requirements	**P6:** Involve diverse groups of stakeholders with widely varying needs	
Interdependence	**P7:** Are high level problems including many component parts or sub-problems	√

The following table explains how the attributes of ranges of Complex Engineering Problem Solving (P1 – P7) have been addressed in EEE 4800 (Project and Thesis).

Table 5.6 Attributes of complex engineering problem solving (P1 – P7) explanation

P	Explanation/Justification
P1	The project requires deep knowledge in plasmonics, material science and nanotechnology (K3-K8). A first-principles approach is essential for designing the sensor and optimizing its performance through advanced simulation tools like COMSOL Multiphysics.
P2	The project must balance sensor sensitivity, material selection and cost-efficiency, addressing conflicting challenges such as optimizing performance while ensuring scalability.
P3	Designing a novel sensor requires abstract thinking and analysis to model interactions between analytes and plasmonic materials, formulating new approaches for enhancing sensitivity.
P4	The use of alternative materials like ZrN in plasmonics presents uncommon challenges in terms of material properties, requiring innovative solutions.
P5	The project deals with the emerging field of silicon plasmonics, which is not fully covered by existing standards. The development of a novel sensor will push beyond traditional biosensing.
P6	The project serves various sectors, each with distinct accuracy, cost, scalability, necessitating a flexible and inclusive approach.
P7	This complex project involves multiple components, such as material optimization, sensor design and performance analysis, each presenting unique sub-problems that must be addressed to achieve the desired overall outcome.

5.8 Attributes of ranges of complex engineering activities (A1 – A5) addressed

The following table shows the attributes of ranges of Complex Engineering Activities (A1 – A5) addressed in EEE 4800 for Project and Thesis.

Table 5.7 Attributes of complex engineering problem activities (A1 – A7) addressed

A	Range of Complex Engineering Activities	Put Tick (√)
Attribute	Complex activities means (engineering) activities or projects that have some or all of the following characteristics:	
Range of resources	**A1:** Involve the use of diverse resources (and for this purpose resources include people, money, equipment, materials, information and technologies)	√
Level of interaction	**A2:** Require resolution of significant problems arising from interactions between wide-ranging or conflicting technical, engineering or other issues	√
Innovation	**A3:** Involve creative use of engineering principles and research-based knowledge in novel ways	√
Consequences for society and the environment	**A4:** Have significant consequences in a range of contexts, characterized by difficulty of prediction and mitigation	√
Familiarity	**A5:** Can extend beyond previous experiences by applying principles-based approaches	√

The following table explains or justifies how the attributes of ranges of Complex Engineering Activities (A1 – A5) have been addressed in EEE 4800 (Project and Thesis).

Table 5.8 Attributes of complex engineering problem activities (A1 – A7) explanation

A	Explanation/Justification
A1	The project requires multiple resources including advanced technologies (COMSOL, MATLAB), materials (silicon, ZrN) and expertise from various fields like nanotechnology and biosensing.
A2	It addresses conflicting engineering challenges, such as optimizing performance while balancing cost and sustainability, which requires resolving complex technical interactions.

A3	The project applies engineering principles in novel ways, leveraging research-based knowledge to design and optimize a new plasmonic sensor for biological detection.
A4	The sensor's real-world applications in medical, environmental and industrial contexts have wide-ranging impacts, requiring careful consideration of unpredictable variables and mitigation strategies.
A5	This project extends beyond traditional plasmonics, using principles-based approaches to explore new materials and design strategies that push the boundaries of current biosensing technologies.

CHAPTER 6
CONCLUSION

This study has systematically addressed the challenge of developing a high-performance, CMOS-compatible plasmonic sensor by pioneering the use of n-doped silicon as a superior alternative to traditional noble metals. The research journey, detailed in the preceding chapters, has culminated in an optimized sensor design validated through rigorous simulation and a clear assessment of its broader implications.

This concluding chapter synthesizes the key outcomes of this work by first presenting a summary of the principal findings, which chronicles the design evolution and the achieved performance metrics. It then elaborates on the significance and impact of the research, highlighting its contributions to material science, semiconductor integration and biosensing applications. Finally, the chapter outlines a trajectory for future work, identifying the critical steps required to transition this theoretical model into a practical, deployable technology, thereby charting the course for subsequent research and development.

6.1 Summary of the key findings

This research has successfully established the foundation for a high-performance, CMOS-compatible plasmonic RI sensor utilizing n-doped silicon (n-Si) as its core material. The investigative journey began with a preliminary grating-based structure, which confirmed basic plasmonic coupling but exhibited limited sensitivity [2]. This prompted a series of deliberate design modifications, leading to the development of a ladder-like resonator and subsequently a simplified rectangular structure, each iteration offering improved field confinement and richer resonance characteristics [2].

The culmination of this process was Finalised design, a sophisticated geometry comprising a central rectangular resonator, four strategically placed dielectric pillars for enhanced mode control and six embedded n-Si rings within the main cavity. This configuration proved highly effective in supporting multiple, sharp resonance dips by facilitating complex plasmonic hybridization and strong light-matter interaction [2].

The performance of this final design was rigorously enhanced through a systematic parametric optimization process using finite-element method (FEM) simulations. Critical dimensions, including the gap between pillars (d), pillar height (h_1), resonator width (w_1), inner and outer ring radii (r and R) and the coupling distance between the ring and waveguide (w_3), were meticulously swept to identify their optimal values [2], [7]. This data-driven approach ensured a balanced trade-off between high sensitivity and resonance sharpness.

The outcome was a sensor achieving a remarkable maximum sensitivity of 1270 nm/RIU and an FOM of 22.3, a substantial leap from the initial design's performance and competitive with many noble metal-based counterparts [2], [7].

To firmly establish its practical utility, the optimized sensor was evaluated for its capability to detect biologically relevant analytes. The sensor demonstrated exceptional precision in correlating resonance wavelength shifts with specific refractive indices, successfully discriminating between various critical biological components. This was demonstrated for blood constituents such as plasma, hemoglobin and red blood cells [36]; distinct brain tissues including grey matter, white matter and the cerebellum [37]; key intracellular components like DNA, lipids and proteins [39]; and various organ tissues such as liver and muscle [40].

The strong, localized electric and magnetic field distributions at the metal-dielectric interface, as visualized in the simulations, confirmed efficient plasmonic coupling and underpinned this high detection capability [2]. Crucially, the reliance on n-doped silicon not only provides superior chemical stability and reduced optical loss compared to noble metals but also guarantees full compatibility with standard CMOS fabrication processes [2], [8]. This strategic material choice positions the proposed sensor as a highly promising and viable platform for the future development of scalable, cost-effective and integrated lab-on-a-chip systems for real-time, label-free biosensing in point-of-care diagnostics and environmental monitoring [2], [7], [8].

6.2 Significance and impact

The significance of this research extends beyond conventional performance metrics, representing a paradigm shift in plasmonic sensor design with profound implications for integrated photonics and sensing technology. This work establishes a comprehensive theoretical and computational framework that fundamentally redefines the material basis for high-performance plasmonics, demonstrating that n-doped silicon can not only match but surpass noble metals in key aspects of sensor design.

Our systematic investigation provides the first complete methodology for optimizing doped silicon's plasmonic properties through strategic doping and geometric engineering, effectively overcoming the century-old reliance on precious metals and creating new possibilities for sustainable photonic technologies [2], [9]. The research makes groundbreaking contributions to semiconductor-based sensing through its holistic CMOS-compatible approach. By synergistically combining a native semiconductor material with fabrication-friendly geometries, we have resolved the longstanding conflict between high sensitivity and manufacturing scalability that has plagued conventional plasmonic sensors.

The breakthrough enables the seamless integration of high-performance sensing capabilities directly into standard silicon photonics platforms, effectively bridging the gap between laboratory demonstrations and commercial implementation [20], [8]. The implications for the semiconductor industry are substantial, as it opens pathways for monolithically integrated sensing-processing-communication systems on a single chip.

Most importantly, this work demonstrates unprecedented versatility in biological sensing applications. The sensor's capability to accurately detect and distinguish diverse biological entities, from subcellular components to complex tissues, across multiple physiological systems establishes a new benchmark for silicon-based photonic biosensors. This multi-scale detection capability, combined with the sensor's inherent compatibility with microfluidic systems, positions it as a transformative technology for next-generation medical diagnostics, enabling everything from rapid point-of-care testing to sophisticated laboratory analysis [7], [36], [40].

The research thus delivers not just an incremental improvement, but a foundational technology that accelerates the convergence of photonics, semiconductor manufacturing and biomedical engineering toward the realization of truly integrated lab-on-chip systems for personalized medicine and environmental monitoring.

6.3 Future works

This research establishes a foundation for several critical future investigations to advance the proposed sensor from simulation to practical application. The immediate next step involves experimental validation, requiring the fabrication of the sensor using standard silicon photonics processes and its characterization with real-world biological samples [43]. This necessitates functionalizing the sensor surface with specific biorecognition elements [44] and implementing antifouling strategies to ensure reliability in complex media [10].

Beyond fabrication, the sensor's functionality can be significantly enhanced. Future designs should explore active tuning through electrical gating of the n-Si to dynamically control resonance [45] and expand the single-channel design into a multiplexed array for simultaneous multi-analyte detection [3].

Ultimately, achieving point-of-care applicability demands full system-level integration. This entails monolithically integrating on-chip light sources and detectors [20] with microfluidic sample delivery systems to create a compact, portable lab-on-a-chip device [18].

REFERENCES

[1] A. A. Melikyan, et al., "CMOS-compatible hybrid plasmonic waveguide for biosensing applications," *Optics Express*, vol. 23, no. 7, pp. 9110–9120, 2015.

[2] M. O. Paruque, R. Al Mahmud and R. H. Sagor, "Highly sensitive plasmonic refractive index sensor using doped silicon: An alternative to MIM structures," *Plasmonics*, vol. 17, no. 1, pp. 203–211, 2022.

[3] D. P. Gao, et al., "Plasmonic interferometer array biochip as a new label-free biosensor platform for multiparallel detection," *Analytical Chemistry*, vol. 85, no. 20, pp. 9781–9788, 2013.

[4] G. Kumar and P. K. Sarwat, "Interaction of surface plasmon polaritons with nano materials," *Reviews in Plasmonics*, pp. 103–129, 2015.

[5] J. Homola, "Surface plasmon resonance sensors for detection of chemical and biological species," *Chemical Reviews*, vol. 108, no. 2, pp. 462–493, 2008.

[6] H. Chen, et al., "Label-free detection of cancer biomarkers using silicon nanowire biosensors," *ACS Nano*, vol. 6, no. 8, pp. 6546–6551, 2012.

[7] R. Rahad, et al., "Plasmonic refractive index sensing in the early diagnosis of diabetes, anemia, and cancer: An exploration of biological biomarkers," *Results in Physics*, vol. 49, p. 106478, 2023.

[8] R. Rahad, et al., "Fuel classification and adulteration detection using a highly sensitive plasmonic sensor," *Sensing and Bio-Sensing Research*, vol. 40, p. 100560, 2023.

[9] V. K. Naik, V. M. Shalaev and A. Boltasseva, "Alternative plasmonic materials: Beyond gold and silver," *Advanced Materials*, vol. 25, no. 24, pp. 3264–3294, 2013.

[10] E. Mauriz, "Low-fouling substrates for plasmonic sensing of circulating biomarkers in biological fluids," *Biosensors*, vol. 10, p. 60, 2020.

[11] Y. Ren, Y. Zhang and Y. Zhang, "Silicon-coated plasmonic sensor with enhanced sensitivity ", *Optics and Lasers in Engineering*, vol. 145, p. 106650, 2025.

[12] L. Hajisharifzadeh, M. S. M. Ali, and M. M. B. S. Ali, "Design and numerical evaluation of a high sensitivity plasmonic refractive index sensor," *Optics Communications*, vol. 490, p. 127907, 2021.

[13] L. Hajisharifzadeh, M. S. M. Ali and M. M. M. B. S. Ali, "Design of a hybrid plasmonic refractive index sensor," *Optics Communications*, vol. 489, p. 127084, 2021.

[14] L. Hajisharifzadeh, M. S. M. Ali, and M. M. M. B. S. Ali, "A high sensitivity refractive index biosensor based on MIM structure," *Optics Communications*, vol. 490, p. 127907, 2021.

[15] M. O. Paruque, et al., "Materials perspectives of integrated plasmonic biosensors, " *Plasmonics*, 2022.

[16] Y.-W. Huang, et al., "Zirconium nitride for plasmonic cloaking of visible nanowire photodetectors," *Plasmonics*, vol. 15, pp. 1249–1258, 2020.

[17] Y. Yang, et al., "Ultrathin titanium nitride epitaxial structures for tunable infrared plasmonics," *The Journal of Physical Chemistry C*, vol. 127, no. 36, pp. 13642–13650, 2023.

[18] A. D. Rakic, A. B. Djurisic, J. M. Elazar and M. L. Majewski, "Optical properties of metallic films for vertical-cavity optoelectronic devices," *Applied Optics*, vol. 37, no. 22, pp. 5271–5283, 1998.

[19] Z. Zhang, Z. Fang, Y. Wang, W. Chen and L. Sun, "Plasmonic nanostructures for sensitive sensing: From nanometers to nanorays," *Sensors*, vol. 18, no. 1, p. 116, 2018.

[20] A. Shakoor, A. Cheah, B. C. Hao, D. Al-Rawhani, M. Nagy, B. Grant, J. Dale, C. Keegan, N. McNeil and C. D. Cumming, "Plasmonic sensor monolithically integrated with a CMOS photodiode," *ACS Photonics*, vol. 3, pp. 1906–1913, 2016.

[21] W. Jiang, M. Yan, S. Yu, X. Xu, A. Liu, G. Wang, C. Li, M. Xu and G. Gao, "Highly sensitive plasmonic refractive index sensor based on MIM waveguide," *Micromachines*, vol. 15, no. 8, p. 987, 2024.

[22] J. Anker, W. P. Hall, O. Lyandres, N. C. Shah, J. Zhao, and R. P. Van Duyne, "Biosensing with plasmonic nanosensors," *Nature Materials*, vol. 7, no. 6, pp. 442–453, 2008.

[23] Z. Zhang, et al., "Plasmonic refractive index sensor with high figure of merit based on concentric-ring resonator," *Sensors*, vol. 18, no. 1, p. 116, 2018.

[24] A. Boltasseva and H. A. Atwater, "Low-loss plasmonic metamaterials," *Science*, vol. 331, no. 6015, pp. 290–291, 2011.

[25] P. Damborsky, P. Svitel and J. Karthik, "Silicon photonic biosensors using label-free detection," *Sensors*, vol. 18, no. 10, p. 3519, 2018.

[26] K. Rashid, K. S. Tasnif, I. Yaseer, A. A. Hassan, M. F. Sagor and R. H. Sagor, "Cop-shaped refractive index sensors embedded with gold nanorings for temperature sensing of multiple analytes," *Optics Express*, vol. 29, no. 23, pp. 37514–37554, 2021.

[27] A. Miah, M. Omar Faruque and R. H. Sagor, "Plasmonic refractive index sensor based on ring-type pentagonal resonator with high sensitivity," *Plasmonics*, vol. 18, pp. 749–758, 2023.

[28] A. Rakib, A. K. M., et al., "ZnA-based plasmonic sensor: A promising alternative to traditional noble-metal-based sensors for CMOS-compatible and stable optical properties," *Optics Express*, vol. 31, no. 23, pp. 25280–25297, 2023.

[29] T. Hossain, et al., "A plasmonic refractive index sensor based on gold–silicon hybrid structures for highly sensitive detection and alteration of biomolecules," *Journal of Optics*, vol. 52, no. 3, p. 2023, 2023.

[30] M. Rahman, et al., "A tunable plasmonic refractive index sensor with nanoring-strip gratings arrays," *Sensors*, vol. 18, p. 4498, 2018.

[31] X. Chen, *et al.*, "Ultrabroad dynamic range plasmonic refractive index sensor based on silicon structures," *Scientific Reports*, vol. 14, 2024, Art. no. 71874.

[32] Y. Li, *et al.*, "High-sensitivity metal–insulator–metal waveguide-based plasmonic sensors with ring resonators," *Plasmonics*, vol. 18, pp. 1125–1136, 2023.

[33] R. Singh, *et al.*, "Plasmonic biosensing of glucose and dopamine using Si–metal hybrid structures," *arXiv preprint* arXiv:2007.00064, 2020.

[34] S. Farooq, *et al.*, "Optimizing plasmonic nanostructures array for high-performance sensing applications," *Results in Physics*, vol. 25, Art. no. 103886, 2025.

[35] G.-Y. Wang, *et al.*, "A refractive index sensor based on an analogy T-shaped metal–insulator–metal waveguide," *Optik*, vol. 174, pp. 448–454, 2018.

[36] M. Kumar, *et al.*, "Analysis of integrated silicon nitride lab-on-a-chip optofluidic sensor at visible wavelength for absorbance-based biosensing applications," *Microsystem Technologies*, vol. 27, no. 9, pp. 3499–3506, 2021.

[37] R. Bacallao, K. Kiamsh Kai and L. Jeanits, "*Guiding Principles of Specimen Preservation for Confocal Fluorescence Microscopy*," in *Handbook of Biological Confocal Microscopy*. Boston, MA: Springer, 1995, pp. 311–325.

[38] R. Simpson, "Homogenization of mammalian tissue," *Cold Spring Harbor Protocols*, 2010(7), pdb.prot5455.

[39] I. Bigio and S. Bown, "Spectroscopic sensing of cancer and cancer therapy," *Current Status of Translational Research: Cancer Biology & Therapy*, vol. 3, pp. 259–267, 2004.

[40] J.-C. Lai, *et al.*, "Complex refractive index measurement of biological tissues by attenuated total reflection ellipsometry," *Applied Optics*, vol. 49, no. 16, pp. 3323–3328, 2010.

[41] A. Boyde and A. Wood, "Preparation of animal tissues for surface-scanning electron microscopy," *Journal of Microscopy*, vol. 90, pp. 221–249, 1969.

[42] T. Saba, *et al.*, "The potential of heavily doped n-type silicon in plasmonic sensors," *Nanomaterials*, vol. 12, Art. no. 114664, 2024.

[43] W. Bogaerts, *et al.*, “Silicon microring resonators,” *Laser & Photonics Reviews*, vol. 6, no. 1, pp. 47–73, 2012.

[44] M. C. Estevez, *et al.* , “Integrated optical devices for lab-on-a-chip biosensing applications,” *Laser & Photonics Reviews*, vol. 6, pp. 199–216, 2014.

[45] Y. Sopper, *et al.*, “Strongly enhanced molecular fluorescence inside a nanoscale waveguide gap,” *Nano Letters*, vol. 12, no. 2, pp. 1021–1025, 2012.

[46] N. L. Kazanskiy, S. N. Khonina, and M. A. Butt, "Plasmonic sensors based on metal–insulator–metal waveguides for refractive index sensing applications: A brief review," Physica E, vol. 117, p. 113798, 2020.

[47] M. Danaie and A. Shahzadi, "Design of a high-resolution metal–insulator–metal plasmonic refractive index sensor based on a ring-shaped Si resonator," Plasmonics, vol. 14, no. 6, pp. 1453–1465, 2019.

[48] M. F. Hassan, R. H. Sagor, M. R. Amin, M. R. Islam, and M. S. Alam, "Point of care detection of blood electrolytes and glucose utilizing nano-dot enhanced plasmonic biosensor," IEEE Sensors Journal, vol. 21, no. 16, pp. 17749–17757, 2021.

[49] M. Yan and M. Qiu, "Analysis of surface plasmon polariton using anisotropic finite elements," IEEE Photonics Technology Letters, vol. 19, no. 22, pp. 1804–1806, 2007.

[50] X.-P. Jin, X.-G. Huang, J. Tao, X.-S. Lin, and Q. Zhang, "A novel nanometric plasmonic refractive index sensor," IEEE Transactions on Nanotechnology, vol. 9, no. 2, pp. 134–137, 2010.

[51] S. A. Maier, Plasmonics: Fundamentals and Applications. Springer, 2007.

[52] Q. Zhang, X.-G. Huang, X.-S. Lin, J. Tao, and X.-P. Jin, "A subwavelength coupler-type MIM optical filter," Optics Express, vol. 17, no. 9, pp. 7549–7554, 2009.

[53] M. A. Butt, S. N. Khonina, and N. L. Kazanskiy, "A multichannel metallic dual nano-wall square split-ring resonator: design analysis and applications," Laser Physics Letters, vol. 16, no. 12, p. 126201, 2019.